A Theoretical and Observational Comparison of Cirrus Cloud Radiative Properties

By
Paul W. Stackhouse Jr. and Graeme L. Stephens

Department of Atmospheric Science
Colorado State University
Fort Collins, Colorado

Research supported by NSF grants ATM-8812353 and ATM-8519160; DOD grants AFOSR-88-0143 and ONR N00014-87K-0228/P00001.
PI: G. Stephens

Colorado State University

Department of Atmospheric Science

Paper No. 452

A THEORETICAL AND OBSERVATIONAL COMPARISON OF CIRRUS CLOUD RADIATIVE PROPERTIES

by

Paul W. Stackhouse, Jr. and Graeme L. Stephens

Research supported by NSF Grants ATM-8812353 and ATM-8519160;
DOD Grants AFOSR-88-0143 and ONR N00014-87K-0228/P00001

Principal Investigator: Graeme L. Stephens

Department of Atmospheric Science
Colorado State University
Ft. Collins, CO 80523

August 1989

Atmospheric Science Paper No. 452

ABSTRACT

An understanding of the interaction of radiation in cirrus clouds is crucial to determining the ways in which these clouds interact with climate forcings. A two stream radiative transfer model is developed and used to examine the properties of hypothetical cirrus clouds and compare simulations with the observations made on Oct 28, 1986 during the cirrus FIRE IFO.

The two stream model was chosen and formulated in a way which allowed for the consistent treatment of physical processes such as absorption and scattering by both molecules and particles which occur during the interaction of cloud and radiation. This was accomplished by solving the radiative transfer equation assuming a plane-parallel, horizontal homogeneous and azimuthally symmetric atmosphere in terms of reflectance and transmittance coefficients and source terms dependent upon the optical depth, single scatter albedo and asymmetry factor of the optical media. The above three parameters represent the optical properties of molecules and particles for absorption and scattering processes and are weighted according to Slingo and Schrecker (1982). The particulate optical properties are determined using Mie solutions assuming equivalent diameter spheres from the particles measured during the IFO. Gaseous absorption is calculated using the k-distribution method for H_2O, CO_2, O_3 and O_2 where applicable in the solar and infrared wavelengths. Parameterizations of Rayleigh scatter and e-type absorption were also included.

The recognition and resolution of the instability discovered in the infrared is a new contribution to two stream radiation modeling. Agreement of clear-sky heating rates between published line-by-line results and simulated cases is within 0.3 °K/day at cirrus cloud altitude. Fluxes from solar two stream cloudy-sky simulations show discrepancies in most cases less than 5 % of those from a more complicated established model.

The sensitivity of cirrus cloud radiative properties to altitude and size distribution changes are examined. The net radiative effect of cirrus in the infrared is largely determined by the surface-cloud base temperature difference (and thus altitude) and increases (decreases) of this temperature difference causes net heating (cooling) to occur. Cloud top solar heating increases (decreases) with increasing (decreasing) altitude in proportion to

the amount of atmosphere above the cloud layer. Since the concentrations of particles less than 100 μm in diameter are uncertain, particles of this size are added to measured size distributions. The addition of these particles greatly enhances the absorption and albedo of cirrus clouds. Simulations of cirrus clouds with realistic IWC profiles are also performed and it is shown that the radiative heating relative to clear-sky in both the longwave and the shortwave is maximized in the thickest layer of the cloud.

Lastly, simulations using observed microphysical and environmental conditions are performed and compared to measured cirrus cloud radiative properties. Although cloud inhomogeneities are shown to be quite large, comparisons of simulations to observations reveal two sources of discrepancies: the underestimation of the concentrations of small particles and the overestimation of the asymmetry parameter produced by the equivalent sphere approximation. Improved measurements of small particles and irregular ice crystal scattering theories can greatly improve the agreement of theory and observations and may lead to an improved understanding of the interaction between climate and cirrus clouds.

ACKNOWLEDGEMENTS

We wish to acknowledge various people who have contributed in different ways to this research. Among those are Dr. Stephen Cox and Dr. Roger Culver for their participation and evaluation of this paper.

We also acknowledge Dr. Andrew Heymsfield for providing reduced microphysical data and Ming-Dah Chou of Goddard Laboratory for Atmospheric Sciences, GSFC for providing the k-distribution data used in this study. We especially appreciate the time and effort spent by Paul Hein and William Smith, Jr. providing the methods and software required to reduce the radiative data from the FIRE IFO. We would like to especially thank the following individuals, Dr. Si-Chee Tsay, Thomas Greenwald, David Duda, Takmeng Wong and Frank Evans for their constructive collaboration and editorial support. We also gratefully acknowledge the efforts of Sue Lini, who helped in preparing this paper.

This research was supported by the Atmospheric Sciences Section of the National Science Foundation under Contracts ATM-8812353 and ATM-8519160; the Department of Defense, United States Air Force Office of Scientific Research under Grant AFOSR-88-0143; and the Department of Defense Office of Naval Research Grant N00014-87-K-0228/P00001. The Mie solution computations were performed using the super computer facilities at Colorado State University Computer Center.

CONTENTS

LIST OF FIGURES

LIST OF TABLES

Chapter 1

INTRODUCTION

1.1 The Importance of Cloud Radiative Interactions to Climate

Ramanathan (1987), suggests that the interaction between clouds and climate plays an intimate role in the feedback mechanisms which occur in response to perturbations of the present climate. These perturbations may be caused by changes in solar input, the planetary albedo or emitted radiation all of which comprise the energy balance of the climate system. Processes which change the earth's albedo (ie. glaciation, deforestation) or affect the emission of radiation by the atmosphere (ie., increasing greenhouse gases) also affect the radiation budget of the earth. The atmospheric general circulation is a direct result of the differential net heating of the earth (see Fig. 1.1). Ramanathan (1988) explores the sensitivity of the driving mechanism of the general circulation by noting that in the tropics 80% of the absorbed solar radiation is balanced by infrared emission (refer to Fig. 1.1). Thus the remaining 20% of the absorbed solar radiation in the tropics accounts for the excess radiative energy in this region which ultimately drives the general circulation. Therefore, a sustained anomaly of 10% in either the solar absorption or infrared emission of the atmosphere may have a substantial impact on the atmosphere's general circulation and thus on the climate of the earth. The role of clouds in this process determines the overall sensitivity of the earth's climate to perturbations of the earth's radiation budget. Thus an understanding of the way radiation interacts with clouds is vital for understanding the sensitivity of the earth's climate to both natural and anthropogenic changes in the atmosphere.

1.2 Observations and Models

In order to understand the cloud-climate interaction problem more completely, the quality and quantity of observations must be improved. An increased ability to model climate sensitivity accurately is also required. The former is the principle objective of the International Satellite Cloud Climatology Project (ISCCP) and the later is being studied improving, the realism in the way cloud feedback mechanisms are represented in climate models (Stephens et al.,1989). Both efforts face problems in dealing with cirrus which are not negligible. For example, accurate detection of the horizontal and vertical distributions for high thin cirrus clouds using passive satellite remote sensing techniques is quite difficult due to the extreme variability of the optical parameters of such clouds (Liou, 1986). Infrared brightness temperatures observed from above thin cirrus clouds are usually considerably warmer than the temperature of the cloud itself while the dominant forward scattering properties of these clouds sometimes make detection in the visible difficult. For these reasons, it is difficult to make observations of cirrus clouds using present day satellite observations; this represents a major hurdle for ISSCP.

General circulation models (GCM) possess a cold bias compared to observations in the tropics (see Fig 1.2a,b), in the upper polar troposphere and in the lower polar stratosphere. It has been suggested that both of these problems are traceable to inaccuracies in the parameterization of cirrus clouds in the tropics (Ramaswamy and Ramanathan, 1989) and polar stratospheric clouds in the polar regions (Blanchet, 1985). Thus the uncertainty of the feedbacks between cloudiness, radiation and dynamics on the current climate state are crucial to improve our understanding of cloud-climate interactions. Furthermore, it is imperative to study feedbacks of clouds with radiation and dynamics to improve the parameterizations of cloud scale processes and reduce the uncertainties associated with general circulation modeling and climate change.

1.3 Cirrus Clouds and FIRE

The effect of cirrus clouds on the environment and surface temperature is is shown to depend upon the optical thickness and altitude of the clouds as demonstrated by Manabe

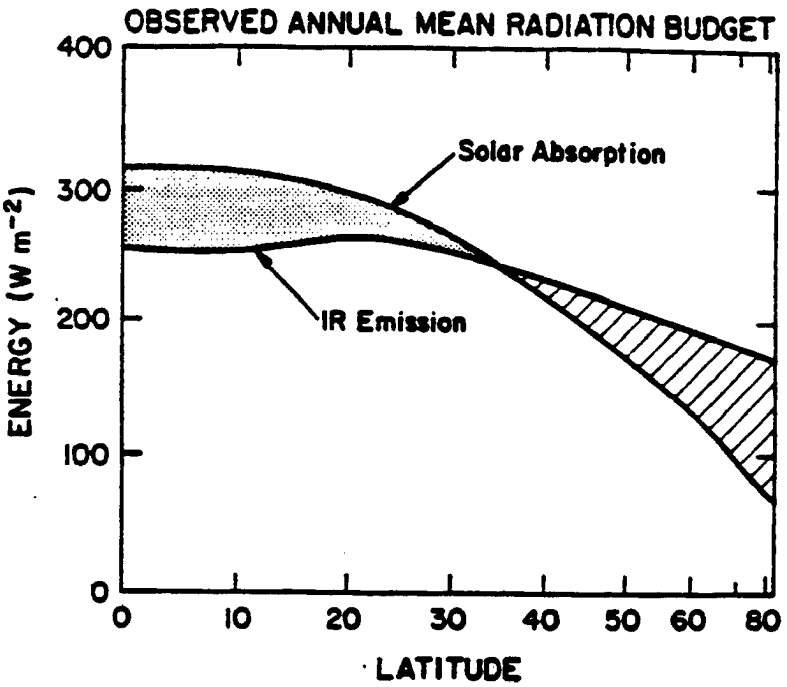

Figure 1.1: Annual zonal mean estimates of absorbed solar radiation and outgoing long-wave flux obtained by satellites. Shaded region denote net heating and dashed regions denote net cooling. (Ramanathan, 1987)

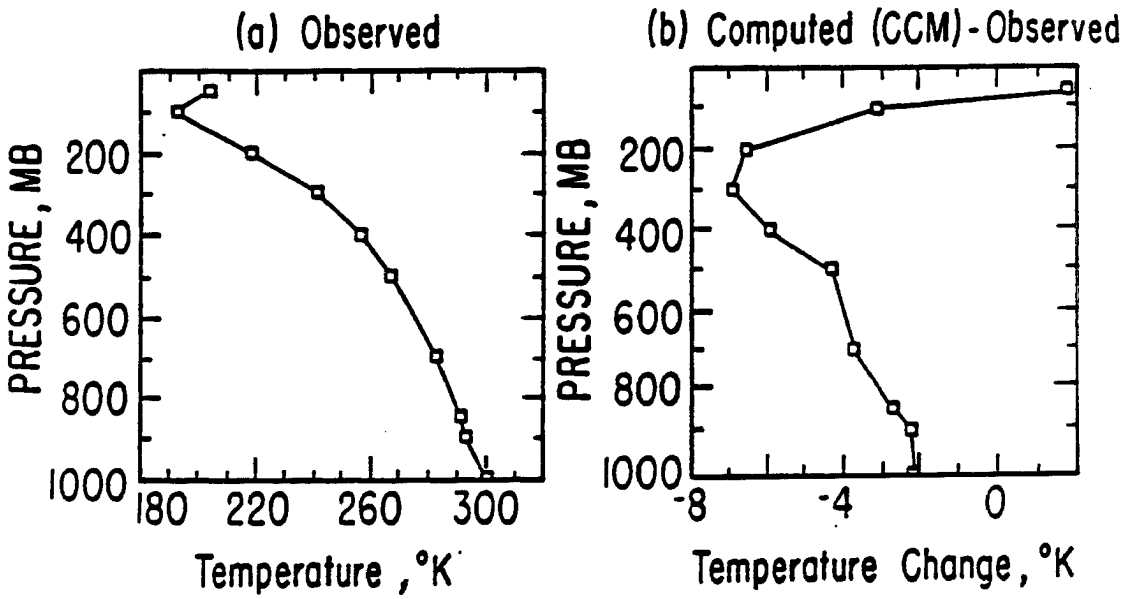

Figure 1.2: Vertical distributions of (a) observed zonal mean temperature and (b) differences between the GCM computed zonal mean temperature and observed zonal mean temperatures at the equator for January. (Ramaswamy and Ramanathan, 1989)

and Strickler (1964), Cox (1973) and by Stephens and Webster (1981) among others. These studies show that high thin cold cirrus clouds located above a warm surface (ie. tropical cirrus clouds) exhibit infrared warming throughout the depth of the cloud and impose a climate warming effect on simulated surface temperatures relative to clear sky temperatures. These results suggest that cirrus are capable of providing a strong positive feedback to greenhouse gas warming as predicted by the modeling studies of Roeckner, *et al.* (1987). Couple these examples with the facts that cirrus clouds are a pervasive feature of the atmosphere, regularly covering approximately 20% of the globe at one time (Liou, 1986) and that thin 'subvisible' cirrus may cover a much larger percentage of the globe (e.g., Prabhakara *et al.* 1988), the importance of studying the properties of cirrus clouds is evident. A more complete understanding of the microphysical parameters of cirrus and the interaction of radiation by these particles will lead to improved parameterizations of these processes in GCM's

For this reason the First ISCCP Regional Experiment (FIRE) was proposed to examine the microphysical and radiative properties of cirrus clouds with the goal of improving parameterizations of cirrus clouds in GCM's. Very few observational studies of cirrus clouds exist in which microphysical measurements such as particle size distributions and ice water content were simultaneously obtained with radiation measurements (e.g., Griffith *et al.*, 1980; Paltridge and Platt, 1980 and Foote, 1988). Most radiative studies are theoretically based largely because of the inaccessibility of cirrus clouds to *in situ* measurements. Ackerman *et al.* (1988) in a theoretical study, for example, infer microphysical properties of cirrus clouds from remote stratospheric aircraft measurements and satellite observations and apply these in a radiative transfer model to calculate heating rates at infrared and solar wavelengths. No comparison could be made between the theoretical radiative calculations and the observations. Therefore, no opportunity is given to relate observed microphysical parameters to the observed radiative characteristics with cirrus clouds and to validate theory. The FIRE cirrus experiment was designed to provide such an opportunity.

FIRE Cirrus Part 1 was held in Wisconsin in late October and early November in 1986. The project was designed to investigate the microphysical and radiative characteristics of middle latitude frontal and jet stream cirrus. The Intensive Field Observation (IFO) involved collection of data from ground based, aircraft (both tropospheric and stratospheric) and satellite observations.

1.4 Scientific Objectives

The overall goal of this work is to understand more completely the elementary properties of cirrus clouds which influence their radiative characteristics. A related goal of this work is to provide a physical basis for future parameterizations which can be used in GCM's as an effort to improve our understanding of cloud-climate feedbacks. To this end, the following specific tasks are identified.

1. Develop a radiative transfer model for the solar (0.3 μm - 3.8 μm) and infrared (3.8 μm - 50 μm) wavelengths with the aim of investigating the radiative properties of cirrus clouds using a consistent theoretical description of the transfer processes of importance. Unlike most previous theoretical studies, the effects of molecular and particle scattering and absorption are treated in a consistent manner throughout these two spectral regions.

2. Use the observed microphysical and environmental data from actual FIRE cirrus cases in the radiative transfer models to simulate the observed cloud cases and explore the phenomenological relationships between microphysical quantities and radiation.

3. Compare the simulated and observed radiative characteristics for these cirrus cases with the purpose of isolating discrepancies by referring to the phenomenological relationships explored above.

1.5 Plan Of This Research

Chapter 2 describes the derivation of the monochromatic two stream radiative transfer model which is a major focus of this work. Chapter 3 describes the gaseous absorption

band model used in this study and presents clear sky results. This chapter provides new information about some of the numerical instabilities encountered in the extreme clear sky cases and presents reformulations of the two stream model which provide more stable solutions. Chapter 4 describes the inclusion of particle absorption and scattering to the band model, presents original results of a comparison case to an established radiative transfer model and presents a theoretical study of cirrus clouds imbedded in different atmospheres. This chapter contains the bulk of the theoretical results and provides many new original contributions to the problem of cirrus cloud radiation interactions. Chapter 5 compares simulated radiative characteristics to those observed in the FIRE for a selected case. Chapter 6 summarizes the results of this research, presents conclusions and recommendations for future research.

Chapter 2

THE TWO STREAM RADIATIVE TRANSFER MODEL

2.1 Justification of Two Stream Radiative Transfer Model

As previously stated the purpose of this research effort is to compare theoretical and observed radiative characteristics of cirrus clouds and the development of an appropriate theoretical radiative transfer model becomes the cornerstone of this research effort. The model employed must be complex enough to simulate the physics involved in atmospheric radiative transfer (i.e. , cloud particle extinction, Rayleigh scatter, gaseous absorption, and multiple scatter) in a consistent formulation. The theoretical radiative transfer model must also be versatile enough to model the changing conditions of the cirrus environment such as pressure, temperature, humidity etc. , and variations in the microphysical parameters; yet be simple enough to allow a clear interpretation of the results. In addition, the spectral region of interest, determined by the solar and terrestrial wavelengths which are most important to the atmosphere, is 0.28 μm to 500 μm. The spectral region will be divided into two smaller regions: the short wavelengths (or solar wavelengths) .28 μm - 3.8 μm and the long wavelengths (or infrared wavelengths) 3.8 μm - 500 μm. Thus the radiative transfer model must simulate the physics for both the shortwave and longwave separately.

There are many possible radiative transfer model formulations which would adequately satisfy the above criteria within the confines of the assumptions that are stated above. The n-stream type of model with adding and doubling probably simulates most accurately the measured radiative fields. However, lack of measurements concerning the directionality of the radiative fields, especially for downwelling radiation and the overall complexity of this type of model make such a model impractical given the objectives of this project. A broadband emissivity type model may be used to model the longwave

region, but there is a distinct advantage in modeling the spectral regions equivalent to the spectral range of satellite observations. Also the scattering of radiation in the longwave, which may not be significant for clouds of water droplets, should be considered for clouds of ice crystals (e.g., Stephens,1980). The reflection of upwelling flux from the surface by the cloud is shown to be significant when the temperature difference between the ground and the base of the cloud is maximized. This characteristic of ice clouds could not be adequately modeled with a broadband emissivity model. Thus, a logical alternative is the two stream radiative transfer model, which would allow the physics of the atmosphere to be modeled while maintaining versatility and simplicity for interpretation.

2.2 Formulation of the Two Stream Radiative Transfer Model

The theoretical radiative transfer equation is solved assuming a plane parallel, horizontally homogeneous atmosphere with azimuthal symmetry for monochromatic radiation. The purpose of this study is to establish whether or not these assumptions are reasonable. These assumptions, although coarse provide an adequate starting point to investigate the radiative properties of cirrus clouds.

The monochromatic plane parallel, horizontally homogeneous and azimuthally symmetric radiative transfer equation can be represented by:

$$\mu \frac{dI(\tau,\mu)}{d\tau} = -I(\tau,\mu) + \frac{\omega_0}{2}\int_{-1}^{1} P(\mu,\mu')I(\tau,\mu')d\mu' + S_{sw,lw}(\tau). \tag{2.1}$$

$I(\tau,\mu)$ represents the diffuse intensity as a function of optical depth (τ) and cosine of the zenith angle (μ), ω_0 is the single scatter albedo which is defined as the ratio of scattering extinction to total extinction ($\omega_0 \equiv \frac{k_{sca}}{k_{ext}} \equiv \frac{k_{sca}}{k_{sca}+k_{abs}}$), $S_{sw,lw}(\tau)$ is the diffuse intensity source term and $P(\mu,\mu')$ is the azimuthally averaged angular distribution function (or phase function). The azimuthally independent distribution function is normalized accordingly:

$$\frac{1}{2}\int_{-1}^{1} P(\mu,\mu')\, d\mu' = 1. \tag{2.2}$$

In this representation τ and z increase in the downward direction. Under this convention, it follows that $\mu > 0$ in the downward hemisphere and $\mu < 0$ in the upward hemisphere.

Following Preisendorfer (1976, Chapter 8), integration of (2.1) over the upward and downward hemispheres is respectively performed by the integral operators

$$\int_{-1,0}^{0,1} \ldots d\mu, \tag{2.3}$$

which transform the radiative transfer equation into upward and downward fluxes. Noting that,

$$\mp \int_{-1,0}^{0,1} \mu I(\tau, \mu) d\mu = \mp F^{\pm}(\tau) \tag{2.4}$$

defines the fluxes $F^{\pm}$ (units Wm^{-2}) and that,

$$\int_{-1,0}^{0,1} I(\tau, \mu) d\mu = U^{\pm}(\tau) \tag{2.5}$$

where $U^{\pm}$ are upward and downward directed scalar irradiances (units Wm^{-2}), then the resulting equations can be arranged as follows:

$$\mp \frac{dF^{\pm}(\tau)}{d\tau} = (f^{\pm} - D^{\pm})F^{\pm}(\tau) + b^{\mp}F^{\mp} + Us^{\pm}_{sw,lw} \tag{2.6}$$

where $D^{\pm}$ is the layer diffusivity and may be thought of as the increase in the optical path of a photon due to scattering and absorption-emission processes as it passes through a horizontal layer of the atmosphere. The diffusivity is defined as:

$$D^{\pm} = \frac{U^{\pm}(\tau)}{F^{\pm}(\tau)}. \tag{2.7}$$

It follows from this definition that the product of the diffusivity factor and flux have units of scalar irradiance. For generality, the assumption that the diffusivity is equivalent in both directions is not made. Generally, it is assumed that,

$$D = \begin{cases} \text{clear sky } 1.66 \\ \text{cloudy sky } 2.0 \end{cases} \text{diffuse radiation} \qquad \begin{matrix} 1/\mu_0 \end{matrix} \text{collimated radiation} \tag{2.8}$$

where μ_0 is the cosine of the solar zenith angle.

Referring again to (2.6), $b^{\pm}$ and $f^{\pm}$ represent the backward and forward scattered fraction of diffuse radiation respectively from the layer. The backward and forward scattered fractions follow from the integration of the multiple scattering term in (2.1) and are defined relative to the flux which is redistributed. Thus, these coefficients appear as

diffusivities and when multiplied by flux produce units of scalar irradiance. The backward and forward scattering fractions are represented as follows:

$$b^{\pm} = \frac{\omega_0}{2F^{\pm}(\tau)} \int_{0,-1}^{1,0} \int_{-1,0}^{0,1} P(\mu,\mu')I(\tau,\mu')d\mu'd\mu \tag{2.9}$$

$$f^{\pm} = \frac{\omega_0}{2F^{\pm}(\tau)} \int_{-1,0}^{0,1} \int_{-1,0}^{0,1} P(\mu,\mu')I(\tau,\mu')d\mu'd\mu \tag{2.10}$$

and are normalized such that:

$$f^{\pm} + b^{\pm} = D^{\pm}\omega_0. \tag{2.11}$$

Lastly, the term $Us^{\pm}_{sw,lw}$ in (2.6) represents the source term after integration over the upward and downward hemispheres and has units of scalar irradiance in agreement with the units of the rest of the terms in (2.6). Equation (2.6) is reformulated by multiplying the identity,

$$k_{ext} \equiv k_{abs} + k_{sca} \tag{2.12}$$

by $D^{\pm}/k_{ext}$ which gives

$$D^{\pm} = \frac{k_{abs}}{k_{ext}} D^{\pm} + f^{\pm} + b^{\pm} \tag{2.13}$$

when noting the normalization (2.11) above and the definition of ω_0. Substitution into (2.6) gives:

$$\mp \frac{dF^{\pm}(\tau)}{d\tau} = -(a^{\pm} + b^{\pm})F^{\pm}(\tau) + b^{\mp}F^{\mp}(\tau) + Us^{\pm}_{sw,lw} \tag{2.14}$$

where $a^{\pm} = (1-\omega_0)D^{\pm}$ and represents the fraction of the total extinction due to particle absorption multiplied by the diffusivity where $1-\omega_0 = \frac{k_{sca}}{k_{ext}}$.

Because of the lack of information concerning the radiance field, (2.9 and 2.10) cannot be solved exactly thereby necessitating the development of various approximations. Different approximations of the diffuse backscatter coefficient are often used in two stream solutions as reported in various studies (see for example, King and Harshavardhan, 1986, Table 2 where b is denoted as γ_2 for a review). Any one of these approximate relationships can be substituted for the above expression in (2.9) provided that the appropriate diffusivity $D^{\pm}$, implied by these approximations, is used. All of these approximations limit the generality of the model in that hemispheric isotropy is assumed, that is $D^{+} = D^{-}$ = constant, and that $b^{+} = b^{-}$. This is also the case assumed here. The diffuse backscatter coefficient

which has been chosen as a first approach is $b = \omega_0(1 - g)$ which corresponds to the mean hemispheric approximation proposed by Sagan and Pollack (1967) where g is the asymmetry factor and is a measure of the forward and backward scatter such that:

$$\begin{array}{rl} -1 \leq g < 0 & \text{backward scatter} \\ 0 < g \leq 1 & \text{forward scatter} \\ g = 0 & \text{isotropic scatter.} \end{array}$$

This approximation of the backward scattered fraction assumes an isotropic up and down intensity and a layer diffusivity of 2 in both hemispheres. This diffuse backscatter coefficient is normalized to $2\omega_0$ which is seen by considering the pure backward scattering particle when $b = 2\omega_0$, as required. Thus b defined in this way, provides for a simple method of determining the diffuse backscatter coefficient in terms of the parameters ω_0 and g which can be determined from Mie scattering theory. Figure (2.1) shows a comparison between this diffuse backward scattering approximation and a diffuse backward scattering coefficient calculated from the Henyey-Greenstein function (see Wiscombe and Grams, 1976).

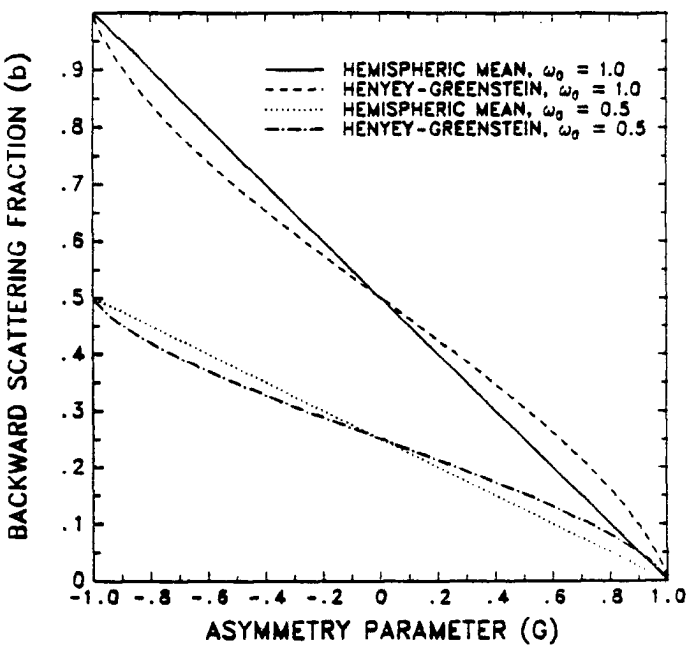

Figure 2.1: Comparison of the Henyey-Greenstein and hemispheric mean backward scattering fractions as a function of asymmetry parameter for $\omega_0 = 1.0$ and $\omega_0 = 0.5$

The equations of (2.14) are reorganized in the form of second order differential equations in F^+ and F^- and are subsequently solved with appropriate boundary conditions.

The presence of source terms necessitates the derivation of particular solutions which are discussed in more detail later but for the moment these sources are treated in a general way. After some algebraic manipulation and recombination of constants the solutions to (2.14) are:

$$F^{\pm}(\tau) = m_{+}\eta_{+}^{\pm}exp(k_{+}\tau) + m_{-}\eta_{-}^{\pm}exp(k_{-}\tau) + Fs_{sw,lw}^{\pm}(\tau). \tag{2.15}$$

where $Fs_{sw,lw}^{\pm}(\tau)$ is the particular solution of the differential equation for the source term and has the units of flux. The constants $\eta_{\pm}^{\pm}$ are defined as follows:

$$\begin{aligned} \eta_{+}^{\pm} &= 1 \pm \tfrac{a^{\mp}}{k_{+}} \\ \eta_{-}^{\pm} &= 1 \pm \tfrac{a^{\mp}}{k_{-}} \end{aligned} \tag{2.16}$$

where

$$k_{\pm} = \frac{1}{2}\{(t^{-} - t^{+}) \pm [(t^{+} + t^{-})^2 - 4b^{+}b^{-}]^{\frac{1}{2}}\} \tag{2.17}$$

and

$$t^{\pm} = -(a^{\pm} + b^{\pm}). \tag{2.18}$$

Noting that $D^{+} = D^{-} = D$ and $b^{+} = b^{-}$, as mentioned above 2.17 and 2.18 become $k_{\pm} = \pm[t^2 - b^2]^{\frac{1}{2}}$ and $t = -(a+b)$ respectively and therefore $\eta_{+}^{+} = \eta_{-}^{-}$ and $\eta_{+}^{-} = \eta_{-}^{+}$.

The constants $m_{\pm}$ from (2.15) can be found by applying boundary conditions at the top and bottom of a layer. Assuming that the optical depth is zero at the top of a layer and τ_1 at the bottom solve for the set of constants using the boundary conditions $F^{+}(\tau_1)$ and $F^{-}(0)$. Substituting these relations into (2.15) give the total solution for the problem. Rearranging the solutions to separate the boundary conditions and sources we are able to express the solution in the following matrix notation

$$\begin{bmatrix} F^{+}(\tau) \\ F^{-}(\tau) \end{bmatrix} = \mathcal{M} \begin{bmatrix} F^{+}(\tau_1) \\ F^{-}(0) \end{bmatrix} + \begin{bmatrix} \mathcal{S}_{sw,lw}^{+}(\tau) \\ \mathcal{S}_{sw,lw}^{-}(\tau) \end{bmatrix} \tag{2.19}$$

where the total source contribution is given by,

$$\begin{bmatrix} \mathcal{S}_{sw,lw}^{+}(\tau) \\ \mathcal{S}_{sw,lw}^{-}(\tau) \end{bmatrix} = \begin{bmatrix} Fs^{+}(\tau) \\ Fs^{-}(\tau) \end{bmatrix} - \mathcal{M} \begin{bmatrix} Fs^{+}(\tau_1) \\ Fs^{-}(0) \end{bmatrix} \tag{2.20}$$

where,

$$\mathcal{M} = \begin{bmatrix} \mathcal{T}(\tau_1, \tau, 0) & \mathcal{R}(0, \tau, \tau_1) \\ \mathcal{R}(\tau_1, \tau, 0) & \mathcal{T}(0, \tau, \tau_1,) \end{bmatrix} \tag{2.21}$$

and where $\mathcal{T}$ and $\mathcal{R}$ correspond to transmittance and reflectance functions. The notation is illustrated in Figure 1.2. The meaning of these two functions follows by considering the homogeneous solution of the differential equation and by noting that the exitant fluxes from the top and bottom of the layer can be expressed in terms of the incoming fluxes.

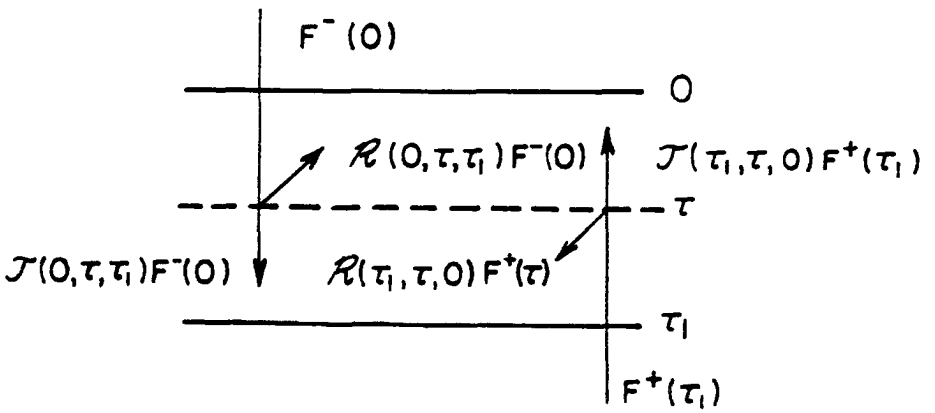

Figure 2.2: A conceptual explanation of the transmittance and reflectance functions for a layer of optical depth τ_1.

The transmittance and reflectance functions, are formed as ratios of the exitant to incident fluxes and depend on the direction in which the radiation is propagating. Thus, the upward and downward transmittance and reflectance functions for an entire layer are not necessarily equivalent (ie. $\mathcal{T}(0,\tau_1,\tau_1) \neq \mathcal{T}(\tau_1,0,0)$ and $\mathcal{R}(0,0,\tau_1,) \neq \mathcal{R}(\tau_1,\tau_1,0)$) as is commonly assumed. The equivalence of these functions in both directions for an entire layer is determined by whether or not the diffusivities are assumed to be equivalent (ie. whether $D^+ = D^-$). The transmittances and reflectances take the following forms:

$$\begin{aligned}
\mathcal{T}(0,\tau,\tau_1) &= \tfrac{1}{\Delta(\tau_1)}[\eta_+^+\eta_-^- \exp(k_+\tau_1 + k_-\tau) - \eta_+^-\eta_-^+ \exp(k_+\tau + k_-\tau_1)] \\
\mathcal{R}(0,\tau,\tau_1) &= \tfrac{\eta_+^+\eta_-^+}{\Delta(\tau_1)}[\exp(k_+\tau_1 + k_-\tau) - \exp(k_+\tau + k_-\tau_1)] \\
\mathcal{T}(\tau_1,\tau,0) &= \tfrac{1}{\Delta(\tau_1)}[\eta_+^+\eta_-^- \exp(k_+\tau) - \eta_+^-\eta_-^+ \exp(k_-\tau)] \\
\mathcal{R}(\tau_1,\tau,0) &= \tfrac{\eta_-^-\eta_-^+}{\Delta(\tau_1)}[\exp(k_+\tau) - \exp(k_-\tau)]
\end{aligned} \tag{2.22}$$

where

$$\Delta(\tau_1) = \eta_+^+\eta_-^- \exp(k_+\tau_1) - \eta_+^-\eta_-^+ \exp(k_-\tau_1). \tag{2.23}$$

Thus the solution (2.19) gives the monochromatic diffuse fluxes at any level inside a homogeneous layer given the parameters τ, ω_0, g and the sources of radiative flux within the layer. For solar wavelengths, a direct component of radiation weighted by the cosine of the solar zenith angle of the form

$$F(\tau) = \mu_0 F_0 \exp\left(-\frac{\tau}{\mu_0}\right)$$

must be added to the diffuse flux given by (2.19) to obtain the total downward flux. Derivation of the monochromatic source terms is now provided.

2.3 The Development of the Source Terms

The processes which produce diffuse radiation in the solar and infrared wavelengths dictate the form in which the source terms are represented within the model. The sources of radiation in the long and short wavelength regions respectively result from the thermal emission within the layer and the single scattering of the direct collimated beam of radiation from the sun.

2.3.1 The Longwave Source Terms

The azimuthally integrated source at any level τ inside a layer of thickness τ_1 due to emission is given by:

$$S_{lw}^{\pm} = 2\pi(1-\omega_0)\mathcal{B}_\nu(\tau) \tag{2.24}$$

where $\mathcal{B}_\nu(\tau)$ is dependent on the Planck emission function. A simple linear relation between the Planck emission function and optical thickness is employed. Thus the emission within the layer can be specified in terms of the emission at the top and bottom of the layer. For this case,

$$\mathcal{B}_\nu(\tau) = B_\nu(T_0) + B_\nu^1(T_0, T_1)\tau \tag{2.25}$$

and,

$$B_\nu^1(T_0, T_1) = \frac{B_\nu(T_1) - B_\nu(T_0)}{\tau_1}. \tag{2.26}$$

$B_\nu(T_0)$ and $B_\nu(T_1)$ represent the Planck function at a particular wavenumber for temperatures at the top (T_0) and bottom (T_1) of the layer respectively. Applying (2.3) on $S^{\pm}_{lw}$ changes the units to scalar irradiance leaving the expression unchanged and therefore:

$$Us^{\pm}_{lw}(\tau) = 2\pi(1-\omega_0)\mathcal{B}_\nu(\tau) \tag{2.27}$$

The particular solution of the differential equation (2.14) becomes:

$$Fs^{\pm}_{lw}(\tau) = \frac{2\pi(1-\omega_0)}{v}\left\{x^{\mp}B_\nu(T_0) + B^1_\nu(T_0,T_1)\left[x^{\mp}\left(\tau - \frac{u}{v}\right) \mp 1\right]\right\} \tag{2.28}$$

where,

$$\begin{aligned} u &= t^+ - t^- \\ v &= b^+b^- - t^+t^- \\ x^{\pm} &= t^{\pm} - b^{\pm}. \end{aligned} \tag{2.29}$$

Thus (2.28) represents the contribution to the flux by emission within a layer. The total longwave source contribution within the layer is computed using (2.20).

2.3.2 The Shortwave Source Terms

The shortwave source term is not as straightforward to derive as the longwave, for it involves a contribution to the diffuse radiation by the scattering of radiation out of the direction of the direct collimated beam. This shortwave source term is represented in the following standard form:

$$S^{\pm}_{sw}(\tau) = \frac{\omega_0 F_0}{2} P(\mu,\mu_0)\exp\left(-\frac{\tau}{\mu_0}\right) \tag{2.30}$$

where μ_0 is the cosine of the solar zenith angle, which is positive in the present representation, and F_0 is the solar irradiance in the downward direction at the top of atmosphere. As with the longwave, applying the operators (2.2) on $S^{\pm}_{lw}$ yields:

$$Us^{\pm}_{sw} = \frac{\omega_0 F_0}{2} exp\left(-\frac{\tau}{\mu_0}\right)\int_{-1,0}^{0,1} P(\mu,\mu_0)d\mu \tag{2.31}$$

Thus in the upward direction Us can be thought of as some backward scattering fraction of the collimated source and in the downward direction as a forward scattering fraction. Since the phase function can be expanded in terms of Legendre polynomials the backward scattering fraction can be defined after Meador and Weaver (1980) as

$$\beta_0(\mu_0) = \frac{1}{2}\int_{-1}^{0} P(\mu,\mu_0)d\mu, \tag{2.32}$$

and the forward scattered fraction can be simply defined as $1-\beta_0$. Thus (2.31) can be expressed as follows:

$$\begin{aligned} Us^{+}_{sw} &= \omega_0 F_0 \beta_0 \exp\left(-\frac{\tau}{\mu_0}\right) \\ Us^{-}_{sw} &= \omega_0 F_0 (1-\beta_0) \exp\left(-\frac{\tau}{\mu_0}\right) \end{aligned} \tag{2.33}$$

This formulation has the distinct advantage that either the exact Legendre polynomial coefficients, produced from a Mie solution for the given microphysical parameters of a cloud layer, or some approximation such as a Henyey-Greenstein function can be used to approximate (2.32). The formulation also allows for both cloud particle and molecular scattering of radiation in the backward scattering function thus adding to the versatility of the model. Proceeding from this point as in section 2.2 to form the second order differential equation and solving by the undetermined coefficients method, the particular solutions representing the pseudo-source term given become:

$$\begin{aligned} Fs^{+}_{sw}(\tau) &= \omega_0 F_0 \frac{(t^{-}+\frac{1}{\mu_0})\beta_0 - b^{-}(1-\beta_0)}{(k_{+}+\frac{1}{\mu_0})(k_{-}+\frac{1}{\mu_0})} \exp\left(-\frac{\tau}{\mu_0}\right) \\ Fs^{-}_{sw}(\tau) &= \omega_0 F_0 \frac{(t^{+}-\frac{1}{\mu_0})(1-\beta_0) - b^{+}\beta_0}{(k_{+}+\frac{1}{\mu_0})(k_{-}+\frac{1}{\mu_0})} \exp\left(-\frac{\tau}{\mu_0}\right). \end{aligned} \tag{2.34}$$

Again as in the longwave case the total source contribution to the shortwave diffuse flux can be computed using (2.20).

2.4 Particle and Molecular Absorption

To model the radiative fluxes in a cirrus cloud environment, gaseous absorption in both the shortwave and longwave regions and Rayleigh scatter in the shortwave must be taken into account. In addition to these molecular processes, the scattering and absorption caused by the presence of cloud particles themselves must also be superimposed. These processes are incorporated in the model through the definition of the optical depth (τ), the single scattering albedo (ω_0), the asymmetry parameter (g) and the angular distribution function $P(\mu, \mu_0)$.

2.4.1 Calculation of Optical Depth

The total optical depth in the longwave and shortwave spectral regions is obtained from the sum of the optical depths determined by each separate radiative process in those

regions respectively,

$$\begin{aligned} \tau_{lw} &= \tau_{cloud} + \tau_{gas} + \tau_{e-type} \\ \tau_{sw} &= \tau_{cloud} + \tau_{gas} + \tau_{Rayleigh}. \end{aligned} \tag{2.35}$$

The optical depths associated with the scattering and absorption of radiation by cloud particles are determined as

$$\tau_{cloud} = \sigma_{ext}\Delta z \tag{2.36}$$

where σ_{ext} is the total particle extinction in the layer in km^{-1} and Δz is the thickness of the layer in km over which σ_{ext}. The particle extinction in a layer is determined from Mie theory given information about the number and size of the ice crystals.

The optical depth due to molecular absorption can be determined similarly as follows:

$$\tau_{gas} = ku \tag{2.37}$$

where u is the optical path of a particular absorbing gas of the layer having units of $g \cdot cm^{-2}$ and k represents the absorption of radiation by that gas in the layer and has units $cm^2 \cdot g^{-1}$. The optical path used in this study for each layer is

$$u = \left(\frac{\overline{p}}{p_{ref}}\right)^n \left(\frac{T_{ref}}{\overline{T}}\right)^m \frac{\overline{w}\Delta p}{g_r} \tag{2.38}$$

where $\overline{p}$ and $\overline{T}$ represent the mean pressure and temperature for that layer, p_{ref} and T_{ref} are the reference temperatures and pressures at which k is defined and the n, m powers which will be chosen depending on how the k used above was computed. $\overline{w}$ is the mean mixing ratio of the particular gas in the layer of Δp thickness and g_r is the acceleration due to gravity. There are a number of methods to determine the value of k including the sum of exponentials and the K-distribution methods. The latter method will be most extensively used in this model and its implementation is discussed in the Chapter 3.

For long wavelengths, another physical process that contributes to the absorption of radiation is the water vapor continuum absorption which varies according to the partial pressure of water vapor in the layer. This type of absorption, known as e-type absorption, is especially important when dealing with clouds in transparent regions of the clear sky absorption spectrum and significant errors can occur if not taken into account. The value

of k used in this study is computed via the empirical function of Roberts *et al.*, (1976). The empirical fit is given as follows after Stephens (1984):

$$k_{e-type} = \frac{\Phi(\overline{T})}{\Phi(T_0)}\Psi(\nu, T_0)e_c \tag{2.39}$$

where

$$\Phi(T) = exp\frac{1800}{T},$$

$$\Psi(\nu, T_0) = c_1 + c_2 \exp -c_3\overline{\nu}$$

and $e_c = e_{H_2O} + \gamma(\overline{p} - e_{H_2O})$. $T_p = 1800°K$, $T_0 = 296°K$, $c_1 = 4.2cm^2 \cdot g^{-1} \cdot atm^{-1}$, $c_2 = 5588cm^2 \cdot g^{-1} \cdot atm^{-1}$, $c_3 = .00787cm$, $\overline{\nu}$ is the mean wavenumber of a spectral band, $\overline{T}$ is the mean temperature in $°K$ for this layer, $\gamma = 0.002$ representing a pressure broadening correction (see Kneizys *et al.*, 1980), $\overline{p}$ and e_{H_2O} are the mean pressure and partial pressure of water vapor in *atm* respectively. This optical depth is calculated as τ_{gas} in (1.28), using the optical path due to water vapor in the layer.

For short wavelengths, the contribution to optical depth by Rayleigh scatter is computed using the empirical fit presented by Paltridge and Platt (1976). Their equation provides the optical depth for a path extending from the top of the atmosphere to a height $H(\text{in}km)$ above the surface

$$\tau_{Rayleigh} = .0088\lambda^{(-4.15+0.2\lambda)}e^{(-0.1188H-0.00116H^2)} \tag{2.40}$$

where λ is the wavelength (μm). This formula is used to calculate the optical thickness of a layer in the atmosphere with the height of the top and bottom of the layer given.

2.4.2 Scaling of the Single Scatter Albedo, Asymmetry Parameter and Direct Backscattered Fraction

The single scatter albedo and asymmetry factor are next determined. The Mie solution provides values of the single scatter albedo ω_0 and the asymmetry factor g due to cloud particles. A scaling correction presented by Slingo and Schrecker (1982), will be

employed to account for molecular scattering and absorption. The scalings in the long and short wavelengths for ω_0 and g are given as follows:

$$\begin{aligned} \omega_{0_{lw}} &= \frac{\omega_{cloud}\,\tau_{cloud}}{\tau_{lw}} \\ \omega_{0_{sw}} &= \frac{\tau_{Rayleigh}+\omega_{cloud}\tau_{cloud}}{\tau_{sw}} \end{aligned} \tag{2.41}$$

$$g_{sw,lw} = g_{cloud}\left(\frac{\omega_{cloud}\,\tau_{cloud}}{\omega_{sw,lw}\,\tau_{sw,lw}}\right) \tag{2.42}$$

where the subscripts *cloud*, *Rayleigh* and *gas* refer to the scattering and absorption from the cloud particles (as provided by Mie solutions), Rayleigh scatter and gaseous absorption respectively. In (2.41) $\omega_{Rayleigh}$ was omitted because it is never different from unity. It should be noted here that g and ω_0 are now a function of the total optical depth which inherently include the contribution to optical depth, by molecular scattering and absorption as described in the previous section.

At short wavelengths, the presence of Rayleigh scatter also affects the the phase function ($P(\mu,\mu_0)$) and therefore the backward scattering fraction determined from (2.32). In order to account for this effect the phase function for Rayleigh scatter and the cloud particles are weighted according to the relative scattering importance as follows:

$$P(\mu,\mu_0) = \frac{\tau_{Rayleigh}P_{Rayleigh} + \omega_{cloud}\tau_{cloud}P_{cloud}}{\tau_{Rayleigh} + \omega_{cloud}\tau_{cloud}}. \tag{2.43}$$

An example of the effect of the weighting in (2.43) is shown in Figure (2.3) which illustrates the change in the Henyey-Greenstein function (taken to represent cloud droplet scattering) as the optical depth of the Rayleigh scatter is increased. It is through the simple scalings shown in this section for ω_0, g and $P(\mu,\mu_0)$ that atmospheric radiative processes other than absorption and scattering by cloud particles are included in the two stream radiative transfer model.

2.5 Multi-layer Solution

To this point, only the monochromatic two stream radiative transfer model has been given for specified environmental parameters such as temperature and pressure, along with gaseous concentrations and microphysical parameters of the cloud particles.

2.5.1 The Adding Method

A multi-layer solution to the radiative transfer problem is obtained using the adding method which is described by Stephens and Webster (1979). Only an outline of the method is described here. The geometric configuration relevant to adding is presented in Figure 2.4.

The essence of the approach is that it provides fluxes using a recursive formula. The upward and downward fluxes at the top and bottom of a layer between levels l and $l+1$ respectively, can be represented as follows (e.g., Stephens and Webster, 1979):

$$\begin{aligned} F^+(l) &= \frac{Tr^+(l)\ F^+(l+1)}{1-Re(1,l)\ R^-(l)} + V^+(l+\tfrac{1}{2}) \\ F^-(l+1) &= Re(1,l+1)\ F^+(l+1) + V^-(l+\tfrac{1}{2}) \end{aligned} \tag{2.44}$$

where

$$Re(1,l+1) = R^-(l) + \frac{Tr^-(l)\ Re(1,l)\ Tr^+(l)}{1-Re(1,l)\ R^-(l)}, \tag{2.45}$$

is the composite reflection of all $l+1$ layers above level $l+1$ and

$$\begin{aligned} V^-(l+\tfrac{1}{2}) &= \frac{Tr^-(l)\ V^-(l-\frac{1}{2})}{1-Re(1,l)\ R^-(l)} + \frac{Tr^-(l)\ Re(1,l)\ J^+(l+\frac{1}{2})}{1-Re(1,l)\ R^-(l)} + J^-(l+\tfrac{1}{2}) \\ V^-(l+\tfrac{1}{2}) &= \frac{Re(l)\ V^-(l-\frac{1}{2})}{1-Re(1,l)\ R^-(l)} + \frac{J^+(l+\frac{1}{2})}{1-Re(1,l)\ R^-(l)}. \end{aligned} \tag{2.46}$$

In these equations,

$$Tr^+(l) = \mathcal{T}^+(0),$$

$$Tr^-(l) = \mathcal{T}^-(\tau_l),$$

$$R^-(l) = \mathcal{R}^+(0),$$

$$J^+(l+\frac{1}{2}) = \mathcal{S}^+_{sw,lw}(0)$$

and

$$J^-(l+\frac{1}{2}) = \mathcal{S}^-_{sw,lw}(\tau_l)$$

where the superscript $+$ and $-$ refer to the upward and downward directions respectively. The coefficients $V^{\pm}$ and $Re(1,l)$ are calculated iteratively from the top of the atmosphere down and then the fluxes are calculated iteratively using those coefficients from the bottom up to the top of atmosphere. In these expressions, $T_r^{\pm}(l)$ and $R^-(l)$ are the transmission and reflection functions for each individual layer (the lth layer) and are provided from the two stream solutions (2.22).

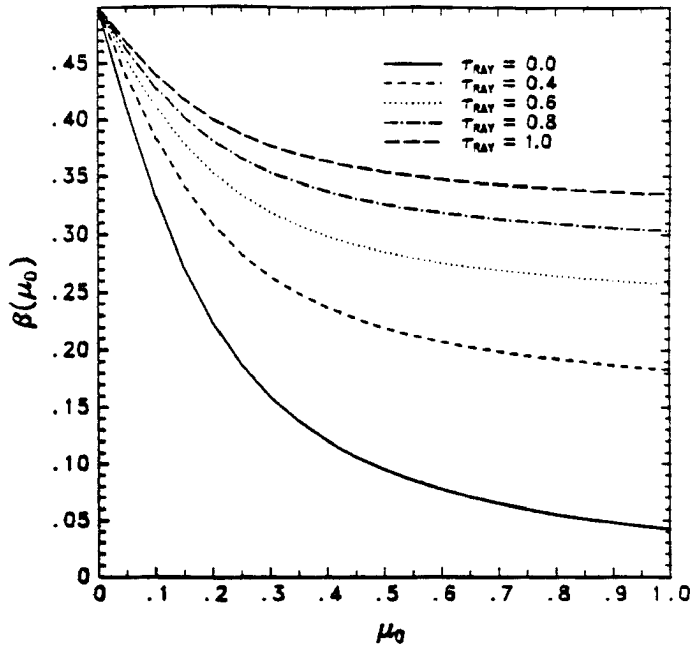

Figure 2.3: The Henyey-Greenstein direct backward scattering function weighted with the optical depth due to Rayleigh scatter where $g_{cloud} = .843$, $\omega_{cloud} = .9$ and $\tau_{cloud} = 1.0$

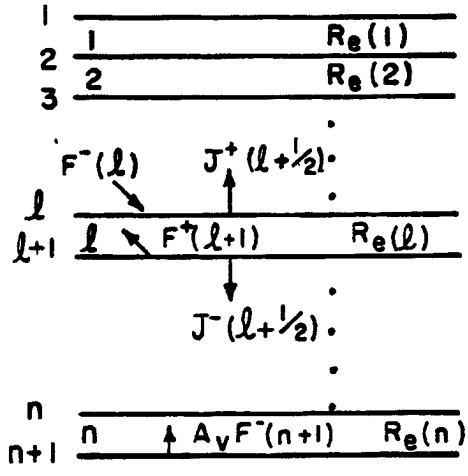

Figure 2.4: The layer configuration used in the adding method.

2.5.2 Boundary Conditions of the Diffuse Flux

Equations (2.44-2.46) require that boundary conditions be specified for the top and bottom of the atmosphere before the fluxes at each level of the atmosphere can be computed. The upper boundary conditions apply for the diffuse longwave and shortwave fluxes.

$$\begin{aligned} Re(1,1) &= 0 \\ F^{-}(1) &= F^{-}_{dif}(1) \\ V^{-}(\tfrac{1}{2}) &= F^{-}(1) \end{aligned} \tag{2.47}$$

where F^{-}_{dif} is simply the diffuse flux down at the top of the model atmosphere and generally $F^{-}_{dif}(1) = 0$ for both the long and short wavelength fluxes. The lower boundary condition ($l = n$) for the longwave and shortwave are based upon the Planck emission from the surface of the earth and the surface reflection respectively. The respective forms of the boundary conditions are:

$$\begin{aligned} F^{+}_{lw}(n+1) &= \pi B_{\nu}(Ts) \\ F^{+}_{sw}(n+1) &= \frac{A_{\nu}\left[V^{-}(n+\frac{1}{2}) + \mu_0 F_0 \exp\left(-\frac{\tau_{t_i}(n)}{\mu_0}\right)\right]}{1 - A_{\nu} Re(1,n+1)}. \end{aligned} \tag{2.48}$$

where $B_{\nu}(Ts)$ is the Planck emission function defined for a surface temperature Ts and a particular wavenumber ν, A_{ν} is the spectral albedo of the surface of the earth and $\tau_{t_i}(n)$ is the total optical depth at the atmosphere for a particular k_i. With these boundary conditions, the diffuse fluxes up and down at each level of the atmosphere can be completely determined using the adding method for a particular spectral band.

2.5.3 Computation of Heating Rates

Given the vertical profiles of the total upward and downward fluxes at any particular wavenumber band within the shortwave and longwave regions, the heating rate through a layer of the atmosphere is computed as

$$\frac{dT}{dt} = -\frac{g_r}{C_p}\frac{dF_{net}}{dp}. \tag{2.49}$$

where $F_{net} = F^{-}(l) - F^{+}(l)$ the net radiation at a specific level, g_r is the acceleration due to gravity and C_p is the specific heat of air. The heating rates are computed for each layer from the top down and thus $\Delta p < 0$ and $\Delta F_{net} = F_{net}(l-1) - F_{net}(l)$. Thus, the computation of heating rates concludes the two stream radiative transfer formulation.

2.6 Summary

The monochromatic multi-layer two stream model has been derived in this chapter assuming a plane parallel, horizontally homogeneous and azimuthally symmetric atmosphere. The general derivation has revealed the versatility of the model within the contents of the above assumptions. The physically meaningful representation of (2.19-2.21) gives added insight to the radiative transfer problem and allows for a multi-layer solution using the adding method which can be arranged to make use of stable matrix tridiagonal solvers (see Grant and Hunt, 1969; Toon *et al.*, 1988). Discussion of the division of both the long and short wavelength spectra and the molecular absorption in these intervals at this stage has been left vague. The spectra intervals that were chosen and the details of the treatment of molecular absorption are now described.

Chapter 3

GASEOUS ABSORPTION

In the previous chapter, the derivation and formulation of a monochromatic two stream model was presented. In order to compare the model results and aircraft observations, the calculated monochromatic fluxes must be integrated over the wavelength domain to match the observations. As discussed in the formulation of this model, the four parameters which determine the absorbing and scattering characteristics of the gases and particles within a layer of the atmosphere are the optical depth (τ), single scatter albedo (ω_0) and the asymmetry parameter (g) and an angular distribution function ($P(\mu, \mu')$). All of these parameters are functions of wavelength. Therefore to calculate a broadband flux, the spectral region must be divided into bands over which τ, ω_0, g and $P(\mu, \mu_0)$ can be assumed to vary smoothly. The optical depth, single scatter albedo, asymmetry parameter and angular distribution function derived for a specific wavelength band, from the cloud microphysics (defined as τ_{cloud}, ω_{cloud}, g_{cloud} and P_{cloud} in section 2.4) are calculated from Mie theory. The optical depths calculated from both the Rayleigh scatter and e-type absorption are known functions of wavelength and vary smoothly with wavelength. The extinction due to molecular absorption however, is a very highly nonlinear function of wavelength depending on the location and intensity of absorption lines, pressure and temperature. Thus, a method of computing extinctions and optical depth for a particular wavelength band must be employed which will allow a proper integration of monochromatic fluxes to broadband values. Such a method will therefore dictate the final form of the two stream model. The focus of this chapter is to discuss the broadband integration used in the model, to highlight this integration as it applies to gaseous absorption bands and then to provide results for various clear sky simulations as a test of the model.

3.1 Gaseous Absorption

As mentioned above, the implementation of a scheme to integrate over the gaseous absorption ultimately dictates the final form of the two stream model. The line by line calculation of gaseous absorption and subsequent integration is the most direct and accurate method but is computationally impractical for application in this study. There are two basically equivalent methods which allow treatment of gaseous absorption together with droplet extinction within a given spectral band. These are the sum of exponentials fit and the k-distribution method (see Stephens, 1984, for review). The K- distribution method is used in this study for most bands except for ozone absorption in the visible wavelengths ($.28\mu m$ - $.68\mu m$), in which case the sum of exponential method is used.

3.1.1 The K-Distribution

The k-distribution method is now described and its implementation is discussed in detail. Equation (2.37) defines the optical depth associated with gaseous absorption at a given wavelength. The purpose of the k-distribution approach is to provide representative values of k for a given spectral region and to represent the mean transmittance over some spectral interval $\Delta\nu$. The mean transmittance for a particular wavenumber band can be represented as

$$\mathcal{T}(u) = \frac{1}{\Delta\nu}\int_{\Delta\nu} e^{-k_\nu u} d\nu \tag{3.1}$$

and further transformed to k space the above becomes

$$\mathcal{T}(u) = \int_0^\infty f(k) e^{-ku} dk. \tag{3.2}$$

The k-distribution method defines a probability distribution function $f(k)$ such that $f(k)dk$ represents the fraction of the wavenumber interval for which a particular extinction lies between k and dk. More formally stated, for a homogeneous atmosphere, the transmission within a relatively wide spectral interval is independent of the ordering of the value k with respect to the wavenumber ν, but depends upon the fraction of the interval that is associated with a particular value k (from Arking and Grossman, 1972). Stephens (1984) summarized the results from Hansen *et al.* (1983) showing that the k-distribution

method provides an accurate method of treatment of vertical inhomogeneity and noting that the strongest and weakest absorption occurs at the same frequency at all altitudes. This allows the pressure effects to be included explicitly in the choice of k (see figure 3.1).

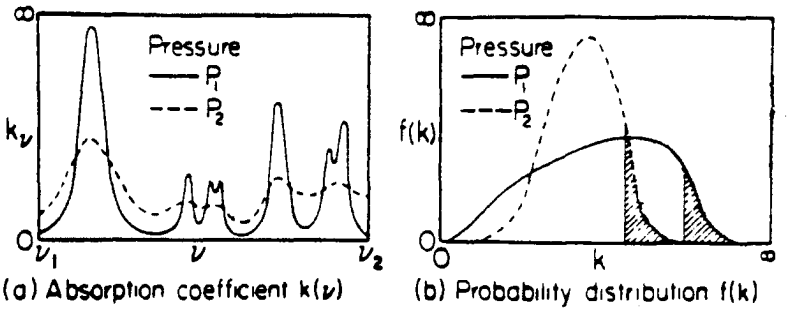

Figure 3.1: A schematic illustration portraying the essence of the k-distribution method. A schematic of absorption line spectra at two different pressures are shown in (a). In (b) the two probability density functions $f(k)$ associated with (a) are illustrated. The shaded area depicts the strongest absorption (i.e., largest k) for the same spectral interval (i.e., $f(k)$ for different pressures are correlated). Integrations of $f(k)$ over k replaces the integration of k_ν over ν (from Stephens, 1984).

Discretizing the RHS of (3.2) results in the following expression:

$$\mathcal{T}(u) \approx \sum_{i=1}^{n} w_i e^{-k_i u} \tag{3.3}$$

where n is the total number of extinction values k_i in the band and w_i is the weight representing the fraction of the wavenumber band with k_i as the extinction.

3.1.2 Implementation of the K-distribution Method

With the approximation (3.3) a set of n optical thicknesses must be used to represent the mean transmission in the spectral band $\Delta\nu$. These are defined as:

$$\tau_{gas_i} = k_i u. \tag{3.4}$$

where $i = 1, \ldots, n$. Associated with this set of optical depths are the weights w_i. Therefore the weights must be applied at some point in the model in order for gaseous absorption to be properly represented. Since the intensity and the flux are both a function of τ, they therefore must be a function of τ_{gas_i} as above and the following must also be true:

$$\begin{aligned} \tau_{lw_i} &= \tau_{cloud} + \tau_{gas_i} + \tau_{e-type} \\ \tau_{sw_i} &= \tau_{cloud} + \tau_{gas_i} + \tau_{Rayleigh}. \end{aligned} \tag{3.5}$$

Thus a set of n different τ's are defined for each band. The flux solutions for the two stream model solved for each τ_i are represented as $F_i^{\pm}(\tau_i)$ and the broadband flux at some level in a layer for a particular interval $\Delta\nu$ is found using

$$F_{\Delta\nu}^{\pm} = \sum_{i=1}^{n} w_i F_i^{\pm}(\tau_i). \tag{3.6}$$

There are many bands within the long and short wavelength regions where two or more gases are absorbing in the same spectral region. This gas overlap needs to be taken into account and is done so in this study by assuming the following:

$$T_{12} \approx \left(\sum_{i=1}^{n_1} w_{1i} e^{-k_{1i}u}\right)\left(\sum_{j=1}^{n_2} w_{2j} e^{-k_{2j}u}\right) \approx \sum_{i=1}^{n_1}\sum_{j=1}^{n_2} w_{1i} w_{2j}\ e^{-u(k_{1i}+k_{2j})} \tag{3.7}$$

in which case the optical depth becomes:

$$\tau_{ij} = u(k_{1i} + k_{2j}) \tag{3.8}$$

and the resulting fluxes can be found by:

$$F_{\Delta\nu}^{\pm} = \sum_{i=1}^{n_1}\sum_{j=1}^{n_2} w_{1i} w_{2j} F_{ij}^{\pm}(\tau_{ij}). \tag{3.9}$$

The k-distribution method has another advantage in that the distribution function can be calculated at any reference temperature and pressure. Thus the scaling approximation, which can be quite inaccurate for the upper atmosphere given reference temperatures of the surface, can be improved greatly by using a k-distribution based on a specifically chosen reference temperature and pressure. The k-distributions for a number of different absorbing gases is discussed in a series of papers (see Chou and Arking, 1980; Chou and Arking, 1981; Chou and Peng, 1983; Chou, 1984) which show favorable comparisons to line-by-line calculations using scaling approximations with optimized reference temperature and pressure. These optimized scaling methods of Chou are used in this study.

3.1.3 Shortwave Ozone Absorption (ESF)

Due to the lack of k absorption data in the spectral region from 0.28 μm to 0.69 μm where ozone absorption becomes dominant, the sum of exponentials approach is adopted. Although the exponentials method is basically equivalent to the k-distribution in design,

it is conceptually very different. The exponential method fits the absorption lines of a particular gas over a specified spectral interval and is thus more empirical than the k-distribution approach. Since the method has exactly the same form as (3.3) it can be applied in exactly the same manner as the k-distribution method. However, it must be noted that the k_i's are not real extinction factors but are merely empirical parameters related to the exponential fit.

3.1.4 Gaseous K-Distribution and ESF Tables

K-distribution data is used for the following gases: water vapor and carbon dioxide in both the longwave and shortwave, ozone in the long wavelengths and oxygen in the short wavelengths and ESF data for ozone in the shortwave region. Table 3.1 lists each gas and the corresponding wavenumber limits of these bands. Note that only two gases are overlapped in any spectral region. The resolution of the K bands in the longwave is 20 cm^{-1} and in the shortwave is 50 cm^{-1}. This is an extremely fine resolution and may be unnecessary to for many studies, however the resolution is very useful when examining spectral variability of fluxes. Given the intervals of Table 3.1 and the resolution previously stated, the total number of bands in the long wavelengths become 130 while 249 bands, including 11 bands of exponential sum fitting of ozone absorption, are used to resolve the solar spectrum. Table 3.1 also shows that there are 19 and 59 overlapped bands in the long and short wavelengths respectively. Tables 3.2 and 3.3 show the reference temperatures, pressures and scaling powers (n, m) used to calculate the optical path (u see eq. 2.38) in the infrared and solar wavelengths respectively. In the infrared the scaling parameters are determined separately for absorption band centers and wings of both H_2O and CO_2 after Chou and Arking (1980) and Chou and Peng (1983). The function $\overline{R}(T, T_{ref})$ represents the mean effect of the temperature on the absorption coefficient as defined by Chou and Arking (1980). The smooth behavior of $\overline{R}(T, T_{ref})$ with T allows an exponential or quadratic fit to specify the variation of $\overline{R}$ with T given the computed values shown in Table 3.2.

Table 3.1: Bandwidths of Absorbing Gases

Gas	Infrared		Solar	
	Bandwidths (cm^{-1})	Bands	Bandwidths (cm^{-1})	Bands
H_2O	20 - 2620	130	2600 - 14450	237
CO_2	540 - 800	13	3300 - 4000, 4600 - 5300, 6000 - 7000	48
O_3	980 - 1100	6	14550 - 35710	11
O_2	-	-	12850 - 13150, 14300 - 14550	11

Table 3.2: Infrared scaling parameters.

Gas	Bandwidths (cm^{-1})	P_{ref} (mb)	n	T_{ref} (^oK)	m	$\overline{R}(T_{ref}-40^oK, T_{ref})$	$\overline{R}(T_{ref}+40^oK, T_{ref})$
H_2O Centers	20 - 340, 1380 - 1900	275	1.00	225	0.0	0.90	1.16
Wings	340 - 1380, 1900 - 3000	550	1.00	256	0.0	0.58	1.78
CO_2 Centers	620 - 720	30	0.85	240	0.0	0.74	0.44
Wings	540 - 620, 720 - 800	300	0.50	240	0.0	0.51	2.03
O_3	980 - 1100	100	1.00	240	1.0	-	-

Table 3.3: Solar scaling parameters.

Gas	$P_{ref}(mb)$	n	T_{ref} (^oK)	m
H_2O	300.00	0.800	240.00	0.000
CO_2	300.00	1.750	240.00	1.375
O_3	1013.25	0.400	273.15	1.375
O_2	500.00	1.750	240.00	1.375

3.1.5 Clear Sky Models

In simulating the clear sky fluxes, the vertical profiles of both temperature and the absorbing gases are required. The vertical profiles of moisture and other non-uniformly mixed gas concentrations are used to calculate the optical paths (2.38) from the scaling approximation which when multiplied by a specific k value yields the optical depth for the particular k interval. For clear sky simulations, the soundings presented by McClatchey *et al.* (1972) which contain information about both moisture and ozone concentrations at different latitudes and seasons are employed. The McClatchey soundings have 33 atmospheric levels, in which the bottom 25 have $1km$ resolutions. Figures 3.2 and 3.3 show the temperature and moisture profiles for the tropical, mid-latitude summer and winter soundings as given by McClatchey.

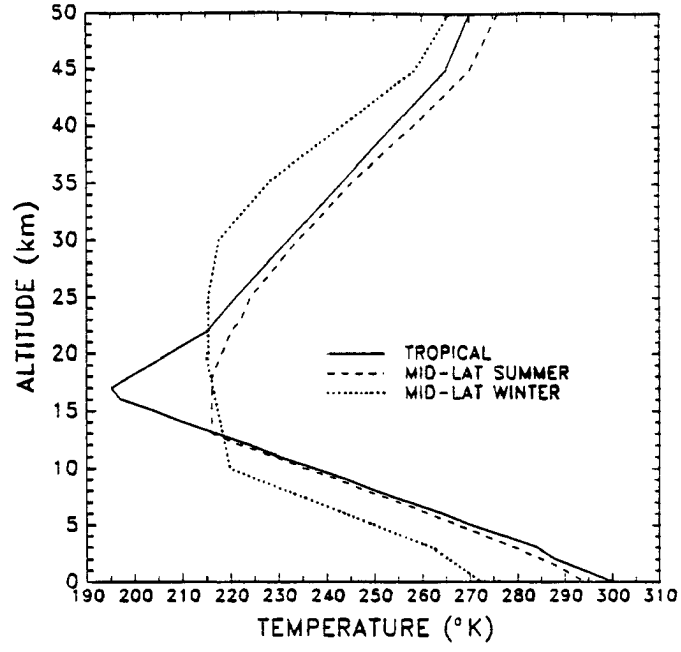

Figure 3.2: McClatchey temperature profiles ($°K$) for the tropical, mid-latitude summer and winter. (McClatchey *et al.*, 1972)

3.2 Longwave Clear Sky Simulations: Difficulties and Solutions

Now that the methods which account for gaseous absorption have been developed, clear sky simulations in the longwave are performed to evaluate the performance of the

model. Simulations of clear sky fluxes with the present model revealed negative downward fluxes at high altitudes associated with particular k intervals and these erroneous results produced numerically noisy heating rates (figure 3.4). Analysis showed that the negative fluxes resulted from the loss of numerical precision in the formulation of chapter 2 (equations 2.19-2.21; 2.25,2.26). The following subsection describes the sources of the numerical instabilities and the corresponding modifications to the formulations to overcome these problems.

3.2.1 Numerical Instabilities

The numerical instabilities encountered arose from the particular form of the longwave source terms (2.28) and the transmittance and reflectance functions (2.22,2.23) used. The problem appears in the clear sky longwave simulation because of the extreme range of optical depths encountered. This range in optical depths is a result of the absorption which varies from large values associated with the center of strong absorbing bands, to low values for weak absorption in the wings. This range was approximately 16 orders of magnitude. Very large optical depths ($> 10^2$) resulted in numerical difficulties in the calculation of the reflectance and transmittance terms, due to the presence of positive exponential factors in (2.22) while very small optical depths ($< 10^{-8}$) caused problems in evaluating the source terms due to presence of the term defined by (2.26).

3.2.2 Reformulation of Transmittance and Reflectance Terms

Examining (2.22) and noting that $k_- \leq 0 \leq k_+$, as shown by Preisendorfer, it can be seen that a negative exponential is subtracted from a positive exponential in both the numerator and denominator. For larger values of optical depth, the positive exponential is unbounded and becomes unstable while the negative exponential approaches zero. Thus the form of the reflectance and transmittance equations must be changed to avoid this problem. This can be done simply by dividing the top and bottom of these coefficients by the largest positive exponential term. Thus the transmittance and reflectance coefficients

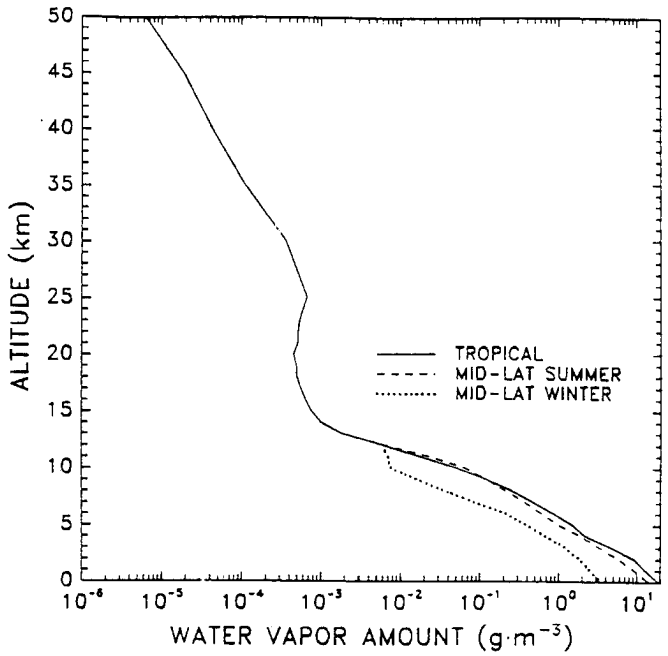

Figure 3.3: McClatchey water vapor density profiles ($g \cdot m^{-3}$) for the tropical, mid-latitude summer and winter. (McClatchey *et al.*, 1972)

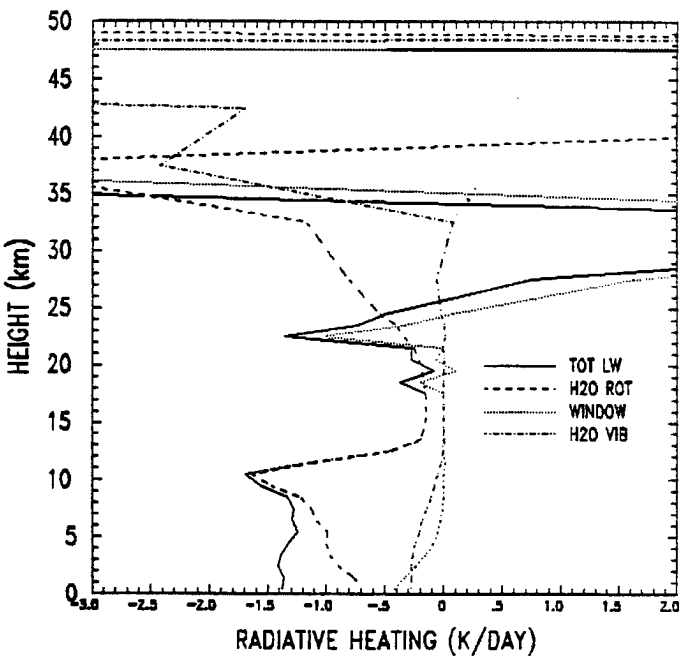

Figure 3.4: LW heating rates ($°K/day$) as a result of numerical instability for mid-latitude summer atmospheric profile.

become:

$$\begin{aligned}
\mathcal{T}(0,\tau,\tau_1) &= \tfrac{1}{\Delta(\tau_1)}\left[\eta_+^+\eta_-^- \exp(k_-\tau) - \eta_+^-\eta_-^+ \exp(k_+(\tau-\tau_1) + k_-\tau_1)\right] \\
\mathcal{R}(0,\tau,\tau_1) &= \tfrac{\eta_+^+\eta_-^+}{\Delta(\tau_1)}\left[\exp k_-\tau - \exp(k_+(\tau-\tau_1) + k_-\tau_1)\right] \\
\mathcal{T}(\tau_1,\tau,0) &= \tfrac{1}{\Delta(\tau_1)}\left[\eta_+^+\eta_-^- \exp k_+(\tau-\tau_1) - \eta_+^-\eta_-^+ \exp(k_-\tau - k_+\tau_1)\right] \\
\mathcal{R}(\tau_1,\tau,0) &= \tfrac{\eta_+^+\eta_-^+}{\Delta(\tau_1)}\left[\exp k_+(\tau-\tau_1) - \exp(k_-\tau - k_+\tau_1)\right]
\end{aligned} \tag{3.10}$$

where,

$$\Delta(\tau_1) = \eta_+^+\eta_-^- - \eta_+^-\eta_-^+ \exp\tau_1(k_- - k_+). \tag{3.11}$$

Noting that $\tau_1 \geq \tau$ it can be seen that all the exponential terms in the above equations are negative, thus avoiding the problem of the uncontrolled exponential growth.

3.2.3 Reformulation of Longwave Source Terms

A more subtle problem was discovered for small optical depths in the longwave source term formulations. As stated, the major source of numerical instability resulted from (2.26) which has optical depth in the denominator. For the small optical depths encountered in the extreme wings of absorption bands, (2.26) becomes extremely large with a loss of precision as a result. This loss of significant digits led to negative fluxes in the upper atmosphere noted above and to the erratic heating rate profile shown in Fig 3.4. This problem is avoided by combining the three terms of (2.20) into an alternative form representing the source upward from the top and downward from the bottom respectively as follows:

$$\begin{aligned}
\mathcal{S}_{l\omega}^+(\tau=0) &= \tfrac{2\pi(1-\omega_0)x^-}{v}\left\{B_\nu(T_0)\left(1-\tfrac{x^+}{x^-}\mathcal{R}^-\right) - \mathcal{T}^+B_\nu(T_1)\right. \\
&- \left.[B_\nu(T_1)-B_\nu(T_0)]\left[\tfrac{1-\mathcal{T}^++\mathcal{R}^-}{x^-\tau_1} + \tfrac{u(1-\mathcal{T}^+-\frac{x^+}{x^-}\mathcal{R}^-)}{v\tau_1}\right]\right\}
\end{aligned} \tag{3.12}$$

$$\begin{aligned}
\mathcal{S}_{l\omega}^-(\tau=\tau_1) &= \tfrac{2\pi(1-\omega_0)x^+}{v}\left\{B_\nu(T_1)\left(1-\tfrac{x^+}{x^-}\mathcal{R}^+\right) - \mathcal{T}^-B_\nu(T_0)\right. \\
&+ \left.[B_\nu(T_1)-B_\nu(T_0)]\left[\tfrac{1-\mathcal{T}^-+\mathcal{R}^+}{x^+\tau_1} + \tfrac{u(1-\mathcal{T}^-+\frac{x^-}{x^+}\mathcal{R}^+)}{v\tau_1}\right]\right\}
\end{aligned} \tag{3.13}$$

where for the reflectance and transmittance coefficients + is up and corresponds to $(\tau_1,\tau,0)$ and − is down and corresponds to $(0,\tau,\tau_1)$ and the remaining variables are defined as before. In (2.50) there is still division by τ_1 however, the numerator is of the same order as the denominator. This can be most easily seen by reducing the equations for the clear sky no scatter case. In this case $\omega_0 = 0$, $\mathcal{R} = 0$ and solving for the fluxes at the top

or bottom of the layer $\mathcal{T} = exp(-k_+\tau_1)$. For $\tau_1 \ll 1$ the Taylor series expansion gives $\mathcal{T} \approx 1 - k_+\tau_1$ and since $x^{\pm}$ and $k_{\pm}$ are of the same order of magnitude, the division is a more stable operation producing a result on the order of 1.

3.2.4 Longwave Simulation Cases

Once the numerical difficulties are overcome, the model was run and produced satisfactory results. In order to evaluate the performance of the model, results of the present model with gaseous absorption are compared to results presented by others using different and more established methods. The model results must be evaluated in both the longwave and the shortwave. Figure 3.5 presents the vertical profile of longwave heating for water vapor absorption for a mid-latitude summer atmosphere model. The heating rates are divided into three major absorbing bands: the rotation band, the vibration band and the continuum for which e-type absorption is not taken into account. Figure 3.6 shows the resulting heating rates for the mid-latitude summer atmosphere for the three important absorbers in the longwave H_2O, CO_2 and O_3 separately and then combined.

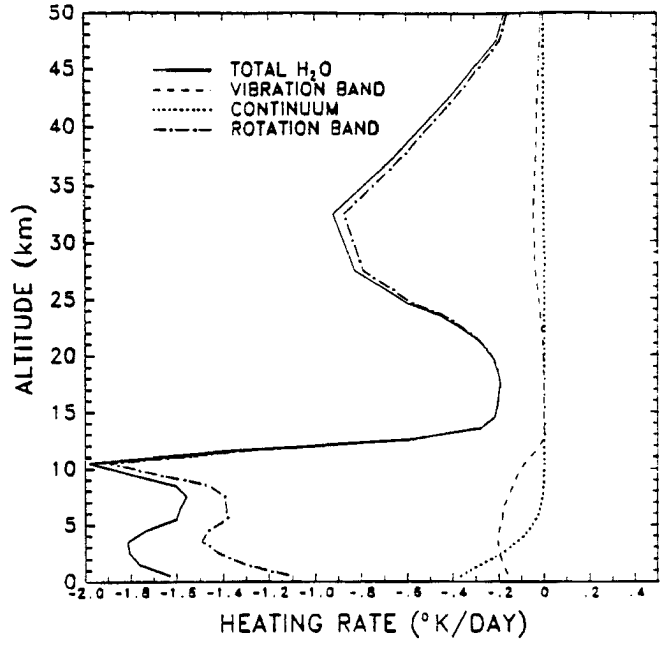

Figure 3.5: LW radiative heating rates ($°K/day$) in mid-latitude summer atmosphere for H_2O. Contribution of rotation, window and vibration bands in the LW are shown.

Figure 3.7 shows a comparison between the standard GFDL line by line model as provided by Luther (1985) and the present model for the combined effect of the three important infrared absorbers H_2O, CO_2 and O_3. The comparisons reveal that the heating rates produced by the present model agree within $0.3^oK/day$ throughout the atmosphere up to about 50 *mb*. Luther observed the differences between various line-by-line models to be within $0.3^oK/day$. Above 50 *mb* discrepancies increase dramatically showing excessive cooling. Table 3.4 compares fluxes at certain levels of the GFDL line-by-line calculations for CO_2 only in the midlatitude summer atmosphere for concentrations of 300 and 600 ppmv. Table 3.5 shows the absorbed flux above the tropopause, within the troposphere and within the entire atmosphere as computed from Table 3.4. The two stream results show an increased divergence above the tropopause and decreased divergence in the troposphere compared to the line-by-line results. Therefore the two stream model predicts greater emission above the tropopause and less emission below the tropopause than the line-by-line models. Table 3.5 also shows that the deficient emission in the troposphere dominates and thus the emission of the entire atmosphere for the two stream model is less than that of the line-by-line models. The cooling rates in the troposphere due to CO_2 ($\approx 0.15^oK/day$) absorption are generally less than 10% of the cooling rates due to H_2O bands and therefore do not constitute significant error in the tropospheric cooling rates.

By contrast, the higher emission of CO_2 throughout the stratosphere leads to errors in the radiative cooling as high as a factor of 2 compared to line-by-line models as shown in figure 3.7. The excessive emission of CO_2 above the tropopause and deficient emission below by the present model points to possible problems in the scaling parameters used to weight the optical path u. These results indicate that the optical path is too long in the stratosphere and too small in the troposphere and that the errors in the stratospheric optical path are exaggerated by the relative thinness of the stratosphere as compared to the troposphere.

This apparent CO_2 scaling problem requires further examination especially if the present model is to be used to investigate stratospheric phenomenon or the sensitivity of atmospheric radiative properties to increasing CO_2 concentrations. However, relative

Table 3.4: Infrared flux comparison of line-by-line (LBL) calculations to the present model for CO_2 emission in a mid-lat summer atmosphere (all units in $W \cdot m^{-2}$, τ^* corresponds to the total optical depth of the atmosphere and τ_{trop} represents the optical depth from the top of atmosphere to the tropopause, line-by-line data from Luther,1985).

ppmv of CO_2	Model	$F^+(\tau^*)$	$F^-(\tau^*)$	$F_{net}(\tau^*)$	$F_{net}(\tau_{trop})$	$F^+(0)$
300	GISS	423.57	75.36	348.21	371.49	384.33
	GFDL	423.57	75.38	348.19	371.96	384.54
	LMD	423.57	76.38	347.19	371.04	383.52
	Mean LBL	423.57	75.71	347.86	371.50	384.13
	2-stream	423.47	60.65	363.92	373.86	391.92
	Abs. error	0.10	15.06	-16.06	-2.36	-7.79
	Rel. error %	0.02	19.9	4.6	0.6	2.0
600	GISS	423.57	83.50	340.07	364.61	380.05
	GFDL	423.57	83.60	339.97	365.10	380.27
	LMD	423.57	84.20	339.37	364.45	379.51
	Mean LBL	423.57	83.77	339.80	364.72	379.94
	2-stream	423.47	65.29	358.18	371.88	391.16
	Abs. error	0.10	18.48	-18.38	-7.16	-11.22
	Rel. error %	0.02	22.1	5.4	2.0	3.0

GISS - Goddard Institute for Space Studies

GFDL - Geophysical Fluid Dynamics Laboratory

LMD - Laboratoire de Meteorolgie Dynamique

Table 3.5: As Table 3.4 but showing the absorbed radiation from the top of the atmosphere to the tropopause (ΔF_{TT}), from the tropopause to the surface (ΔF_{TS}) and the entire atmosphere (ΔF_{ATM}). $\Delta F_{TT} = F_{net}(\tau_{trop}) - F^+(0)$, $\Delta F_{TS} = F_{net}(\tau^*) - F_{net}(\tau_{trop})$ and $\Delta F_{ATM} = F_{net}(\tau^*) - F^+(0)$.

ppmv of CO_2	Model	ΔF_{TT}	ΔF_{TS}	ΔF_{ATM}
300	Mean LBL	-12.63	-24.31	-36.94
	2-stream	-18.06	-9.94	-28.00
	Abs. error	5.43	-14.37	-8.94
600	Mean LBL	-15.22	-24.92	-40.14
	2-stream	-19.28	-13.70	-32.98
	Abs. error	4.06	-11.22	-7.16

errors in the fluxes due to the presence of all three long wavelength absorbers are within 5% (see Table 3.6) with the exception of the net flux at the surface which has an absolute error that is within the $30W \cdot m^{-2}$ range that other approximate schemes used by the scientific community were reported by Luther to produce. Figure 3.8 shows the heating rates resulting from the inclusion of continuum or e-type absorption the effects of which are mainly confined to the lowest levels. The downward flux at the surface ($321.2\, W \cdot m^{-2}$) agrees to within $1\ W \cdot m^{-2}$ to the value obtained from the LMD line- by-line model (see figure 8, Luther,1985).

Table 3.6: Infrared comparison of line-by-line (LBL) calculations to the present model for H_2O+CO_2+O_3 absorption for a mid-lat summer atmosphere.

Model	$F^+(\tau^*)$	$F^-(\tau^*)$	$F_{net}(\tau^*)$	$F_{net}(\tau_{trop})$	$F^+(0)$
LMD	423.09	302.80	120.29	277.30	293.69
GFDL	423.15	303.46	119.69	278.30	294.42
Mean LBL	423.12	303.13	119.99	277.80	294.05
2-stream	423.47	288.22	135.25	283.21	307.79
Abs. error	0.35	14.91	-15.26	-5.41	-13.74
Rel. error %	0.08	4.9	12.7	1.9	4.7

3.3 Shortwave Clear Sky Simulations: Difficulties and Solutions

The reformulation of the reflectance and transmittance functions as described above is also required for the shortwave model to avoid any numerical difficulties resulting from exponential growth in these terms. However, another problem became apparent during sample simulations which shall be described below. Once this problem was addressed, clear sky simulations of the shortwave were able to be performed.

3.3.1 Singularity of Shortwave Source Term

A problem was encountered in the shortwave source term (refer to equation 2.25) for which a singularity occurred when $k_- = -\frac{1}{\mu_0}$. Because $k_- \leq 0$ and $\frac{1}{\mu_0} \geq 1$ this singularity can occur when $k_- \leq -1$. An example of this problem arose when considering gaseous absorption in the shortwave with a solar zenith angle of 60.0°. In this case $k_- = -2$ and $\frac{1}{\mu_0} = 2$ and a division by zero resulted. Unlike the problem encountered

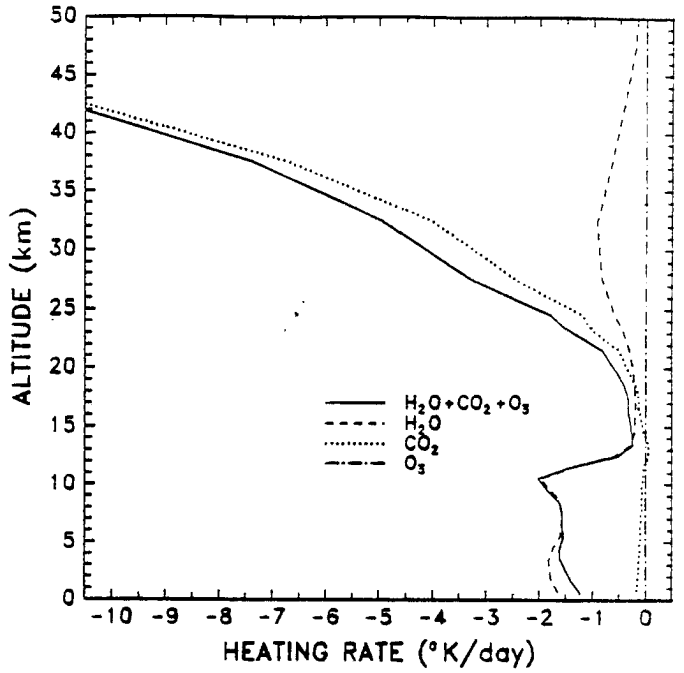

Figure 3.6: LW radiative heating rates ($°K/day$) in mid-latitude summer atmosphere for H_2O, CO_2 and O_3 and their combined effect. (CO_2 concentration of 330ppm.)

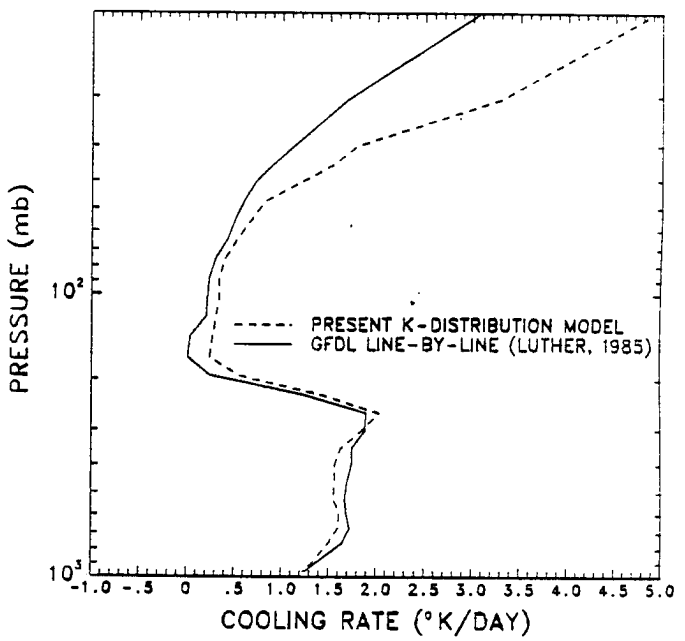

Figure 3.7: Comparison of the radiative cooling rates ($°K/day$) for the combined cooling of H_2O, CO_2 and O_3 between the present model and the GFDL line by line model presented by Luther (1984). (CO_2 concentration of 330ppm.)

in the infrared wavelengths, this is not a new problem to the two stream solution in the shortwave. Zdunkowski (1980) and King and Harshvardhan (1986) outline ways to overcome this problem. Zdunkowski lets $\mu_0 = \mu_0 + \delta\mu_0$ while King and Harshvardhan solve the two stream differential equation for this specific case. The later method of avoiding this problem is chosen here for completeness.

The differential equations (2.14) are solved for the case when $k_- = -\frac{1}{\mu_0}$ resulting in a form of the particular solution containing a linear and exponential dependence on τ. The particular solutions are represented as

$$\begin{aligned} Fs^+_{sw}(\tau) &= \omega_0\mu_0^2\tau F_0 \frac{(t^- + \frac{1}{\mu_0})\beta_0 - b^-(1-\beta_0)}{[\tau(1-\mu_0 u + \mu_0^2 v) + \mu_0(\mu_0 u - 2)]} \exp -(\tfrac{\tau}{\mu_0}) \\ Fs^-_{sw}(\tau) &= \omega_0\mu_0^2\tau F_0 \frac{(t^+ - \frac{1}{\mu_0})(1-\beta_0) - b^+\beta_0}{[\tau(1-\mu_0 u + \mu_0^2 v) + \mu_0(\mu_0 u - 2)]} \exp -(\tfrac{\tau}{\mu_0}) \end{aligned} \tag{3.14}$$

where u and v are defined by (2.29). If $D+ = D^- = D$, $b^+ = b^- = b$ then $t^+ = t^- = t$, $u = 0$ and referring to (2.17) $v = -\frac{1}{\mu_0}$. Therefore the above particular solutions reduce to

$$\begin{aligned} Fs^+_{sw}(\tau) &= \tfrac{1}{2}\omega_0\mu_0\tau F_0 \left[b\,(1-\beta_0) - (t + \tfrac{1}{\mu_0})\beta_0\right] \exp\left(-\tfrac{\tau}{\mu_0}\right) \\ Fs^-_{sw}(\tau) &= \tfrac{1}{2}\omega_0\mu_0\tau F_0 \left[b\,\beta_0 - (t - \tfrac{1}{\mu_0})(1-\beta_0)\right] \exp\left(-\tfrac{\tau}{\mu_0}\right) \end{aligned} \tag{3.15}$$

which have no singularity.

3.4 Shortwave Simulation Cases

Figure 3.9 and 3.10 show a comparison between the heating rates in the atmosphere, due to the absorption of water vapor for the tropical and mid- latitude winter soundings respectively of the present two stream model and the line by line results published by Chou and Arking (1981). The error is within $0.03°K/day$ throughout the mid-latitude winter atmosphere and agrees even more closely at the altitude typical of where cirrus clouds form. In the tropical case the error is within $0.1°K/day$ near the surface and decreases with increasing altitude. The sharp discontinuities in the heating rates have been replicated well and the slight displacements can be attributed to differences in the altitude of the levels inside the model. Figure 3.11 shows the heating rates in the mid-summer atmosphere due to all the important shortwave absorbers (H_2O, CO_2, O_2 and

O_3). Note the characteristic increase in absorption by ozone in the atmosphere and the increase of absorption by carbon dioxide about the 100 mb level. Figure 3.12 presents the effect of Rayleigh scatter in the mid-latitude summer atmosphere. The total downward flux at the surface is approximately 6% less with the inclusion of Rayleigh scatter than without. From these diagrams it can be seen that the shortwave radiative heating rates, due to the gaseous absorption, are in excellent agreement with previously published data.

3.5 Summary

In this chapter two stream modeling of gaseous absorption has been described in the long and short wavelength spectral regions. The numerical difficulties encountered and the reformulation necessary to overcome them has also been presented in detail. Recognition of the numerical instabilities in the infrared wavelengths and the means to overcome them is new. Lastly, clear sky calculations using the models have been performed. Agreement of infrared fluxes down at the surface and up at the top of the atmosphere are within 5% of the line-by-line fluxes for CO_2+O_3+H_2O while the net flux at the tropopause agrees within 2%. Luther (1984) shows these fluxes to be within the range of comparative narrow band models (6% of mean). Solar clear sky results showed agreement within 0.1 $^{o}K/day$ of the line-by-line results of Chou and Arking (1981). It now remains to establish the ability of the model to simulate the transfer of radiation throughout a cloudy atmosphere. This will be the subject of the next chapter along with various theoretical cirrus simulations.

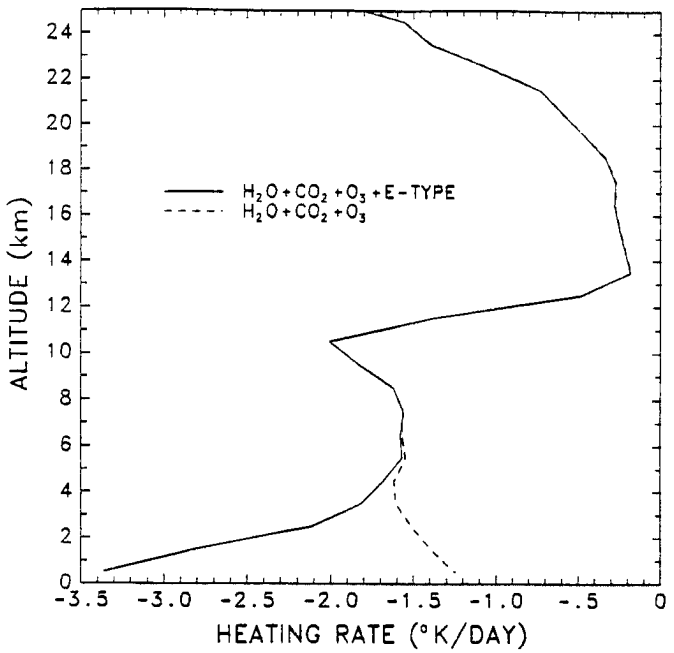

Figure 3.8: LW radiative heating rates ($°K/day$) in mid-latitude summer atmosphere for the combined effect of H_2O, CO_2 and O_3 and e-type absorption.

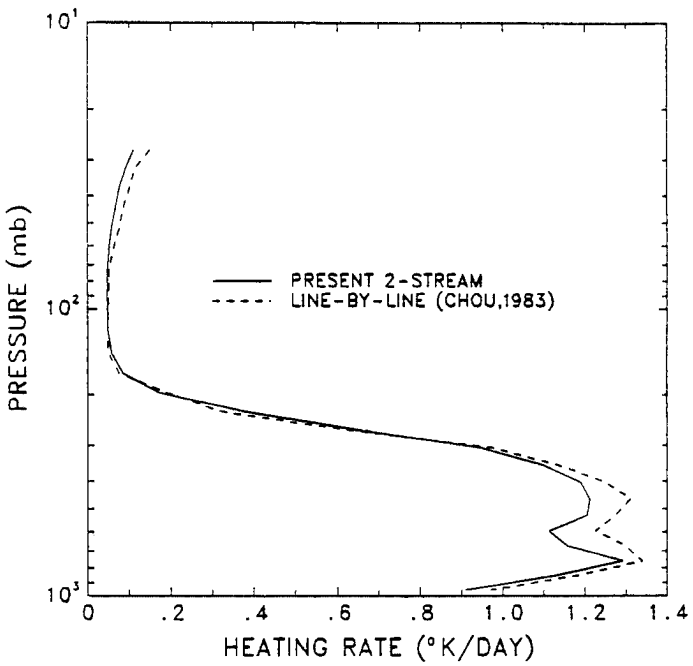

Figure 3.9: Comparison between SW radiative heating rates ($°K/day$) in the tropical atmosphere for H_2O between the present model and the line by line solution presented by Chou and Arking (1981).

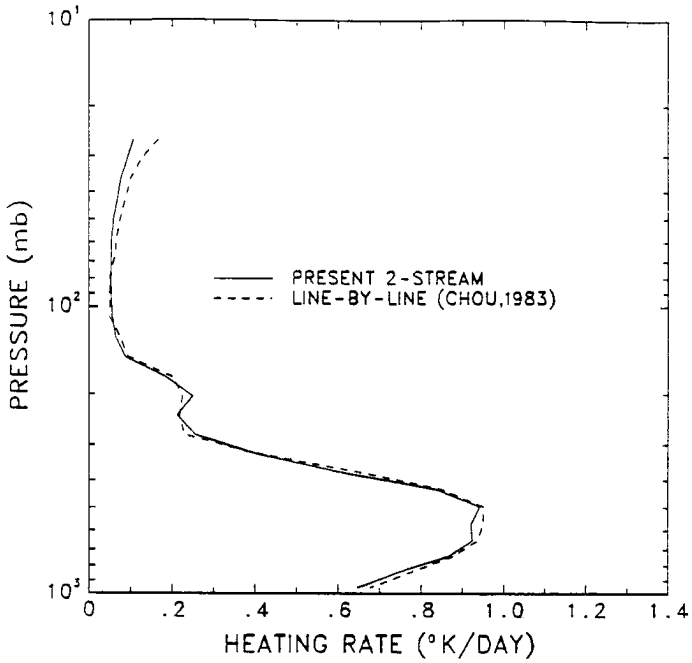

Figure 3.10: Comparison between SW radiative heating rates ($°K/day$) in the mid-latitude winter atmosphere for H_2O between the present model and the line by line solution presented by Chou and Arking (1981).

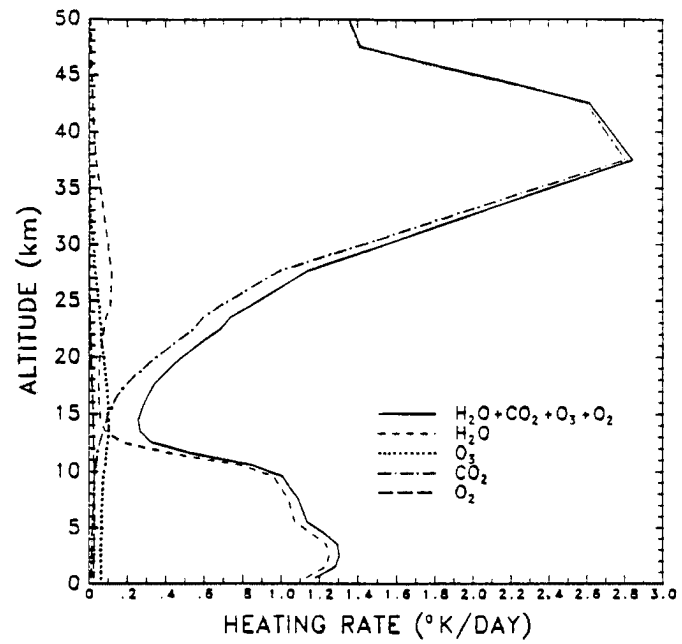

Figure 3.11: SW radiative heating rates ($°K/day$) in mid-latitude summer atmosphere for H_2O, CO_2,and O_3 and their combined effect.

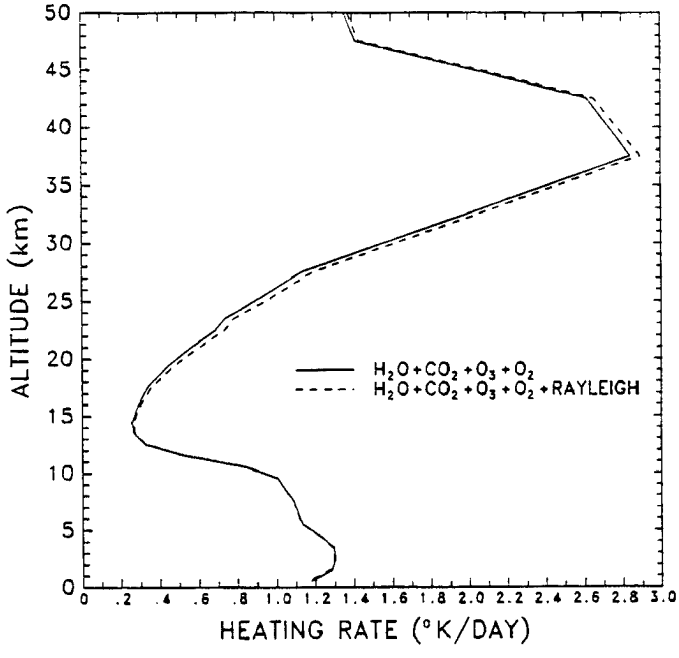

Figure 3.12: SW radiative heating rates ($°K/day$) in mid-latitude summer atmosphere for the combined effect of H_2O, CO_2, O_2 and O_3 and Rayleigh scatter.

Chapter 4

PARTICLE EXTINCTION AND CIRRUS CLOUDS

The complete formulation of the two-stream radiative transfer model including implementation of gaseous absorption and treatment of various numerical instabilities have been presented in detail in the preceeding chapters. Clear sky simulations in the long- and short wavelengths compared favorably to line-by-line radiative transfer methods in literature. Since the examination of cirrus clouds is the primary focus of this research, a method of calculating the optical depth, single scatter albedo and asymmetry parameter,- representative of cirrus cloud layers must be employed. The calculation of these parameters involves the use of Mie theory which requires the determination of the shape and size distributions of the particles.

The size distributions which are presented in this chapter were measured in the cirrus FIRE IFO on October 28, 1986. Comparison of the two stream and n-stream model is presented for a particular case in the solar wavelengths. Theoretical simulations of cirrus clouds are performed for different atmospheres and for various ice water content profiles in both the infrared and solar spectra.

The remaining modeling studies in this chapter focus on the effects of small particles on the radiative characteristics of cirrus clouds. The observational studies by Paltridge and Platt (1981) and Foote (1988) report significant concentrations of ice crystals smaller than 100 μm. During the FIRE experiment, the uncertainty in the measurements of particles of this size is unknown (see Heymsfield and Miller, 1989).

This study endeavors to show some of the radiative characteristics of cirrus cloudiness imbedded in various atmospheres and to evaluate the radiative effects of small particles in cirrus size distributions. These characteristics aid in the interpretation of the results

of the comparison between model simulations and aircraft observations performed in the following chapter.

4.1 Mie Theory

The optical depth, single scatter albedo and asymmetry parameter due to cloud particles are determined using Mie theory. Mie theory requires the size distributions of the cloud particles and their respective real and imaginary indices of refraction. For this study, the size distributions measured during the cirrus IFO are employed and these are discussed further below. The ice particles are assumed to be spheres and Mie's solutions are employed. The assumption of spherical cirrus ice particles is discussed in several studies (eg. Pollack and McKay, 1985; Ackerman et al.,1988 for review). Only recently have methods been developed which enable the treatment of irregularly shaped particles other than cylindrical crystals or spheroids. However since the object of this study is to evaluate the effects of the presence of small particles the effects of particle shape is left for future investigations.

In addition to the size distributions, the complex index refraction of ice must also be specified. This parameter is interpolated from tabulated values in the subroutine REFICE which is available through the public domain software at NCAR. In addition to the Mie theory solution a large particle approximation is also included which is required because of the large particles and the short solar wavelengths over which the integration is performed. The Mie solutions provide the volume extinction in (expressed in this study in km^{-1}) for a given spectral interval which can be used in (2.37) to find optical depth. The theory also gives the single scattering albedo, asymmetry parameter and the scattering phase function which are used directly in the radiative transfer model.

4.2 Stratus Cloud Simulation Test Case

A simulation of cloudy sky solar radiative transfer is presented here to establish the validity of the two-stream radiative transfer model under these conditions. The simulations are compared with the results from an n- stream radiative transfer described by

Stamnes et al. (1985) applied to the case presented in the dissertation by Tsay (1985). Since the n-stream radiative transfer model treats gaseous absorption with the sum of exponentials method, the present model was modified to accept these data as input. For the comparison presented below, the solar spectrum is divided into 24 bands. Figure 4.1 shows the atmospheric temperature and water vapor sounding used for this simulation. The sounding consisted of 53 levels with high vertical resolution throughout the troposphere. Two clouds, with a haze layer between, constitute the cloud layer which has cloud top and cloud base at approximately 1.2 km and 0.2 km respectively. The microphysical parameters of the cloud and haze layers were common to both models and the Henyey-Greenstein function was used to approximate the angular distribution function. The broadband optical depths of the cloud system are given in Table 4.1. Note that the top cloud accounts for nearly all the optical depth in the cloud system. Two other interesting features of this case study are the high sun angle (53.8°) and the high surface albedo (0.680 in the visible solar wavelengths and 0.350 in the near infrared).

Table 4.1: Optical depths of simulated stratus layers.

	Top Cloud	Haze Layers	Bottom Cloud	Total
Optical Depth (τ)	24.69	0.05	0.20	24.94

Figure 4.2 compares the heating rates ($°K/day$) of the top stratus cloud between the four-stream and the present two-stream models. The backscatter coefficients used in the two-stream results are listed in Table 4.2. The two stream model underestimated the heating at cloud top by an amount ranging from 3-7 $°K/day$ depending upon the backscatter approximation employed. Below cloud top agreement improves towards cloud base where discrepancies are less than 0.1 $°K/day$. The hemispheric mean approximation produced heating which agreed most closely to the four stream results especially towards cloud top (see Figure 4.2). Figures 4.3 and 4.4 respectively show the near infrared and visible spectral variation of the differential net flux (net flux top - net flux bottom) for the four-stream and the two-stream results. The most pronounced disagreement occurs in the visible spectrum (0.3-0.7μm) where absorption by particles is small ($\omega_0 \approx 1$). Thus

although relative errors appear large ($\approx$ 1 order of magnitude at worst), they contribute negligibly to the computation of heating rates when compared to the near infrared region (0.7-4.0μm) which exhibits much smaller relative error generally less than 5% with a few exceptions of $\approx$ 10% approaching the visible spectrum.

Table 4.2: Diffuse backscattering coefficients and their corresponding diffusivities (King and Harshvardan,1986).

Coefficient Name	Coefficient (b)	Diffusivity (D)
Hemispheric Mean	$\omega_0(1-g)$	2
Eddington Approximation	$-\frac{1}{4}[1-\omega_0(4-3g)]$	2
Discrete Ordinate	$\frac{\sqrt{3}}{2}\omega_0(1-g)$	$\sqrt{3}$
Coakley-Chylek	$\frac{\omega_0\beta_0}{\mu_0}$	$\frac{1}{\mu_0}$
Meador and Weaver Hybrid	$\frac{-1+g^2+\omega_0(4-3g)+\omega_0^2(4\beta_0+3g-4)}{4[1-g^2(1-\mu_0)]}$	$\frac{2-g^2}{[1-g^2(1-\mu_0)]}$

Table 4.3 compares the calculated fluxes at top and bottom of the atmosphere, the net fluxes at the surface, and the differential net fluxes for the atmosphere and the top cloud between the four-stream and two stream models. The two stream results generally agree well with the four stream results in that discrepancies never exceed 10% and only once show an absolute error over 10 $W \cdot m^{-2}$. Specific comparisons of $F^+(0)$ and $F^-(\tau^*)$ between the two stream backscatter approximations reveal fluxes which are both greater than and less than the corresponding four stream values. For instance, the discrete ordinate produces fluxes too large at the top of the atmosphere and too small at the surface while the Meador and Weaver hybrid approximation performs oppositely. Similar cases are found for the differential net flux in the atmosphere and the clouds. These results highlight the sensitivity of diffuse backscattering coefficients in the two stream model. The important point here is that the results of the two stream models bracket the results of the more complicated four stream in such a way that errors are generally less than 5%. The exception to this is the hemispheric mean approximation. However, although this approximation leads to more significant errors in scattering (ie. transmission is 20.8 $W \cdot m^{-2}$ too high, while reflection is 7.81 $W \cdot m^{-2}$ too low), the absorption within atmosphere and within the cloud most closely agree with the four stream results and in fact

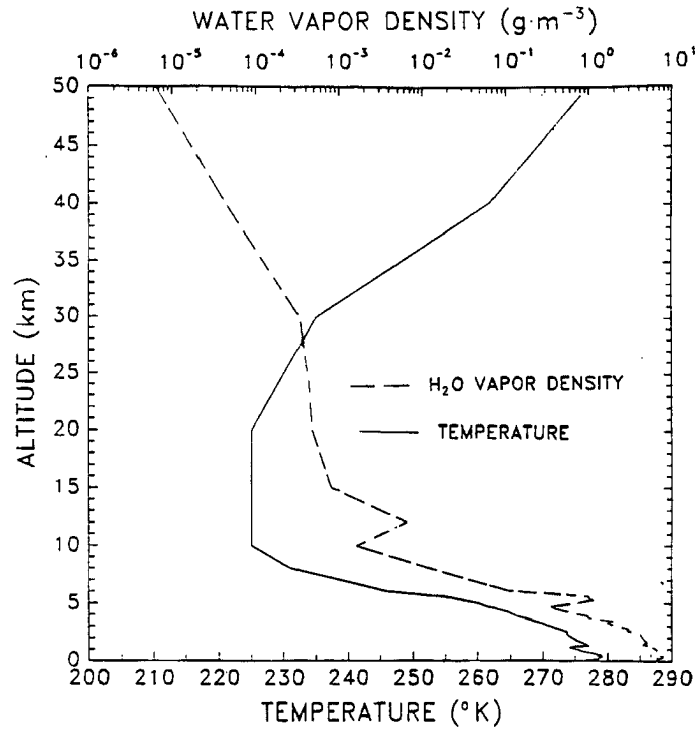

Figure 4.1: The atmospheric temperature and water vapor sounding for the status cloud atmosphere.

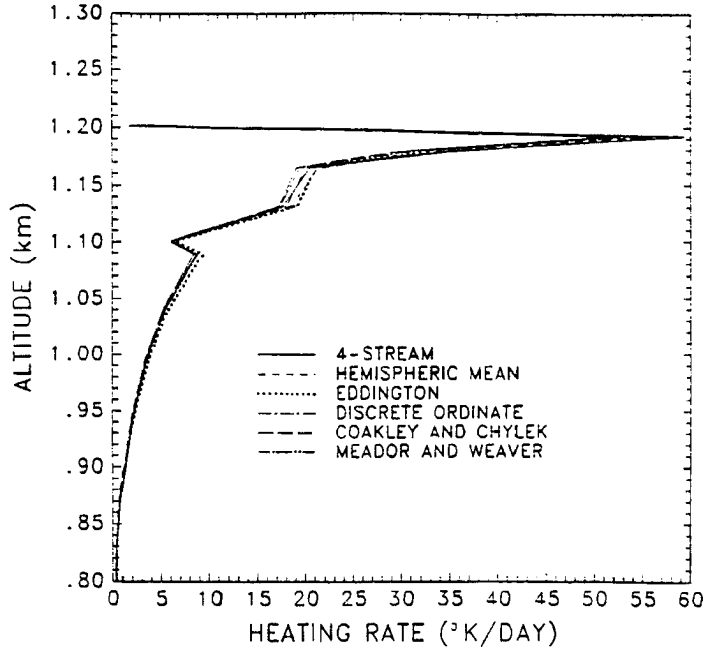

Figure 4.2: Stratus heating rates comparing the four stream and the present two stream model results for the various backscatter approximations shown in table 4.2

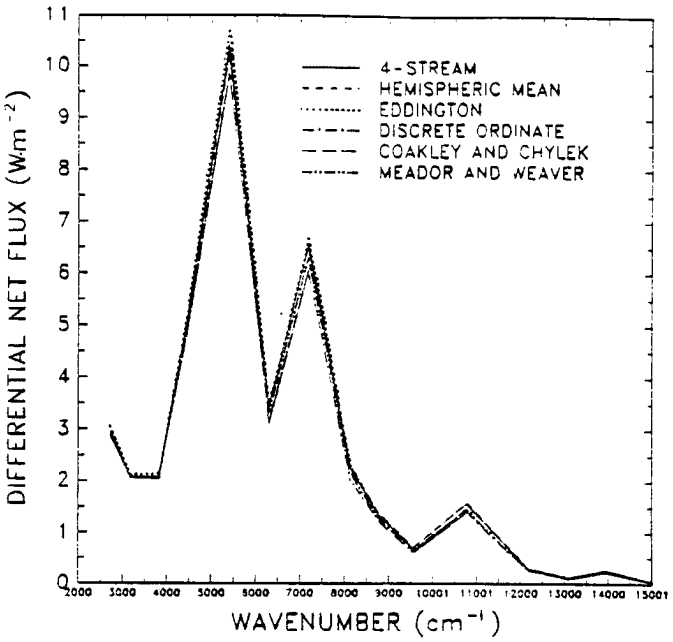

Figure 4.3: Comparison of the near infrared spectral differential net fluxes between the four stream and the present two stream results for the various backscatter approximations shown in table 4.2

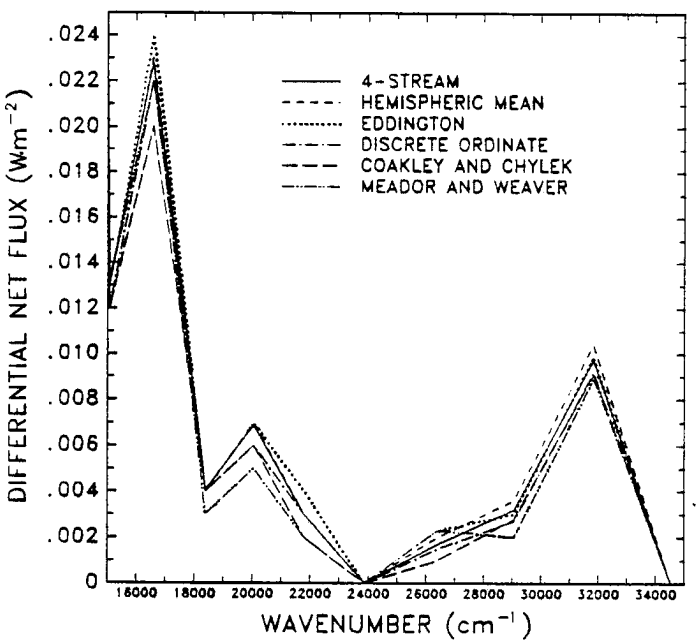

Figure 4.4: Comparison of the visible spectral differential net fluxes between the four stream and the present two stream results for the various backscatter approximations shown in table 4.2

this approximation produces the heating profile closest to that from the four stream model as noted above.

Table 4.3: Flux ($W \cdot m^{-2}$), net flux and differential net flux comparison between the four stream and the present two stream models for the various two stream backscatter approximations shown in Table 4.2. Infrared fluxes are in parentheses and the notation of Tables 3.4 - 3.6 is used here. Errors are computed only for total. $F^{-}(0) = 789.76(360.2)W \cdot m^{-2}$.

Model	$F^{+}(0)$	$F^{-}(\tau^{*})$	$F_{net}(\tau^{*})$	ΔF_{ATM}	ΔF_{cld1}
Four stream	518.91	247.43	98.00	172.85	39.22
	(187.47)	(57.04)	(37.08)	(135.65)	(38.78)
Two streams					
Hemispheric Mean	526.72	226.63	88.67	174.37	38.98
	(192.37)	(48.93)	(31.80)	(136.03)	(38.54)
Abs. error	-7.81	20.80	9.33	-1.52	0.24
Rel. error (%)	1.50	8.41	9.52	0.88	0.61
Eddington Approx.	512.55	257.16	102.12	175.09	40.26
	(184.11)	(60.10)	(39.06)	(137.03)	(39.81)
Abs. error	6.36	-9.73	-4.12	-2.24	-1.04
Rel. error (%)	1.22	3.93	4.20	1.30	2.66
Discrete Ordinate	523.93	243.50	96.36	169.47	36.83
	(191.08)	(55.59)	(36.13)	(132.99)	(36.45)
Abs. error	-5.02	3.93	1.64	3.38	2.39
Rel. error (%)	0.97	1.59	1.67	1.96	6.09
Coakley and Chylek	519.00	256.78	101.81	168.95	36.74
	(188.76)	(59.52)	(38.69)	(132.75)	(36.35)
Abs. error	-0.09	-9.35	-3.81	-3.90	2.48
Rel. error (%)	0.02	3.78	3.89	2.26	6.75
Meador and Weaver Hybrid	515.26	255.09	101.28	170.22	38.29
	(186.22)	(59.57)	(38.71)	(135.27)	(37.89)
Abs. error	3.65	-7.66	-3.28	2.63	0.93
Rel. error (%)	0.70	3.10	3.35	1.52	2.37

4.3 An Investigation of Cirrus Clouds In Various Atmospheres

Heating rate profiles in cirrus clouds are shown to be dependent upon the altitude of the atmosphere in which they occur (eg. Stephens, 1980) and the present model is now used to examine these dependencies. For this theoretical investigation a uniform cirrus cloud approximately 3 km thick is modeled with ice water contents (IWCs) of 0.1, 0.02, 0.002 $g \cdot m^{-3}$ respectively. Mie solutions were obtained for a size distribution measured on 10/28/86 (see Figure 4.20 below) normalized to these IWCs. The clouds

are positioned with cloud top at the tropopause in the McClatchey subarctic winter and tropical atmospheres. A composite 1600 Z sounding constructed from the observed 1500 Z and 1730 Z Green Bay, Wisconsin soundings on 10/28/86 is used as a third atmosphere for comparison (see sec. 5.1.4). The position of the cloud layer in this atmosphere is located according to observed positions of the cirrus clouds. All the simulations assume saturation with respect to ice throughout the cloud layer.

For the longer wavelengths, Stephens (1980) shows that the temperature difference between the ground (or underlying cloud top) and the cirrus cloud base (ΔT_{gc}) largely determines the heating profile within the cloud. Figures 4.5-4.7 show heating rates in the infrared for the three atmospheres mentioned above. The heating profiles show an enhancement of cloud top cooling and cloud base heating with increasing IWC. The very thin cirrus clouds exhibited virtually uniform heating in the Wisconsin and Tropical atmospheres and cooling in the Subarctic winter atmosphere compared to the clear sky. Comparison of these figures also reveals an increase in heating at cloud base and cooling at cloud top with increasing altitude.

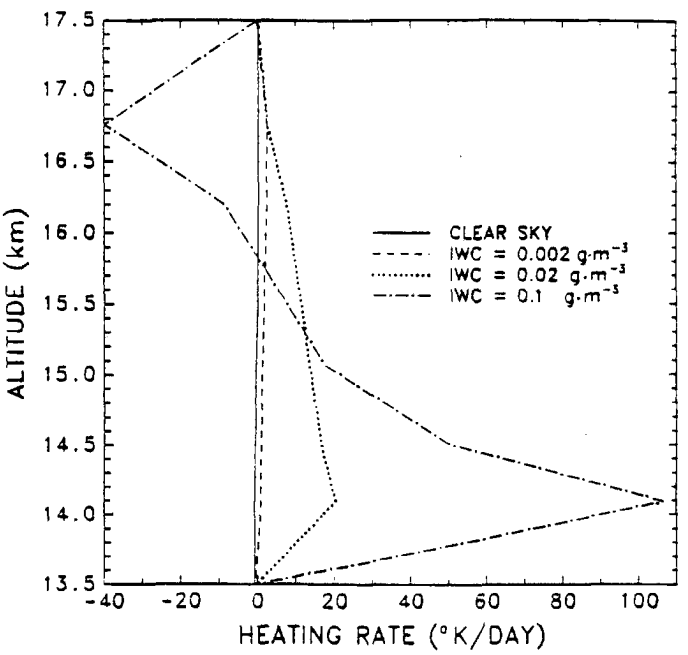

Figure 4.5: Radiative heating rates in the infrared for a 3 km uniform cirrus cloud with ice water contents of 0.002, 0.02 and 0.1 $g \cdot m^{-3}$ in a tropical atmosphere.

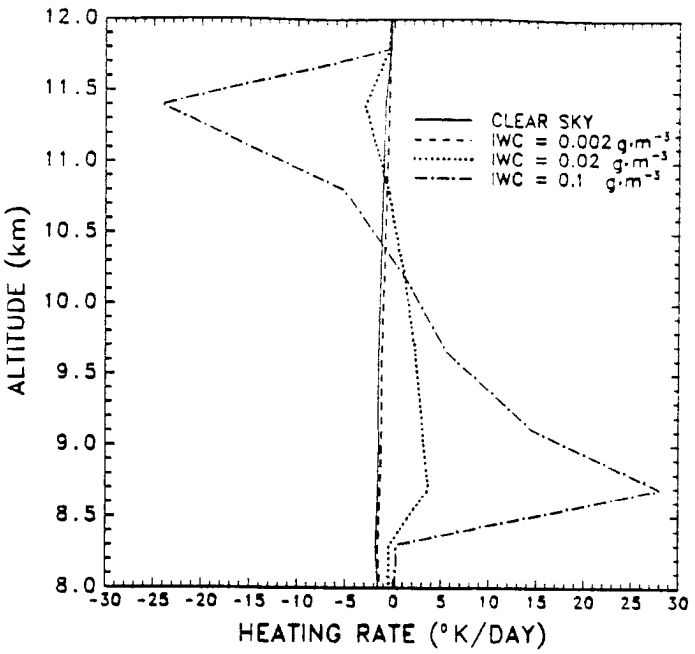

Figure 4.6: Radiative heating rates in the infrared for a 3 *km* uniform cirrus cloud with ice water contents of 0.002, 0.02 and 0.1 $g \cdot m^{-3}$ in FIRE October 28, 1986 Wisconsin atmosphere.

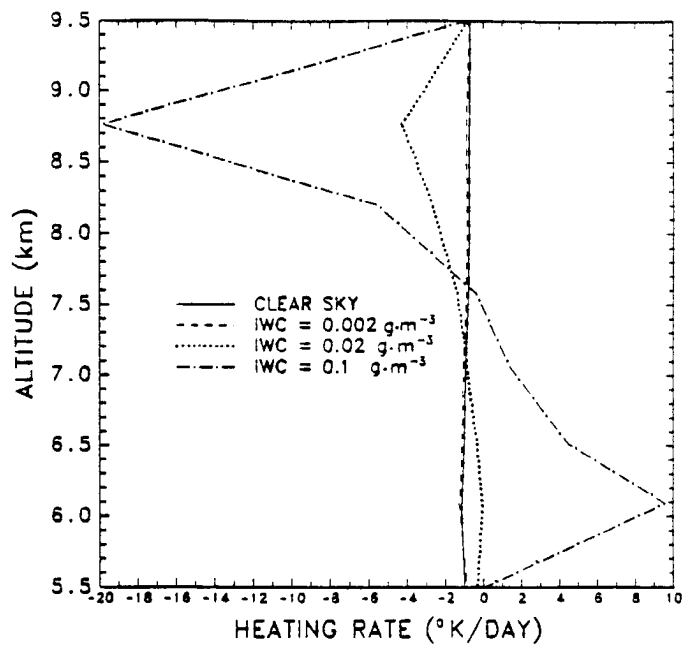

Figure 4.7: Radiative heating rates in the infrared for a 3 *km* uniform cirrus cloud with ice water contents of 0.002, 0.02 and 0.1 $g \cdot m^{-3}$ in a subarctic winter atmosphere.

Table 4.4 summarizes this result for the dense cloud with IWC = 0.1 $g \cdot m^{-3}$. The relative areas in Figures 4.5-4.7 of heating at cloud base and cooling at cloud top determine the overall radiative effect of the cloud layer on the environment. Therefore, cooling processes dominate at the cloud top in the subarctic cirrus while the heating processes dominate at cloud base in the tropical and Wisconsin cirrus. Figure 4.8 is a schematic of the net energy budget derived for the cloud layer obtained as the difference of the net fluxes at cloud top and base (see sec. 2.5.3). This figure along with Table 4.4 show that the net effect of the cirrus is one of cooling at the lowest altitude and least ΔT_{gc}. The cooling changes to warming which in turn increases as both ΔT_{gc} and altitude increase. Also shown is the sensitivity of the differential net flux to change in IWC and this sensitivity increases with increasing height. These results imply that there may exist a cloud where the cloud top cooling balances the cloud base heating so that the differential net flux is essentially zero and is insensitive to changes in IWC. The net radiative effect of a cirrus cloud in the infrared is then determined by its height (or ΔT_{gc}) above or below this equilibrium cloud and the heating (cooling) becomes larger with increasing (decreasing) height (and or ΔT_{gc}).

Table 4.4: Cloud top and base radiative heating rates ($\frac{dT_t}{dt}, \frac{dT_b}{dt}$) as a function of cloud base height and temperature difference (ΔT_{gc}) between cloud base (T_b) and the surface (T_g) for a 3 km uniform cirrus with IWC = 0.1 $g \cdot m^{-3}$ in the Tropical, Wisconsin and Subarctic Winter atmospheres.

Atmosphere	Alt (km)	T_b (^oK)	T_g (^oK)	ΔT_{gc} (^oK)	$\frac{dT_b}{dt}$ ($^oK/day$)	$\frac{dT_t}{dt}$ ($^oK/day$)
Tropical	14.0	210.0	300.0	90.0	106.6	-39.9
Wisconsin	8.6	234.4	286.7	52.3	28.0	-24.2
Subarctic Winter	6.0	234.1	257.1	23.0	9.6	-19.9

Comparison of the spectral differential net fluxes for tropical cirrus (shown in Fig. 4.9) and subarctic winter atmospheres (shown in Fig. 4.10) reveals that heating dominates in the atmospheric window region ($8\mu m$-$12\mu m$) and cooling dominates in the far infrared ($\approx 15\mu m - 200\mu m$). This is always true due to the influence of the H_2O absorption bands in the far infrared region. In the tropical atmosphere the heating in the window

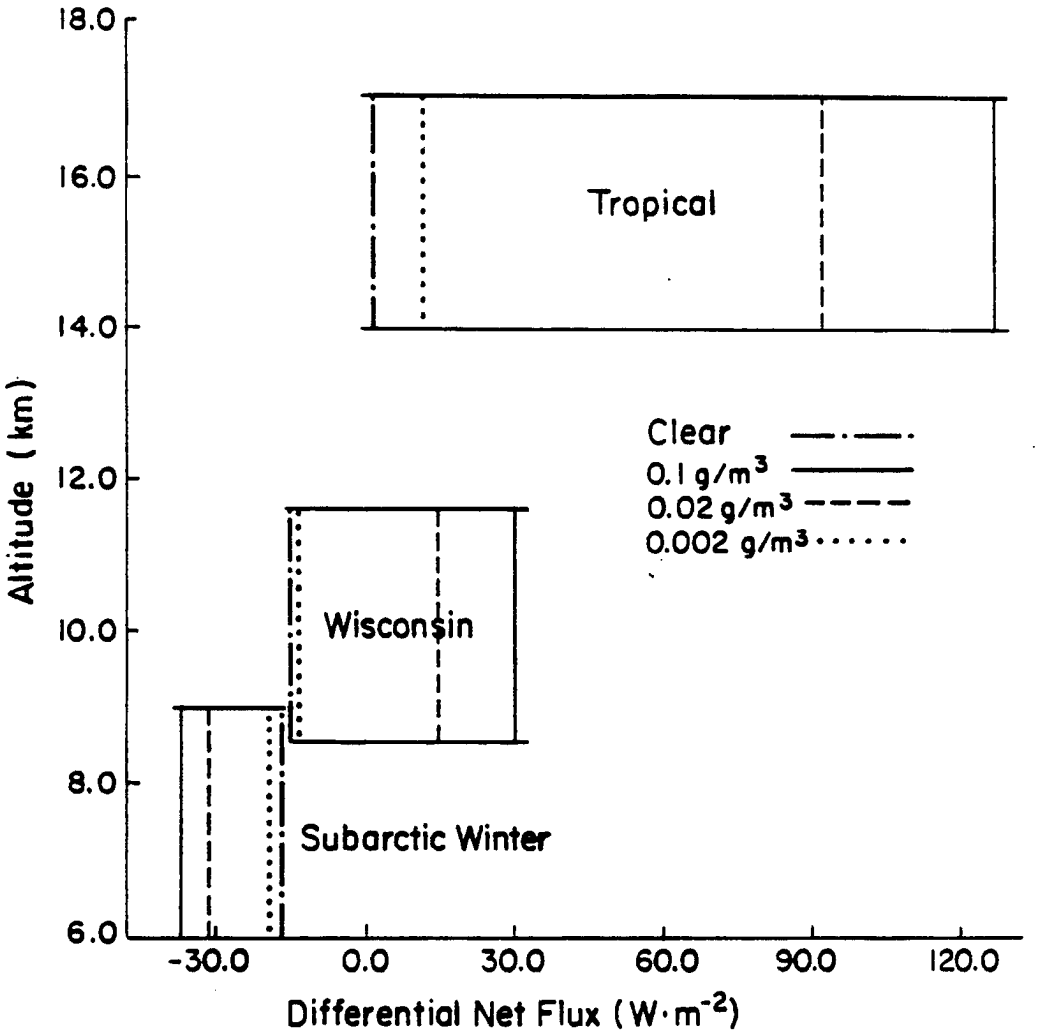

Figure 4.8: Schematic of the net infrared energy budgets of the three 3 km uniform cirrus clouds situated in their respective atmospheres as shown for ice water contents of 0.002, 0.02 and 0.1 $g \cdot m^{-3}$.

region is much greater than the cooling in the far infrared despite the fact that significant window absorption occurs in the moist tropical atmosphere below the cloud. The reverse holds for the subarctic winter atmosphere. The relationship between the window heating and far infrared cooling depends on the microphysics of the cloud and the environmental conditions in which the cloud exists.

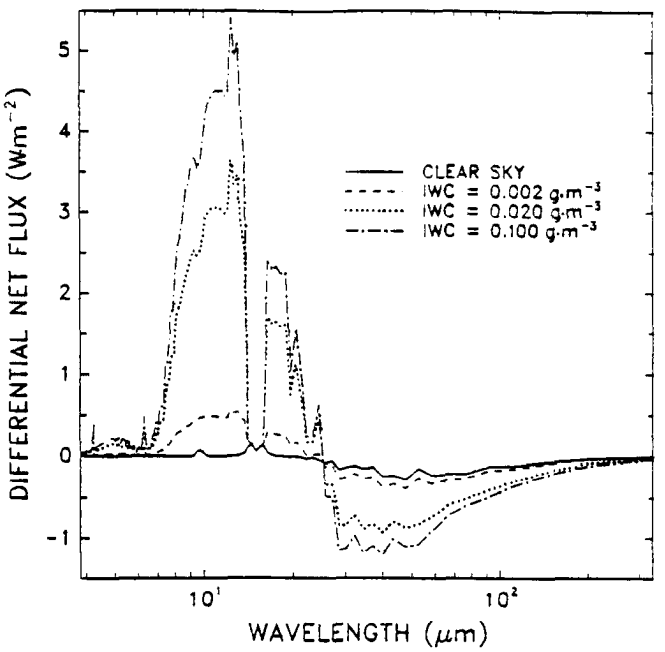

Figure 4.9: Spectral net differential fluxes in the infrared wavelengths for a 3 km uniform cirrus cloud with ice water contents of 0.002, 0.02 and 0.1 $g{\cdot}m^{-3}$ in a Tropical atmosphere.

Calculations of the solar transfer were for a zenith angle of 61.4° and a surface albedo 0.072 which happen to correspond to the estimated albedo over Lake Michigan at 10:00am local time. Figures 4.11-4.13 show that the heating at cloud top due to the incident solar radiation dominates producing a net radiative heating as a result. However, the solar heating at cloud top for the most dense tropical cirrus cloud is greater than the most dense subarctic cirrus cloud by approximately $15°K/day$ despite the fact that the same solar flux and zenith angles were used. The lower altitude of the subarctic winter cirrus cloud ($\approx$ 8 km) allows for scattering and absorption processes to decrease the incident solar radiation at cloud top thus decreases the flux convergence and heating. Comparison of the spectral absorption for the tropical (Fig. 4.14) and subarctic winter (Fig. 4.15) atmospheres

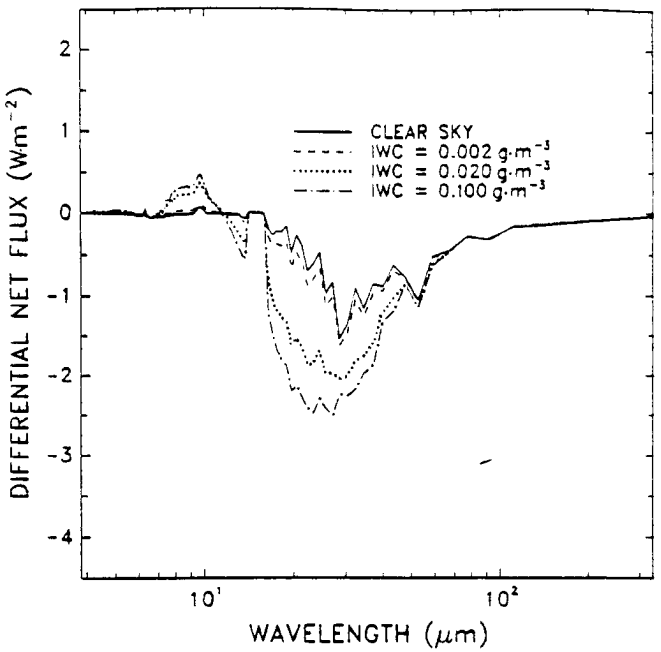

Figure 4.10: Spectral net differential fluxes in the infrared wavelengths for a 3 km uniform cirrus cloud with ice water contents of 0.002, 0.02 and 0.1 $g \cdot m^{-3}$ in a Subarctic winter atmosphere.

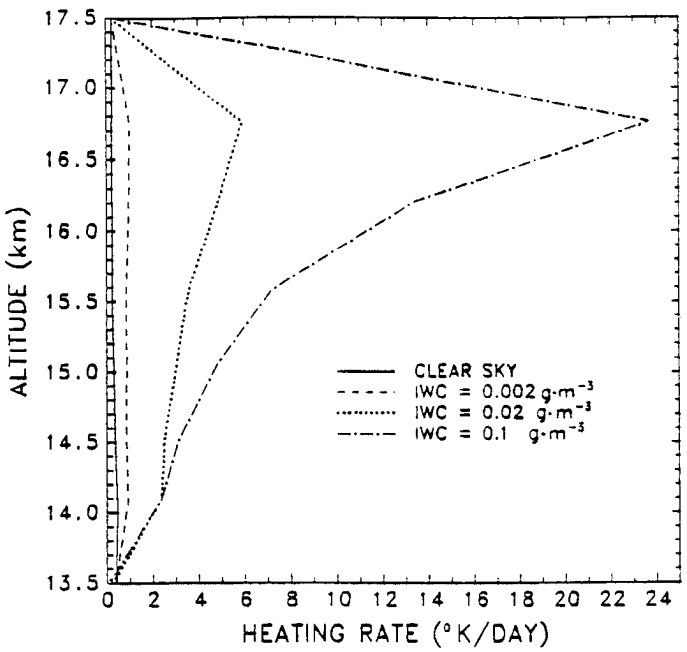

Figure 4.11: Radiative heating rates in the solar wavelengths for a 3 km uniform cirrus cloud with ice water contents of 0.002, 0.02 and 0.1 $g \cdot m^{-3}$ in a tropical atmosphere.

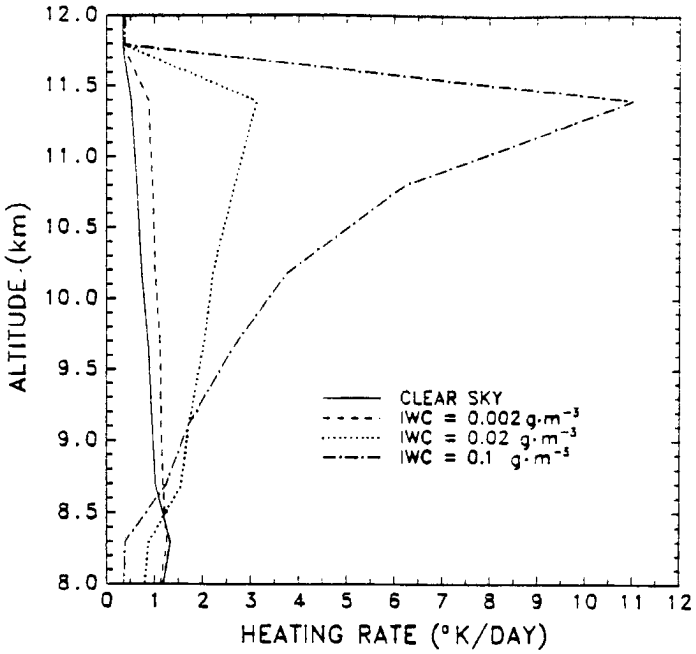

Figure 4.12: Radiative heating rates in the solar wavelengths for a 3 km uniform cirrus cloud with ice water contents of 0.002, 0.02 and 0.1 $g \cdot m^{-3}$ in FIRE October 28, 1986 Wisconsin atmosphere.

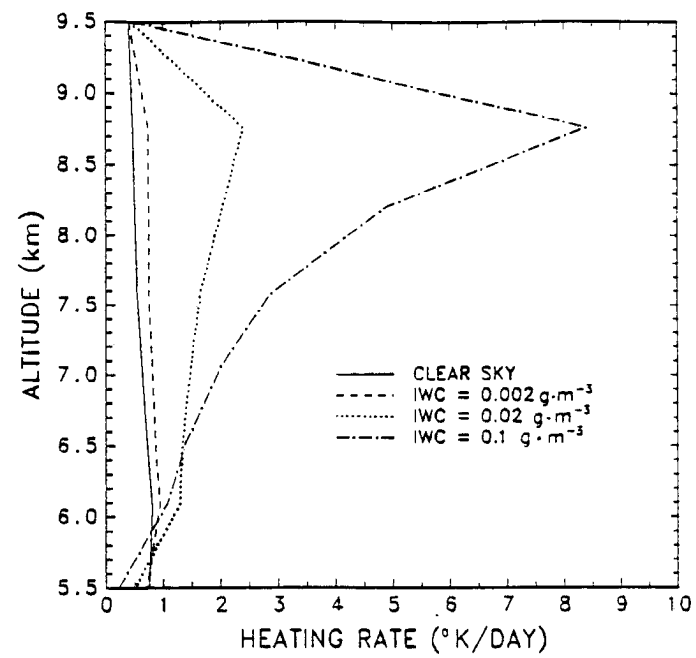

Figure 4.13: Radiative heating rates in the solar wavelengths for a 3 km uniform cirrus cloud with ice water contents of 0.002, 0.02 and 0.1 $g \cdot m^{-3}$ in a Subarctic winter atmosphere.

reveal very similar results despite the differences in the respective atmospheres. The clear sky differences are attributed mainly to the higher water vapor amounts in the subarctic winter cloud because of the higher temperatures at the cloud altitudes. The differences in the cloud absorption in the $2.6 - 2.9\mu m$ spectral region account for a large part of the differences in heating between the clouds of these two atmospheres. The CO_2 band corresponding to this spectral region is saturated in the subarctic atmosphere because of the longer path lengths to cloud top encountered by the radiation compared to those of the tropical atmosphere.

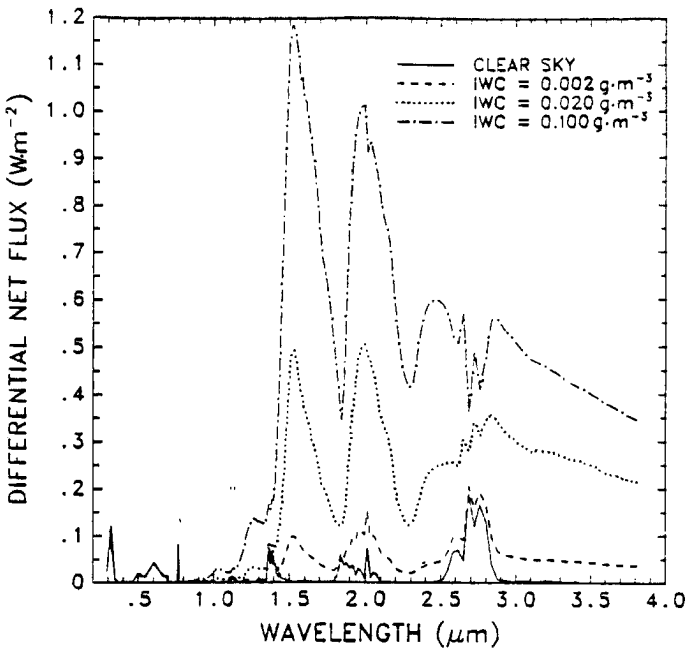

Figure 4.14: Spectral net differential fluxes in the solar wavelengths for a 3 km uniform cirrus cloud with ice water contents of 0.002, 0.02 and 0.1 $g \cdot m^{-3}$ in a tropical atmosphere.

The heating rate profiles of cirrus clouds in various environments as presented in this section are very similar to theoretical studies presented by Ackerman et. al. (1988). In addition, the results of the above investigation have profound climatological implications (eg. Stephens (1980), Stephens and Webster (1981) and Platt and Harshvardhan (1988)). It is not enough just to know the amount of cirrus or the distribution of cirrus about the globe to understand their influence on the earth radiation budget. In order to understand the climatological effects of cirrus clouds information regarding temperature and height as well as their distribution and microphysical characteristics must also be understood.

4.4 The Effect of Small Particles in Cirrus Clouds During FIRE

A theoretical study of cirrus clouds is now presented with the objective of investigating the likely effects of small particles on the radiometric properties of these clouds. An effort is made to replicate the environmental conditions and the microphysical characteristics of the cirrus present during the FIRE IFO case of October 28, 1986. This study is used to make inferences regarding the effect of small particles on the observed radiometric fields measured in the cirrus clouds during that case. Before presenting these studies in detail, the method of treatment for small particles is now described.

4.4.1 Inclusion of Small Particles in the Size Distributions

Figure 4.16 shows the ice water content (IWC) as a function of altitude for the October 28 case (Heymsfield, personal communication). For this case the upper level observations of IWC closely corresponds to cloud top and the lowest level of IWC to the cloud base. The observed particle concentrations from the 2C probe on board the aircraft are weighted to the IWC measurement assuming an appropriate particle density as follows:

$$IWC = 10^6 \frac{4\pi}{3} \rho_{ice} \int_0^\infty n_w(r)\, r^3\, dr \tag{4.1}$$

where IWC is the measured ice water content in $g \cdot m^{-3}$, ρ_{ice} is the density of the particles in $g \cdot cm^{-3}$, r is the particle radius in μm and $n_w(r)$ is the weighted size distribution of the particles having units $N \cdot cm^{-3} \cdot \mu m^{-1}$ given by

$$n_w(r) = n_m(r) \frac{IWC}{(IWC)_0} \tag{4.2}$$

where $n_m(r)$ is the measured size distribution and IWC_0 is the ice water content calculated using (4.1) for $n_m(r)$.

Since only particles greater than 50 μm in diameter were measured, particles smaller than this size were not sampled and thus were not accounted for in the IWC data shown by the solid lines of Figures 4.17-4.23. However, smaller particles were observed on impact slides and their existence has been speculated on previously. Thus the amount and size of smaller particles is taken into account by assuming a simple analytic size distribution

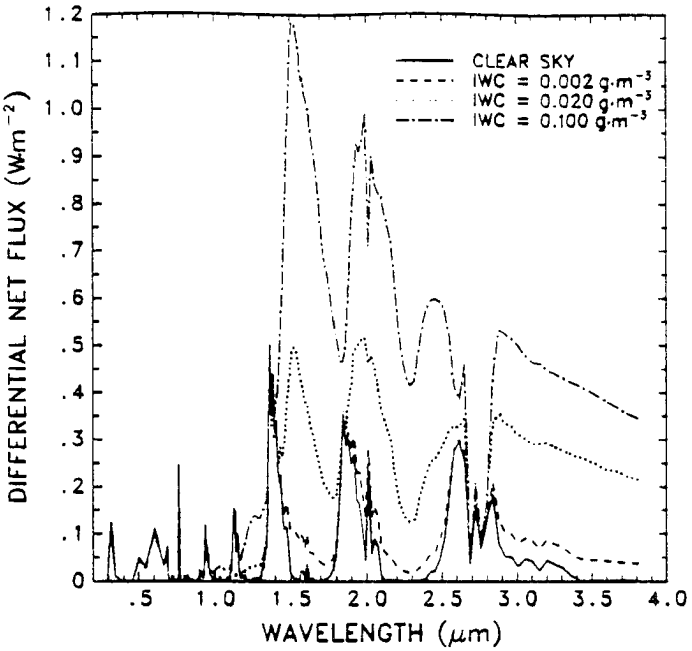

Figure 4.15: Spectral net differential fluxes in the solar wavelengths for a 3 km uniform cirrus cloud with ice water contents of 0.002, 0.02 and 0.1 $g \cdot m^{-3}$ in a Subarctic winter atmosphere.

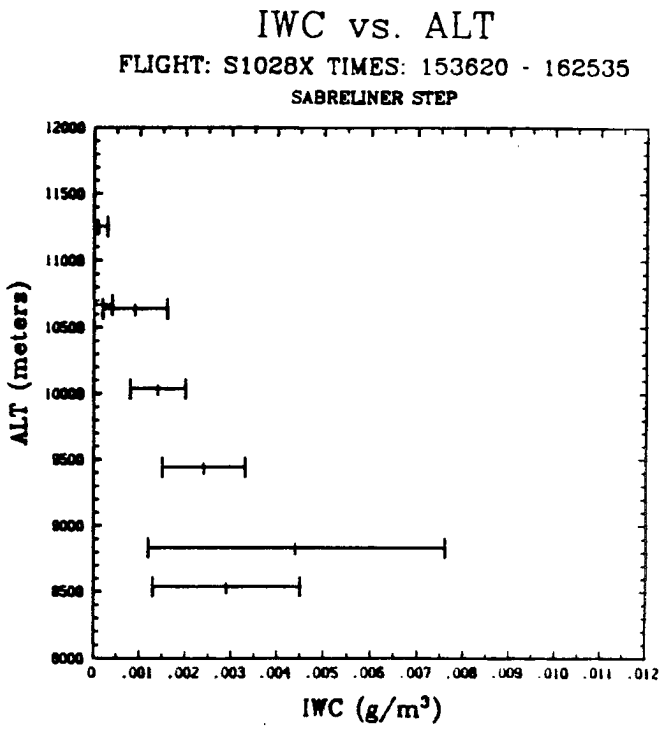

Figure 4.16: Measured ice water content and standard deviations as a function of altitude for each flight leg of Oct. 28, 1986 during FIRE. (Heymsfield, personal communication)

for particles from 10 - 50 μm in diameter. The form of the small particle size distribution $n_s(r)$ is by

$$n_s(r) = N_0\, r\, e^{-\frac{r}{b}} \tag{4.3}$$

where $N_0 = 1.25 \times 10^{-4} N \cdot cm^{-3} \cdot \mu m^{-2}$ and $b = 10\mu m$ is the modal radius. Since the measured IWC represents only large particles, the small particles to the ice water content which is prescribed in terms of the ratio a such that:

$$a \equiv \frac{(IWC)_m}{(IWC)_{tot}} \tag{4.4}$$

where the subscripts m and tot refer to the measured or large particles and all particles respectively. Since

$$(IWC)_{tot} = (IWC)_m + (IWC)_s,$$

where the subscript s refers to small particles, then

$$1 - a = \frac{(IWC)_m}{(IWC)_{tot}}$$

and therefore the small particle ice water content is given by

$$(IWC)_s = \frac{1-a}{a}(IWC)_m. \tag{4.5}$$

The small particle ice water content is prescribed in this way because it is assumed that the IWC values derived from the aircraft measurements represent $(IWC)_m$. The ratio a is expected to vary between 0.8 to 1.0 (Heymsfield and Miller, 1989) and therefore three different size distributions a=0.8, 0.9 and 1.0 are proposed. Figures 4.17-4.23 show the adjusted size distributions for $a = 0.8$ and 0.9 along with the measured size distributions ($a = 1$) at each altitude leg of the October 28, 1986 case.

4.4.2 Simulation Cases: enhanced IWC vs added small particles

The prescription of ice water content due to the addition of small particles to the cirrus size distribution as described in the previous section may influence the radiative characteristics of these clouds in two ways: first, by the enhancement of IWC and secondly by the decrease of the effective radius of the size distributions. The following simulations were

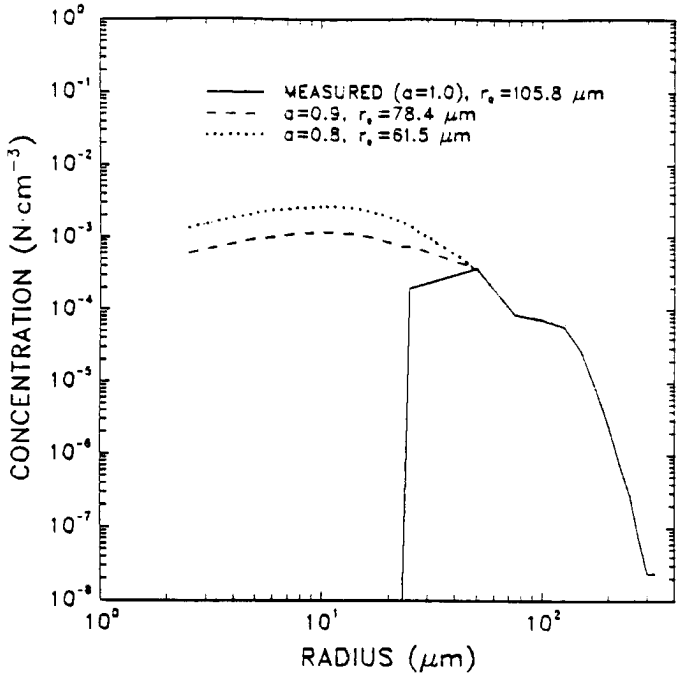

Figure 4.17: Cirrus ice crystal size distributions for $a = 1.0$, 0.9 and 0.8 measured during leg 1 at 10.641 *km* and 217.3 ^{o}K.

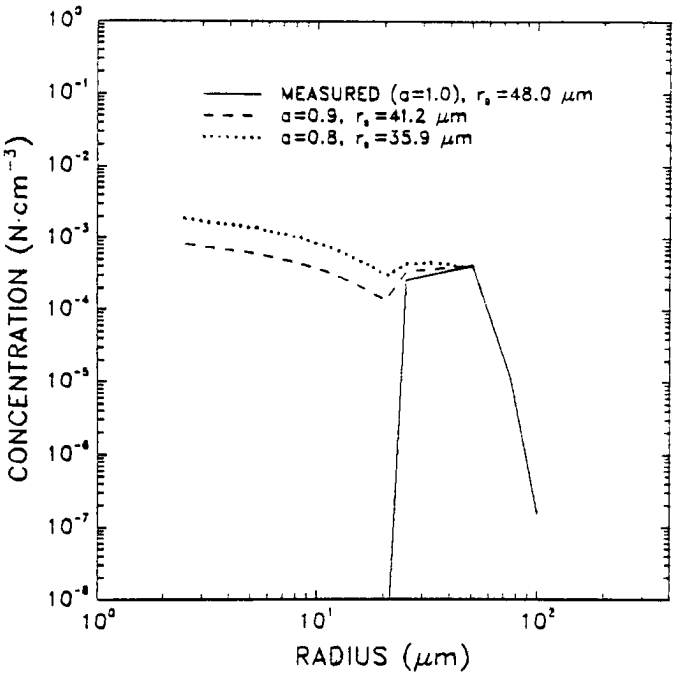

Figure 4.18: Cirrus ice crystal size distributions for $a = 1.0$, 0.9 and 0.8 measured during leg 2 at 11.259 *km* and 213.8 ^{o}K.

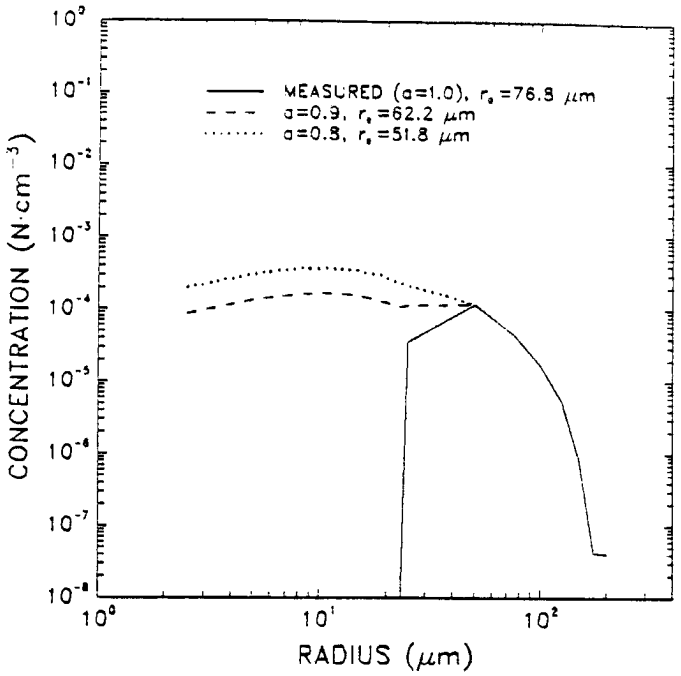

Figure 4.19: Cirrus ice crystal size distributions for $a = 1.0$, 0.9 and 0.8 measured during leg 3 at 10.667 *km* and 216.8 $°K$.

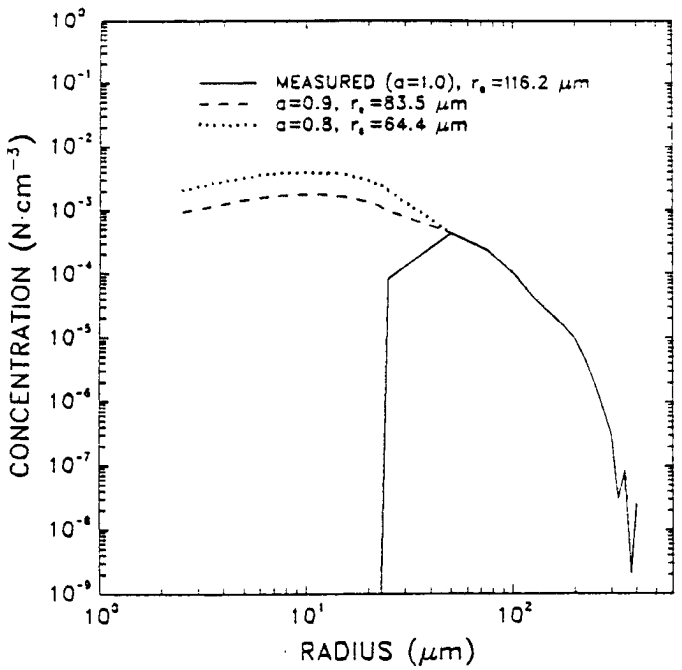

Figure 4.20: Cirrus ice crystal size distributions for $a = 1.0$, 0.9 and 0.8 measured during leg 4 at 10.038 *km* and 222.4 $°K$.

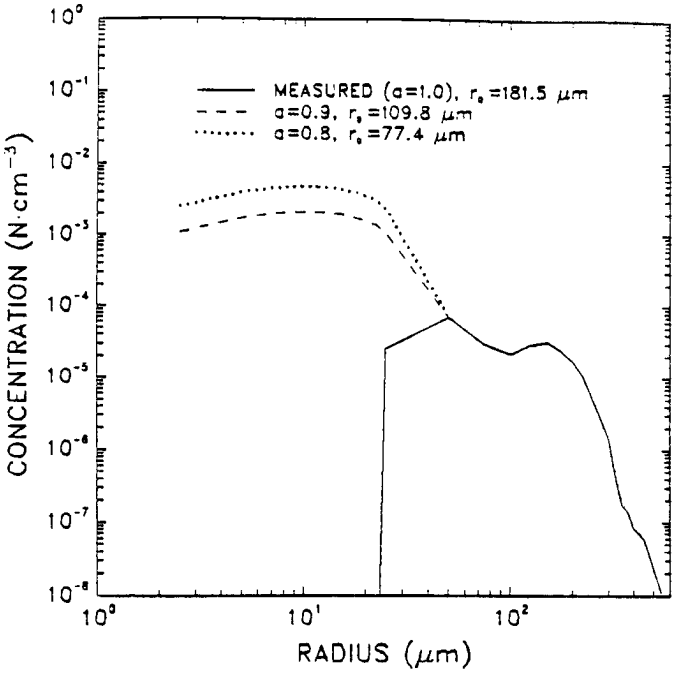

Figure 4.21: Cirrus ice crystal size distributions for $a = 1.0$, 0.9 and 0.8 measured during leg 5 at 9.445 *km* and 227.1 ^{o}K.

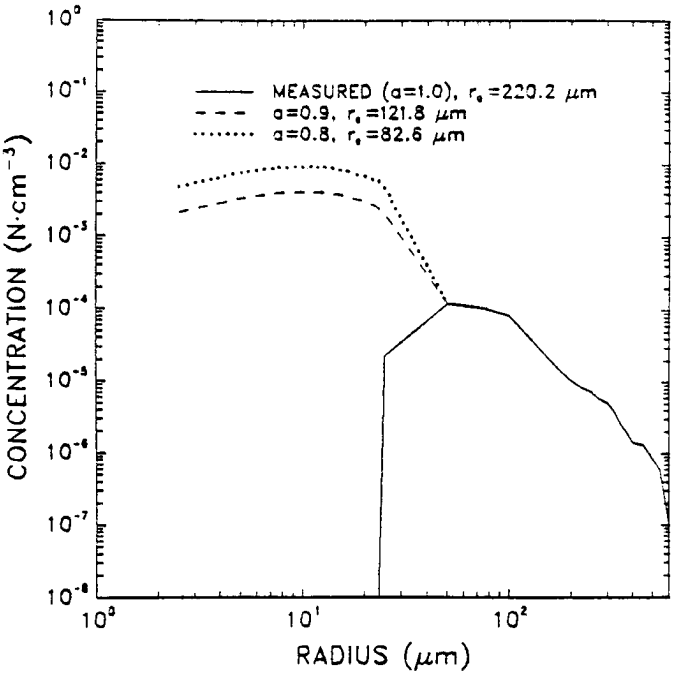

Figure 4.22: Cirrus ice crystal size distributions for $a = 1.0$, 0.9 and 0.8 measured during leg 6 at 8.834 *km* and 232.2 ^{o}K.

conducted to assess which of these influence the radiative characteristics of cirrus clouds most. Figure 4.24 presents the longwave radiative heating profiles for the hypothetical uniform cirrus cloud of section 4.3 in the Wisconsin atmosphere. The solid line is the clear-sky heating profile while the dashed line represents the radiative heating profile of the measured size distribution. The dotted line shows the radiative heating profile of the case when a=0.8. This case requires that 0.0005 $g \cdot m^{-3}$ be added to the measured ice water content so that $(IWC)_{tot}$ = 0.0025 $g \cdot m^{-3}$. The dot-dashed line represents the heating rate profile for the case where the measured size distribution was normalized to 0.0025 $g \cdot m^{-3}$ for comparison. This comparison shows that the change in heating due to the addition of small particles is approximately a factor of three greater than the change in heating caused by the enhancement of the IWC in the measured size distribution. Figure 4.25 presents the spectral net differential fluxes and shows that the effects from the addition of small particles on the absorption properties of this cirrus cloud are largest in the water vapor continuum region ($8\mu m$-$12\mu m$). Figure 4.26 compares the spectral upward cloud emittances (see sec. 5.2.1 for definition) for the identical cases described above. The enhancement of emittance due to decrease of the effective crystal size dominates greatly except in spectral regions where gaseous absorption bands have saturated.

Figure 4.27 presents the solar heating rate profiles for the hypothetical cases just described. The enhancement of the radiative heating profiles due to the addition of small particles is approximately a factor of two greater than the change in heating due to the enhanced IWC. Figure 4.28 shows the spectral differential net flux in the near infrared spectral region. The absorption of the cirrus cloud is greatly increased from the addition of small particles only for wavelengths greater than 2.8 μm. For shorter wavelengths, difference between the change due to the decrease of effective crystal size is only slightly greater than that of the renormalized measured size distribution. Thus the differences observed in the heating rates are due mainly to the effects of the smaller effective crystal size for wavelengths greater than 2.8 μm. The spectral albedo of the cirrus cloud in the near infrared is given by Figure 4.29 and in the visible region by Figure 4.30. These figures show the substantial effects of decreasing the effective crystal size which enhance the albedo of the cloud.

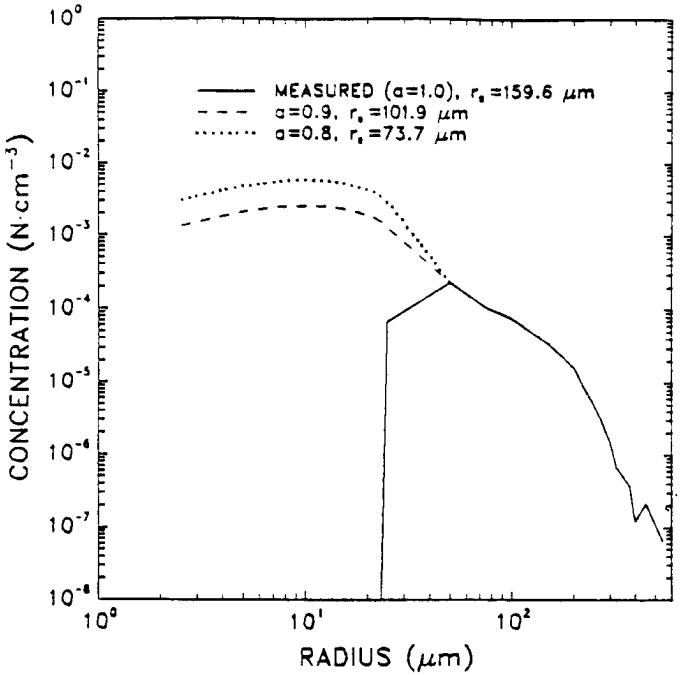

Figure 4.23: Cirrus ice crystal size distributions for a = 1.0, 0.9 and 0.8 measured during leg 7 at 8.537 *km* and 234.4 °*K*.

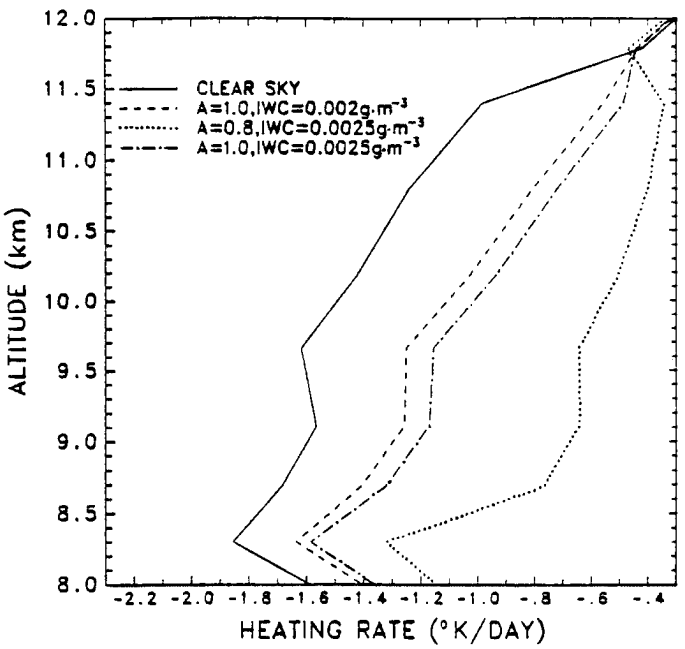

Figure 4.24: Infrared radiative heating rates for the cases described in the text for a 3 *km* uniform cirrus cloud in the Wisconsin atmosphere.

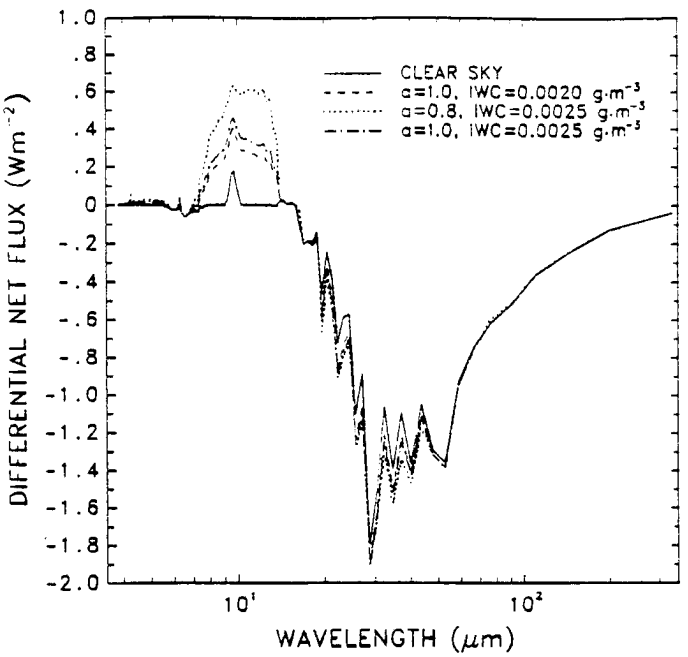

Figure 4.25: Spectral differential net fluxes in the infrared for the cases described in text for a 3 *km* uniform cirrus cloud in a Wisconsin atmosphere.

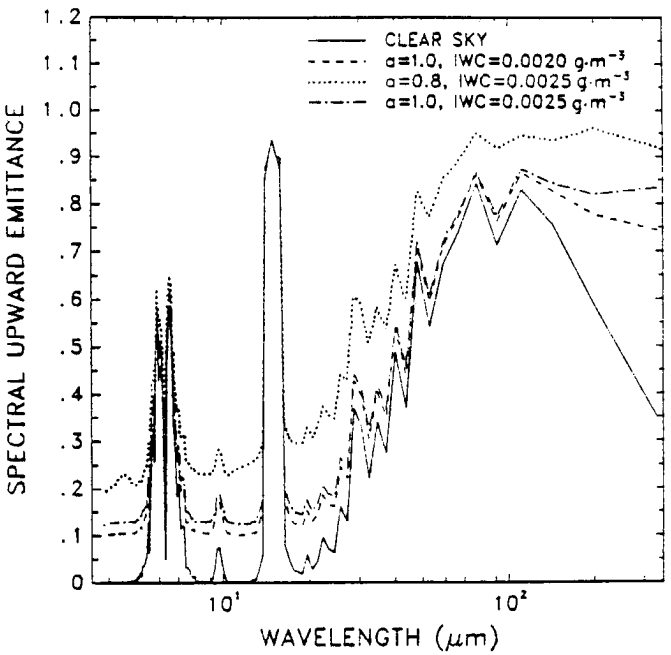

Figure 4.26: Spectral emittances in the infrared for the cases described in text for a 3 *km* uniform cirrus cloud in a Wisconsin atmosphere.

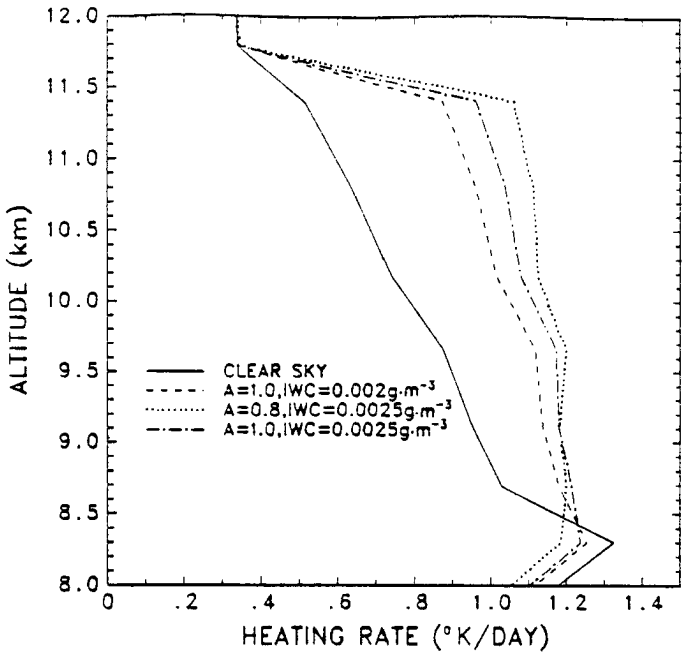

Figure 4.27: Solar radiative heating rates for the cases described in the text for a 3 *km* uniform cirrus cloud in the Wisconsin atmosphere.

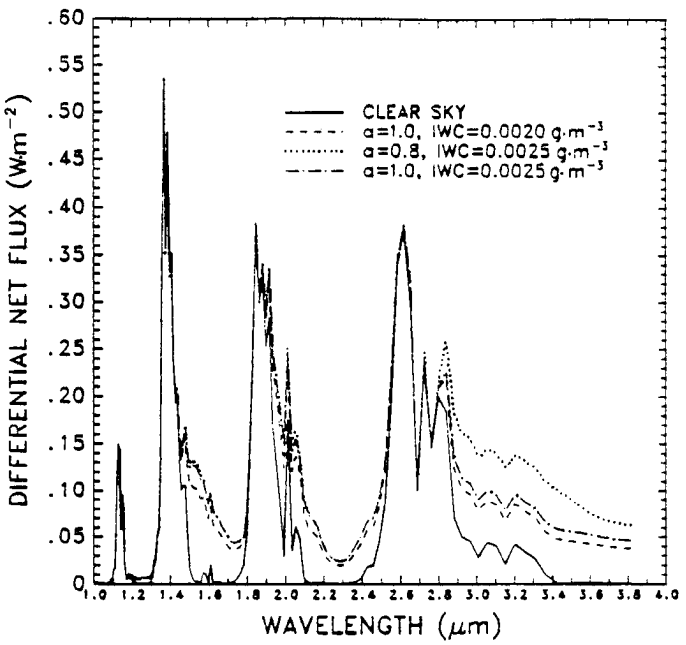

Figure 4.28: Spectral differential net fluxes in the near infrared solar wavelengths for the cases described in text for a 3 *km* uniform cirrus cloud in a Wisconsin atmosphere.

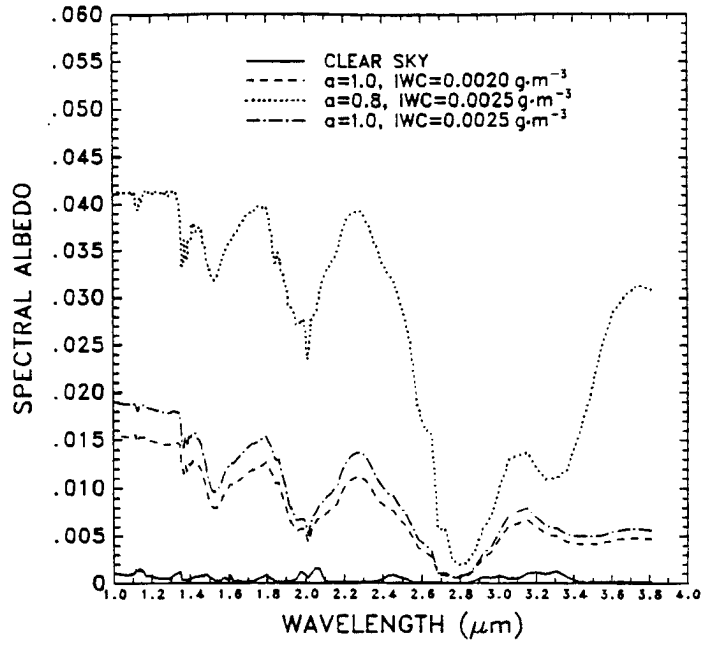

Figure 4.29: Spectral albedo in the near infrared ($1.0 - 4.0\mu m$) for the cases described in text for a 3 km uniform cirrus cloud in a Wisconsin atmosphere.

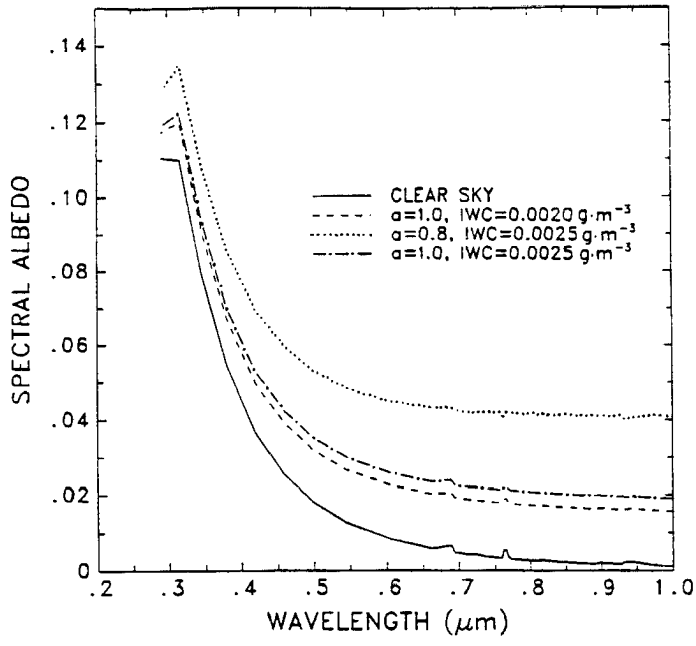

Figure 4.30: Spectral albedo in the visible wavelengths ($0.25\mu m - 1.0\ \mu m$) for the cases described in text for a 3 km uniform cirrus cloud in a Wisconsin atmosphere.

In principle, the effect of enhanced ice water content and decreased effective crystal size through the addition of small particles cannot be separated. However, these simulations show that for wavelengths greater than $2.8\mu m$ (including the infrared) the effect of the decreased effective crystal size in a size distribution on the radiative characteristics of a cirrus cloud is much greater than that of enhanced ice water content. Thus in this spectral region changes in the radiative characteristics of cirrus clouds caused by the prescription of the ratio a presented in the previous section are primarily caused by the decrease of the effective crystal size and not the corresponding IWC. Therefore appreciable differences between observations of cirrus radiative characteristics and theoretical calculations in the near infrared and infrared spectral regions may partly be attributable to uncertainties of the effective crystal size in the observed size distributions. However, discrepancies between observations and theoretical calculations in the visible spectrum may be more difficult to resolve.

4.4.3 Simulations Cases: The Effect of Small Particles on Variable IWC Profile Clouds

Up to this point only uniform cirrus clouds have been considered. It is advantageous to examine a cloud with variable ice water content similar to the clouds observed on 10/28/86 during FIRE in order to gain a better understanding of the characteristics of cirrus. Figure 4.16 presents the IWC profile used in these simulations in which a is varied from 1.0 to 0.8. The observed atmospheric sounding is used along with the size distributions in Figures 4.17-4.23. Table 4.5 shows the position of each size distribution observed in the cloud.

Table 4.5: Positions of Size Distributions Observed

Layer	Size Distribution	IWC ($g \cdot m^{-3}$)	T(^oK)	Alt (km)
1	Fig. 4.18	0.00019	213.8	11.42
2	Fig. 4.17	0.00129	217.3	10.80
3	Fig. 4.20	0.00200	222.4	10.20
4	Fig. 4.21	0.00242	227.1	9.60
5	Fig. 4.22	0.00471	232.2	8.99
6	Fig. 4.23	0.00292	234.4	8.70

Figures 4.31 and 4.32 show radiative heating rates inside the cloud for the infrared and solar wavelengths for three different values of a. The variable IWC profile has a noticeable

effect on the shape of the heating profile in both cases. The sharp discontinuities of heating and cooling at the top and base of the cirrus clouds seen in the uniform cloud cases are no longer evident. Instead heating gradually increases in both the solar and infrared wavelengths toward the thickest layer in the cloud. This occurs because of the shape of the IWC profile and the optical thinness of the cloud. In all cases the addition of small particles significantly enhances the radiative heating within the cloud.

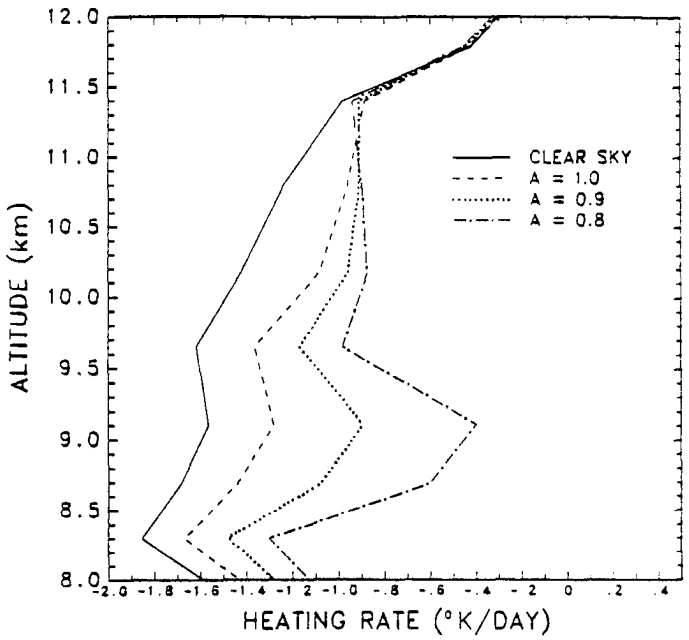

Figure 4.31: Infrared radiative heating rates for three values of a in a 3 km variable IWC cirrus cloud in the Wisconsin atmosphere.

Table 4.6 summarizes the longwave, shortwave and total (longwave + shortwave) energy budget of these cirrus clouds for the longwave, shortwave and total spectral regions. In the infrared, the cloud layer radiatively cools but at a lesser rate than the equivalent clear sky layer. In the solar wavelengths, atmospheric heating is enhanced by the presence of the cloud. In the case where $a = 1$ the atmospheric cooling in the infrared is greater than all the other heating influences combined. However, when $a = 0.8$ the heating within the cloud has increased such to change the net radiative cooling of the atmosphere to heating. This case emphasizes the sensitivity of the radiative characteristics of cirrus to a decrease in the effective crystal size of the ice size distribution.

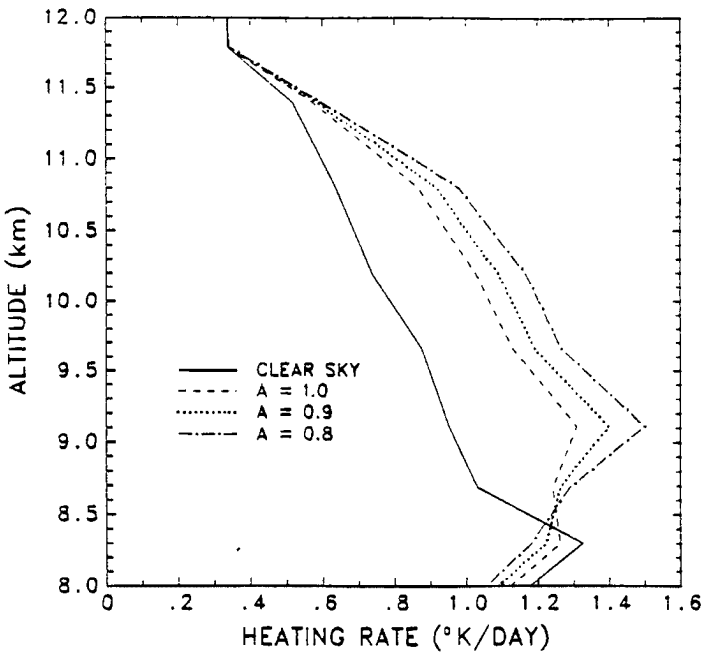

Figure 4.32: Solar radiative heating rates for three values of a in a 3 km variable IWC cirrus cloud in the Wisconsin atmosphere.

Table 4.6: Energy budgets of the the variable IWC cirrus cloud for three values of a represented in terms of differential net flux for the infrared, solar wavelengths and total spectra.

Spectral Interval	Differential Net flux $W \cdot m^{-2}$		
	$a = 1.0$	$a = 0.9$	$a = 0.8$
Infrared	-17.121	-14.699	-11.635
Solar	15.589	16.432	17.434
Total	-1.532	1.733	5.799

Figures 4.33 and 4.34 show solar and infrared spectral absorption for the entire cloud layer for this case. Figures 4.35 and 4.36 show the spectral albedos and spectral emittances for the solar and infrared wavelengths respectively. The spectral characteristics of this cloud are similar to those of the uniform cirrus cloud. These figures do show the sensitivity of the absorption and reflective properties of cirrus clouds to decreases in the effective crystal size. The spectral emittances and albedos of this cloud are low due to the optical thinness of the cirrus.

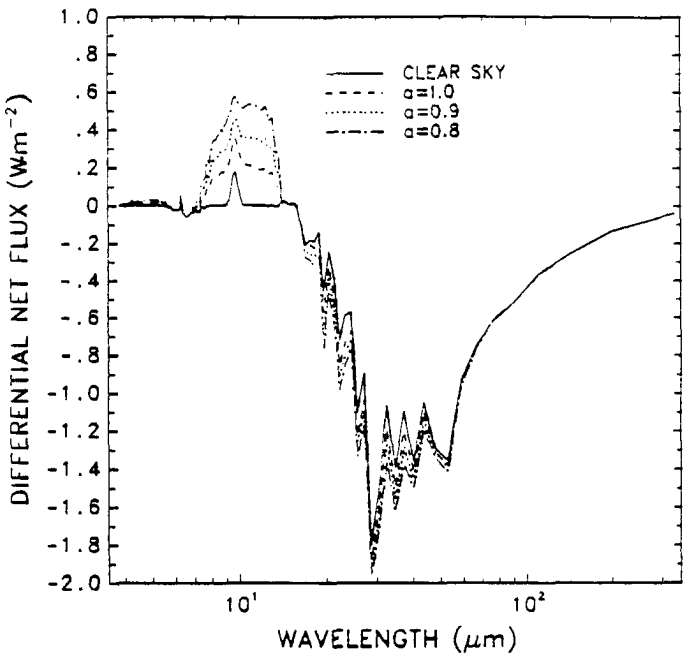

Figure 4.33: Spectral net differential fluxes in the infrared for a 3 *km* variable IWC cirrus cloud in the Wisconsin atmosphere with the values of a shown.

The simulations reported here show that the vertical structure of the ice water content affects the magnitude and shape of the heating rate profiles throughout the clouds. Since ice crystal growth is enhanced (suppressed) by radiative cooling (heating), this result is important to the evolution and dissipation processes within cirrus and its interactions with the environment. Additionally, it was shown that the net radiative effect of cirrus cloud in the atmosphere is highly sensitive to changes in the size distributions inside the clouds in that net cooling is changed to warming with the addition of small particles to the crystal size distributions, for the case examined above.

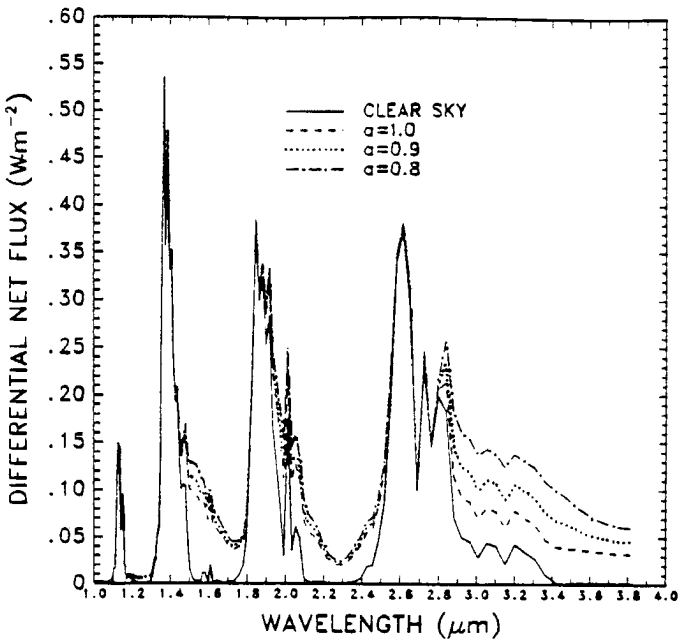

Figure 4.34: Spectral net differential fluxes in the solar wavelengths for a 3 *km* variable IWC cirrus cloud in the Wisconsin atmosphere with the values of α shown.

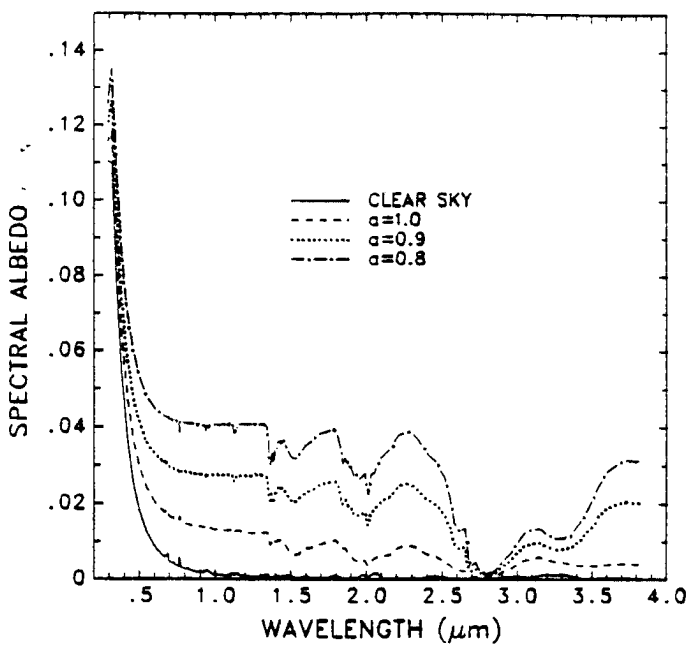

Figure 4.35: Spectral albedo in the solar wavelengths for a 3 *km* variable IWC cirrus cloud in the Wisconsin atmosphere with the values of α shown.

4.5 Summary

This chapter demonstrates the viability of the present two stream model applied to cloudy atmospheres especially cirrus cloudiness. Comparison to an established model produced heating rate agreement to within 5% for an arctic stratus cloud. Simulation of uniform cirrus in the tropical subarctic winter and the October 28, 1986 Wisconsin atmosphere showed the gross radiative characteristics of high thin clouds and their relation to height and temperature. The effects of small particles on the radiative properties of these clouds were also studied. Results showed enhanced absorption and thus emittances when the size distributions contain large amount of small particles. Albedos in the solar wavelengths were also enhanced. Lastly, the effect of a variable IWC profile was shown to greatly affect the shape of radiative heating profiles in that the heating maximum was shifted from near cloud top and base to the thickest part of the layer. The net energy budget of these cirrus clouds was also shown to be sensitive to changes in effective crystal size changing the net radiative cooling of a cloud to heating for the hypothetical case examined.

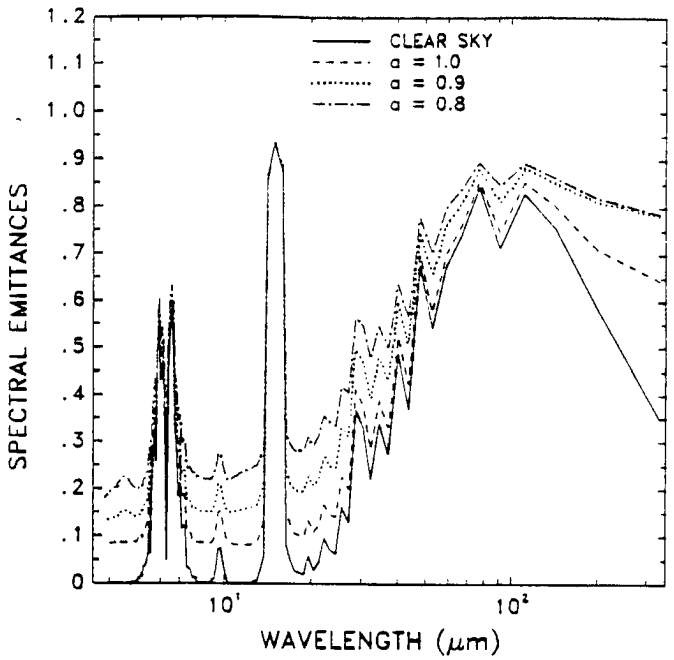

Figure 4.36: Spectral emittances in the infrared for a 3 *km* variable IWC cirrus cloud in the Wisconsin atmosphere with the values of a shown.

Chapter 5

OBSERVATIONAL AND THEORETICAL COMPARISON OF CIRRUS CLOUD RADIATIVE PROPERTIES

A theoretical examination of the properties of cirrus clouds in various atmospheres, with different ice water paths and size distributions having different effective crystal size was presented in the previous chapter. Only the observed microphysical properties of cirrus were used in these studies. In this chapter, an attempt is made to simulate more closely the conditions observed during the FIRE October 28, 1986 case. These simulations are compared to actual observations of the radiative characteristics of cirrus clouds and inferences are made concerning quality of the observations and the differences and similarities. The sensitivity of the model simulations to variable size distributions which translate into changes in the particle extinction, single scatter albedo and asymmetry factor are made in order to assess the relative importance of these parameters. This chapter is divided into two main sections. Firstly, the radiative, microphysical and environmental observations are described as well as the data reduction processes. Secondly, the comparisons between these observations and simulations are presented.

5.1 October 28, FIRE observations

The observations used in this study were obtained from instruments mounted on the NCAR Sabreliner which flew over the western shore of Lake Michigan in the vicinity of Green Bay Wisconsin during October 28, 1986 as part of the FIRE IFO period. The plane was flown through a thin banded cirrus deck having cloud base and top at approximately 8.5 *km* and 11.5 *km* respectively. A racetrack pattern at six different levels throughout the cirrus was performed between 1530Z and 1630Z (9:30 - 10:30 local time). The following three sections discuss the radiative, microphysical and environmental measurements. A

more detailed treatment of the radiative, microphysical and environmental observations collected during the cirrus case are presented by Smith, Jr. *et.al.* (1989), Heymsfield and Miller (1989) and Starr and Wylie (1989) respectively.

5.1.1 Radiative Measurements

Among the radiative measurements collected during the IFO by the Sabreliner are broadband flux measurements in the infrared (4.0 μm - 50.0 μm) and in the solar band (0.3 μm - 3.0 μm). Two Epply pyrogeometers were used to measure the upwelling and downwelling infrared radiation. Two Epply pyranometers with red domes were used to measure the upwelling and downwelling near infrared (0.7 μm - 3.0 μm) flux, while two others with clear domes were used to measure the entire solar wavelength spectrum. Observations from two photodiode detectors measuring radiance are used in this section. The two photodiodes have spectral responses throughout the entire short-wave spectrum and blue visible light (0.35 μm - 0.55 μm) for the detector measuring the downwelling and upwelling radiances respectively (Hein *et. al.*, 1987). The downward looking photodiode was part of the CSU Multidirectional Radiometer (see Davis and Cox, 1982). The instruments measuring downwelling and upwelling flux were mounted on the top and bottom of the aircraft fuselage respectively.

Albrecht and Cox (1976, 1977) and Smith, Jr. *et. al.* (1988) discuss the radiometers, their respective calibrations and sensitivities to cold temperatures. The data was processed applying these corrections and calibration procedures. In addition, flight information such as pitch, roll, heading and sun-earth geometry were used to correct the pyranometer data to a horizontal surface and to normalize it to a common time (see Rockwood and Cox, 1976; Ackerman and Cox, 1981). Absolute accuracies for the pyranometers and pyrogeometers are approximately $\pm$ 10 $W \cdot m^{-2}$ and $\pm$ 5 $W \cdot m^{-2}$ respectively.

5.1.2 Preliminary Analyses of the October 28 Cirrus Case

Figure 5.1 presents a time series at 11.4 km approximately corresponding to cloud top, for the IWC, Lyman-alpha voltage (proportional to water vapor amount), temperature,

upwelling infrared, total short-wave irradiance and the downward looking photodiode voltage (proportional to radiance). Figure 5.2 presents a time series at 9 km approximately corresponding to cloud base for the similar measurements but for downwelling radiation. These plots exemplify the vertical and horizontal inhomogeneities associated with the cirrus observed in this case. The standard deviations of the total downward shortwave irradiance increase toward cloud base to 30 $W \cdot m^{-2}$ while upward shortwave measurements increase toward cloud top to 25 $W \cdot m^{-2}$ corresponding to approximately 10% of the flux measurement at that height. Observed standard deviations in the upwelling infrared irradiance ranged from 5 - 10 $W \cdot m^{-2}$ with higher values at cloud boundaries. Comparison of Figs. 5.1 and 5.2 shows more high frequency variability at altitudes corresponding to cloud base than at cloud top. For example, the downward total shortwave irradiance is much more variable than the upwelling shortwave irradiance. Figure 5.1 shows considerable negative correlation between the infrared and solar upwelling fluxes. The cloud under the aircraft during this time becomes thicker and therefore more solar radiation is reflected while the cloud emits closer to its blackbody temperature. Comparison to Fig. 5.2 however, reveals much less correlation between the infrared and solar sensors. Cloud inhomogeneities in this case appear to be much greater at cloud base than at cloud top.

The large observed inhomogeneities cause confusion in the interpretation of the radiative characteristics of the cirrus. For example, in the shortwave absorption may be overestimated due to the leakage of radiation out of the sides of the clouds. McKee and Cox (1974) show that the albedo measured above finite clouds is greatly reduced compared to that of a cloud of infinite horizontal extent. These effects lead to error in the estimation of the transmission of these clouds. Emittances within the infrared can also be reduced significantly due to the effects of finite cloudiness (see Paltridge and Platt, 1981). Since the model developed in chapter 2 assumed a plane-parallel horizontally homogeneous atmosphere, the extent to which these inhomogeneities introduce error to the theoretical calculations requires evaluation. However, uncertainties in the radiative measurements and sampling errors due to the changing state of these clouds limit the ability to represent these clouds completely.

In recognition of this variability, the following analysis of radiation data is performed in such a way as to provide upper and lower limits which contain the bulk of the variability. This analysis involves averaging the observations after Smith *et.al.* (1989) who average the downwelling infrared irradiance and the IWC for the entire flight leg and the lowest and highest 30% of the irradiance and IWC values. These averages are meant to correspond to the mean, thin and thick limits of cloudiness. There is no attempt to correlate the IWC and downward infrared irradiances in the lower and higher 30% brackets. The aim is to gain insight into understanding the limits of the radiative characteristics observed on this day. Simulations of the cirrus cloudiness are performed using the variability of the observations and are compared to the averages as described above.

Figure 5.3a, b and 5.4a, b show the downwelling and upwelling total shortwave and longwave mean irradiance profiles through all six traverses inside the cirrus clouds (adapted from Smith, Jr. *et. al.*, 1989). It is apparent by examination of these data that the cirrus on south side of the racetrack (denoted as cloud 1) has different radiative characteristics than cirrus on the north side (denoted by cloud 2). This is shown by the similarity between the slopes of these vertical flux profiles. The flux profiles in both the longwave and the shortwave measurements are clearly offset to such an extent that inclusion of these irradiance values into one cloud is unjustified. For this reason cloud simulations are performed on this day for the two different sets of observations in an effort to reproduce the mean characteristics of each portion of the cloud.

5.1.3 Microphysical Measurements

The NCAR Sabreliner was equipped with two different Particle Measuring Systems (PMS) particle sizing probes. These particles were the 2D imaging type which detect particles as a two dimensional shadow of particles that pass through a sampling volume into which a laser beam is projected and detected by a photodiode array (see Heymsfield and Baumgardner, 1985 for more detail). The instruments (PMS 2D-C and 2D-P) were mounted under the wing of the aircraft. The C-probe (PMS 2D-C) effectively sampled particles from 44 μm to 1 mm in 50 μm increments (the resolution was 25 μm along the

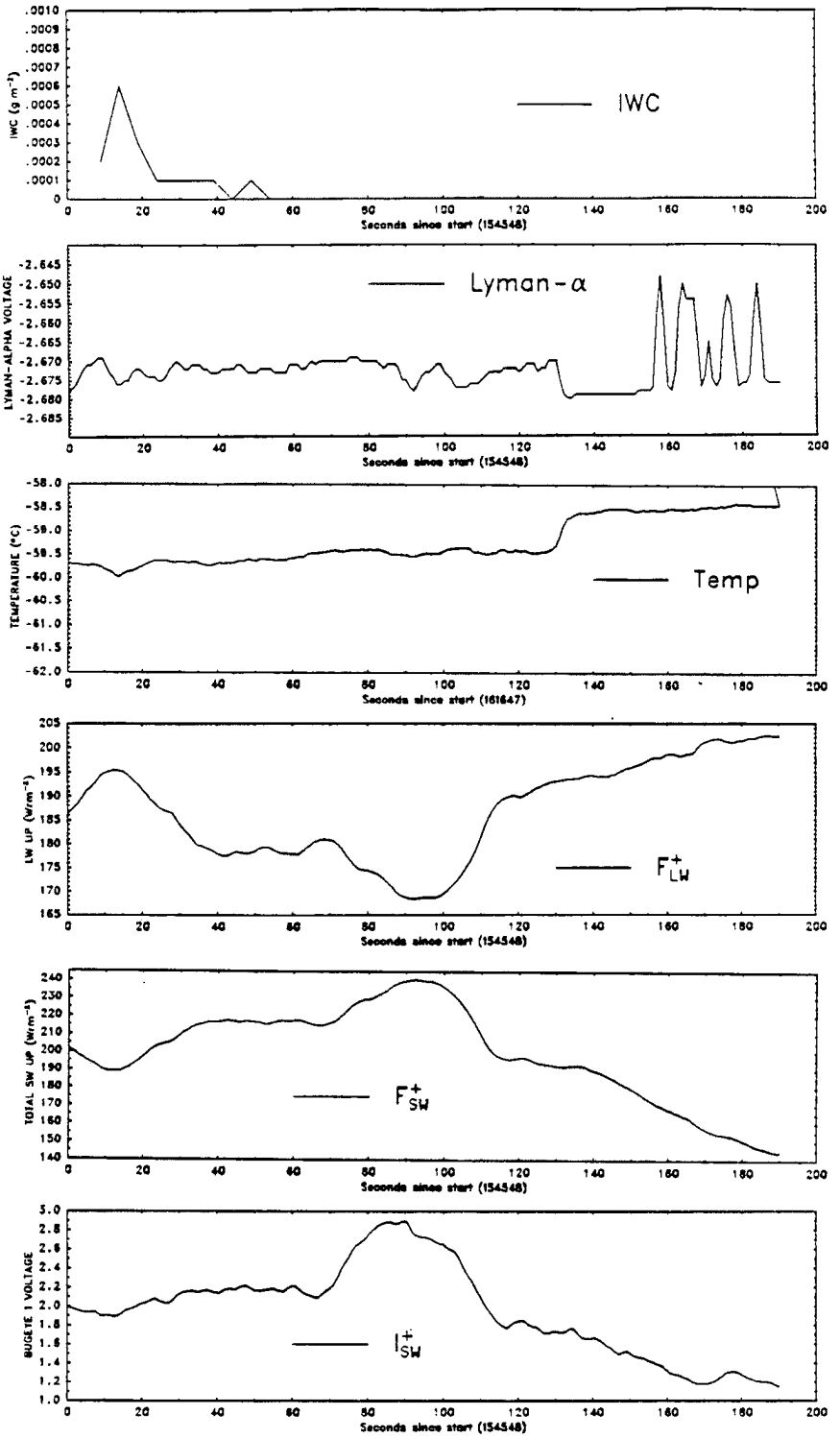

Figure 5.1: Time series for flight leg 2 at 11.4 *km* for the IWC, Lyman-alpha voltage, temperature, infrared upwelling flux, shortwave total upwelling flux and the downward looking photodiode voltage

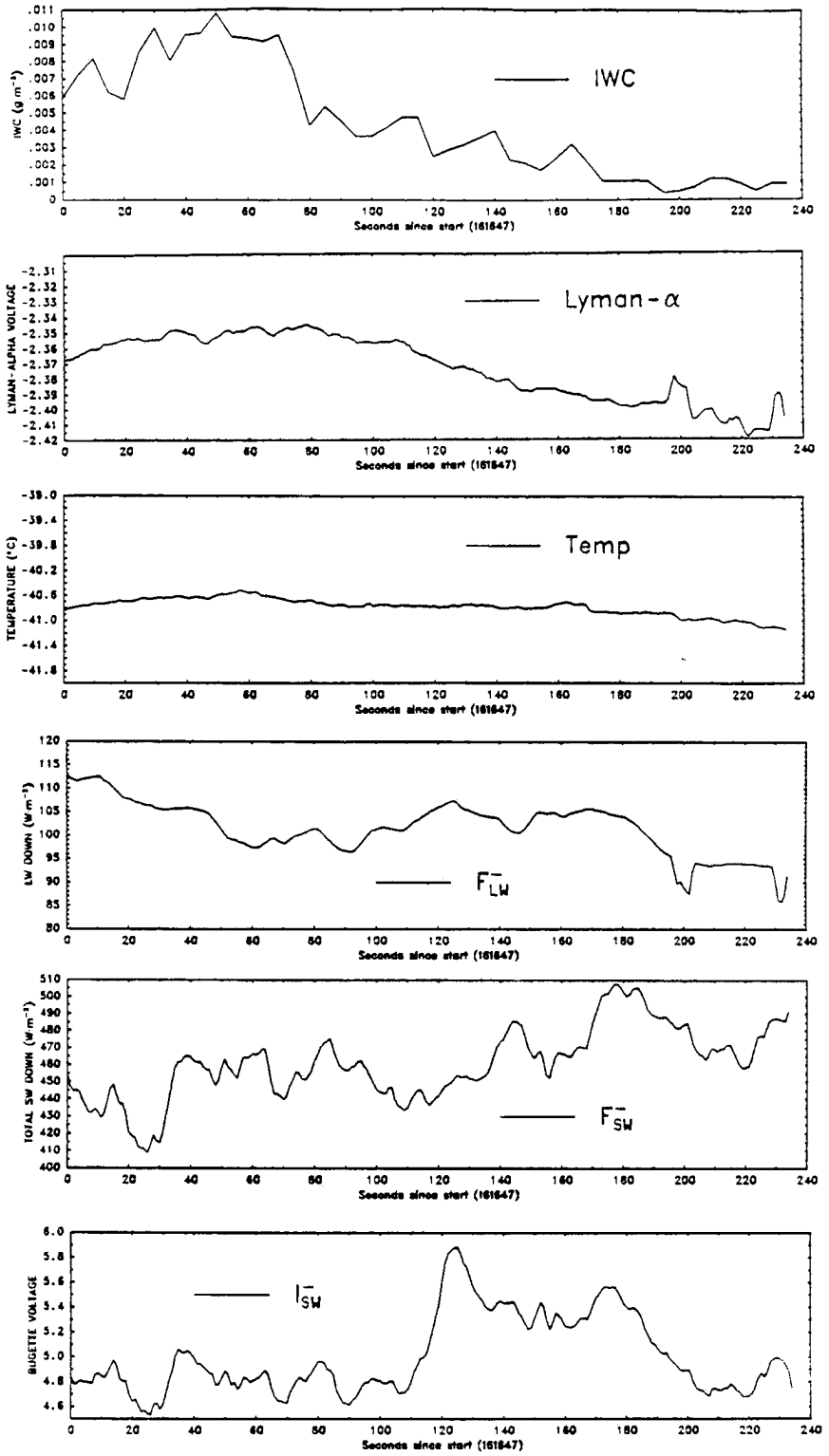

Figure 5.2: Time series for flight leg 5.5 at 9.0 *km* for the IWC, Lyman-alpha voltage, temperature, infrared downwelling flux, shortwave total downwelling flux and the upward looking photodiode voltage

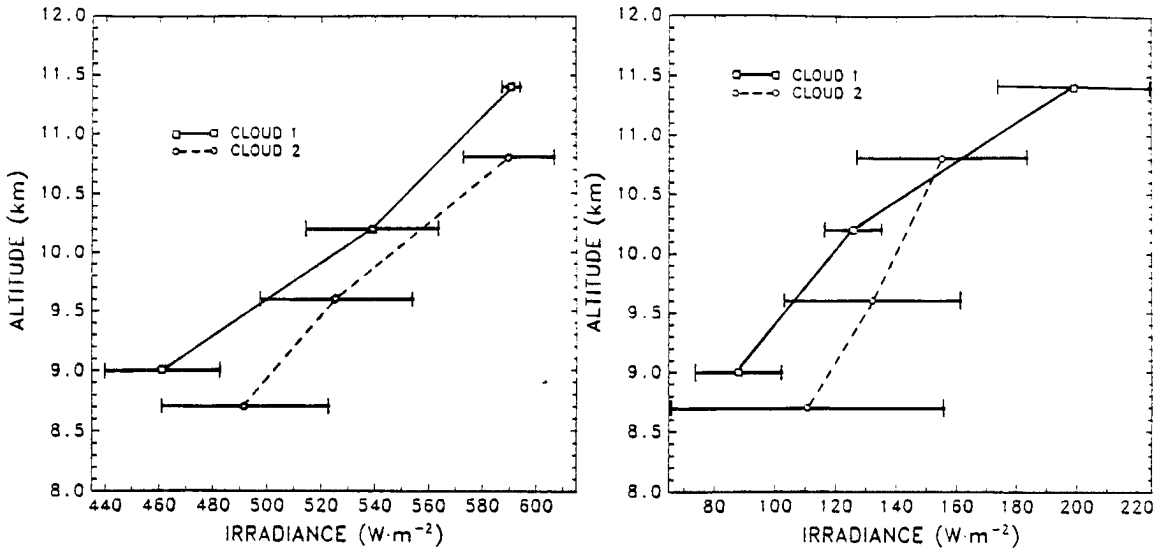

Figure 5.3: The (a) downwelling and (b) upwelling mean solar irradiance along with their respective standard deviations as a function of altitude for clouds 1 and 2.

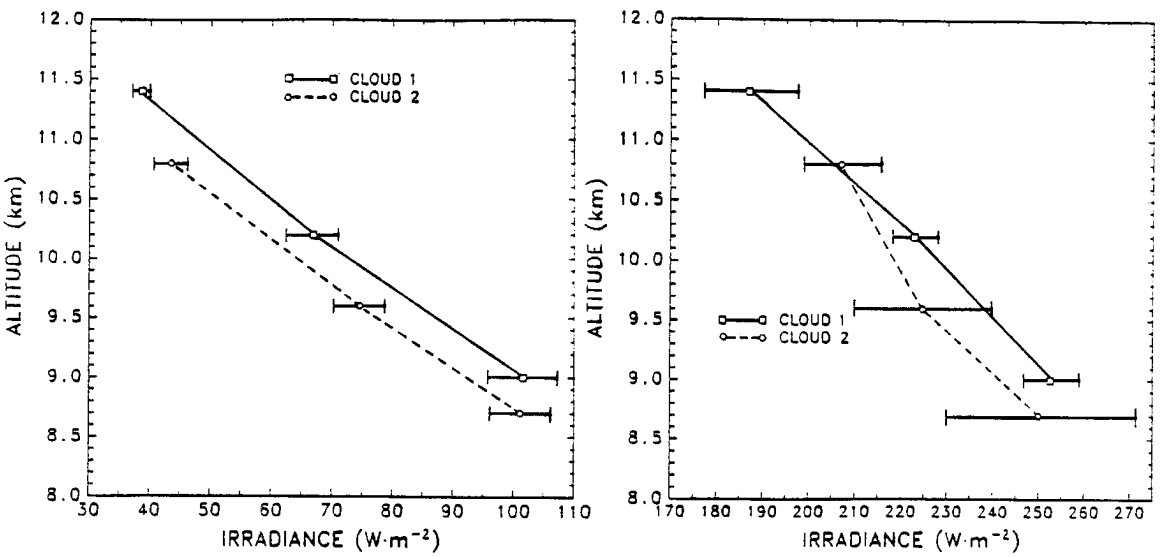

Figure 5.4: The (a) downwelling and (b) upwelling mean infrared irradiance along with their respective standard deviations as a function of altitude for clouds 1 and 2.

probe array axis and 44 μm in the direction of flight, see Heymsfield and Miller, 1989). The 2D-P probe measures particles from 300 μm to above 2 mm in size. The crystal size distributions presented in Figures 4.16-4.22 were the composite samples from both probes and are the microphysical data used in the cirrus simulations.

The 2D data were used to derive size spectra, particles shapes and ice water content. The particles imaged were sized into bins for which concentrations were calculated for every five seconds of flight time. Data from the 2D-C and 2D-P probes were combined to maximize the accuracy of the sampled size spectra. However, Heymsfield and Miller (1989) note that estimates of sampling volume and concentrations below 100 μm are questionable, due to the uncertainties associated with equation for depth of field of the probe versus particle size (see Heymsfield and Baumgardner, 1985). These observations point to the deficiency in measuring small particles during the experiment and further justify the discussion of chapter 4.

Figure 5.5 (Heymsfield, personal communication) shows the maximum particle dimension as a function of altitude. This figure reveals a trend of increasing particle size toward cloud base. Particle shapes were deduced based upon comparison of the particle area to an equivalent diameter sphere. Information about concentrations and particle shapes together with diameter-mass conversion relationships dependent on the particle habit were used to derive the IWC (see Heymsfield, 1977). The uncertainties in the derived IWC values were estimated to be approximately a factor of 2 (Heymsfield and Miller, 1989). Table 5.1 presents the mean, minimum and maximum IWCs throughout the cirrus clouds observed in this case as inferred from the 2D-C and 2D-P probes. The IWC has the most variability toward the cloud base where the cloud is thickest.

The radiative characteristics for this case study will be simulated using a range of IWCs and effective crystals sizes (assigned by varying the ratio a, see sec. 4.4.1) as shown in table 5.1. The microphysical crystal size distributions and their corresponding IWCs are assumed constant throughout a layer centered at the level of the aircraft flight track. Since the six legs are divided into the two clouds, the three cloud layers shown in table 5.1, are used in the radiative transfer calculations for each cloud. The depth of the layers

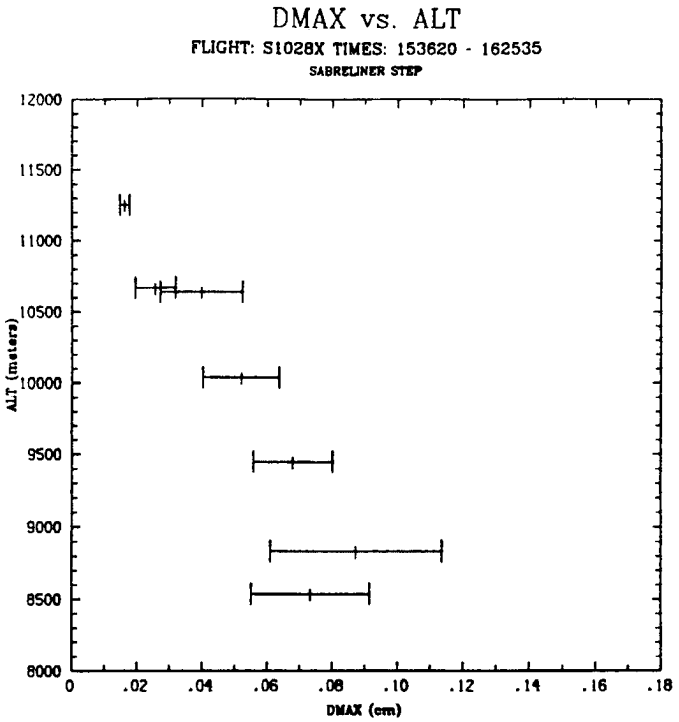

Figure 5.5: The maximum particle dimension (μm) as a function of altitude for the six separate racetrack legs. (Heymsfield, personal communication)

Table 5.1: Variation of the IWCs in the clouds observed during the Oct 28, FIRE case. The IWCs are assumed constant within the given layer. Ice Water Path (IWP) is also given for each profile.

	Cloud Layer		Ice Water Content ($g \cdot m^{-3}$)		
	Top (km)	Bottom (km)	Mean	Minimum	Maximum
Cloud 1	11.6	11.0	0.00019	0.00001	0.00040
	11.0	9.4	0.00200	0.00140	0.00290
	9.4	8.8	0.00471	0.00160	0.00780
	IWP ($g \cdot m^{-2}$)		6.140	3.206	9.56
Cloud 2	11.0	10.4	0.00019	0.00001	0.00050
	10.4	8.9	0.00242	0.00150	0.00330
	8.9	8.5	0.00292	0.00130	0.00450
	IWP ($g \cdot m^{-2}$)		4.192	2.776	7.05

are determined such that the area of the three histogram layers (layer depth × IWC) approximates the integral of the smoothed IWC vertical profile (see Figs. 5.6 and 5.7).

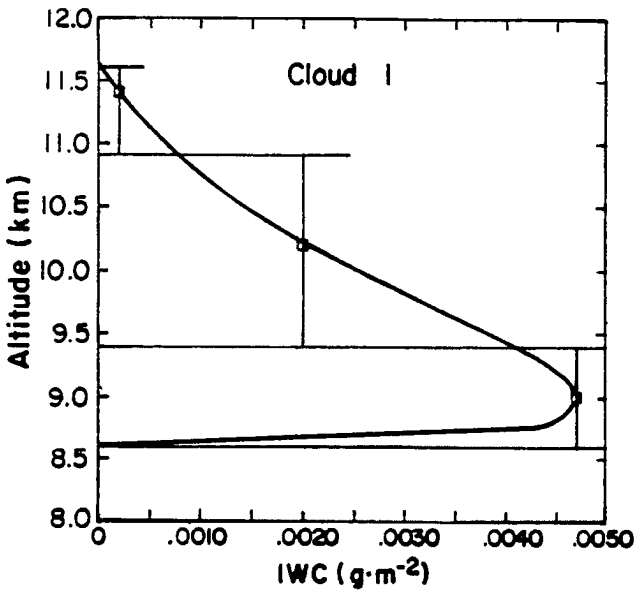

Figure 5.6: The smoothed mean IWC profile and the histogram areas which approximate its integral (IWP) for cloud 1.

5.1.4 Environmental Measurements

A simulation of the radiative properties of the cirrus clouds requires the vertical profile of pressure, temperature and moisture. Rawinsonde measurements were taken frequently within a special network grid. However, no rawinsondes were released during the Sabreliner flight times corresponding to cloud penetration (1530Z to 1630Z). Therefore a composite sounding corresponding to 1600Z is constructed using the soundings from Green Bay at 1400Z and 1730Z. The temperature and moisture profiles above 16 *km* are assumed to be the average of the McClatchey *et al.* (1972) mid-latitude summer and winter soundings. The entire ozone vertical profile is assumed to be that of this summer and winter average McClatchey sounding.

Especially important is the temperature and moisture within the cirrus cloud layer itself. This data is provided by the flight level data of the Sabreliner aircraft. Due to the extreme low temperatures observed within the cirrus cloud layers ($< -40°C$), the

moisture amount was difficult to determine. The dewpoint sensor on board the aircraft saturates at dewpoints below -55.0 ^{o}C corresponding to the sensor's minimum value (Hein *et. al.*, 1987). The Lyman-alpha instrument which measures water vapor amount, can only be calibrated relative to the dewpoint sensors. However, a calibration curve for the Lyman-alpha instrument was obtained for higher values of dewpoint temperature observed below cloud base and was extrapolated to the lower dewpoint temperatures within the the cloud layer. Uncertainties in the moisture amounts derived in this way are not fully understood. An alternative moisture amount is given by assuming saturation with respect to ice throughout the cloud. A comparison of the water vapor mixing ratio profiles are shown in Figure 5.8 (from Smith, Jr. *et. al.*, 1989). The profile inferred from observations shows a region at cloud top which is supersaturated with respect to ice and becomes more subsaturated with respect to ice toward cloud base. This profile is qualitatively similar to that which might be expected in a cirrus environment (see for example Ramaswamy and Detwiler, 1986).

For the reasons described above, the aircraft measurements corresponding to the north and south sides of the oval racetracks are assumed to describe two different clouds. The data taken on the south side of the racetrack are denoted as cloud 1 and from the north side as cloud 2. The atmospheric soundings used for these two cases are identical except within the cloud layer itself where the pressure, temperature and moisture measurements from the aircraft are employed. These data are interpolated to altitude levels so that the microphysical size distribution measurements and therefore the ice water content can be assumed constant throughout a cloud layer. The profiles of pressure, temperature and moisture within each cloud are shown in table 5.2. The atmospheric temperature and moisture profiles throughout the atmosphere are shown in Figure 5.9.

5.2 Observed and Simulated Radiative Characteristics of Cirrus Clouds

The cases examined in this section are used to evaluate the sensitivity of the radiative characteristics of cirrus clouds to the mean observations to the effects of water vapor amount, effective crystal size and IWC within the clouds. Cloud radiative heating rates, albedos and emittances as defined above are compared to observations. Model

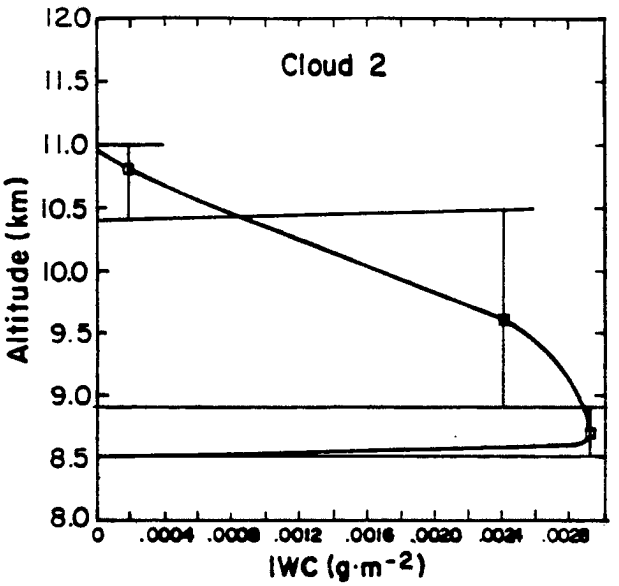

Figure 5.7: The smoothed mean IWC profile and the histogram areas which approximate its integral (IWP) for cloud 2.

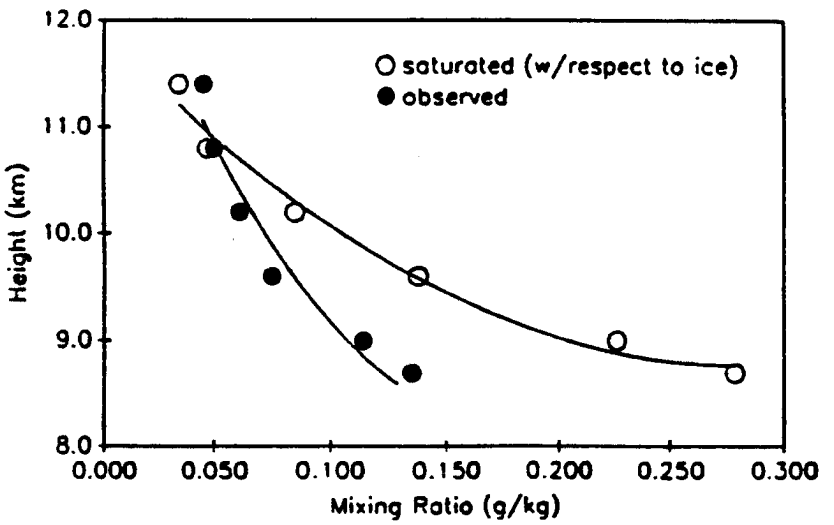

Figure 5.8: Comparison of the observed moisture profile from aircraft race track legs in cirrus during the Oct 28 and an imposed profile of saturation with respect to ice.

Table 5.2: In cloud environmental profiles of pressure (P), temperature (T), water vapor and ozone amounts (ρ_{O_3}). Water vapor amount are given for both the observed (ρ_{v_o}) and assumed (saturation with respect to ice, ρ_{v_i}) profiles.

	Alt. (km)	P (mb)	T (^oK)	ρ_{air} ($g \cdot m^{-3}$)	ρ_{v_o} ($g \cdot m^{-3}$)	ρ_{v_i} ($g \cdot m^{-3}$)	ρ_{O_3} ($g \cdot m^{-3}$)
Cloud 1	11.6	210.0	213.3	3.431×10^2	1.3×10^{-2}	1.1×10^{-2}	1.8×10^{-4}
	11.0	231.3	217.2	3.738×10^2	1.9×10^{-2}	1.8×10^{-2}	1.7×10^{-4}
	9.4	295.8	229.4	4.558×10^2	4.1×10^{-2}	7.9×10^{-2}	1.2×10^{-4}
	8.8	323.1	233.4	4.743×10^2	8.4×10^{-2}	1.2×10^{-1}	1.1×10^{-4}
Cloud 2	11.0	231.0	216.0	3.723×10^2	1.8×10^{-2}	1.6×10^{-2}	1.7×10^{-4}
	10.4	253.9	220.1	4.012×10^2	2.4×10^{-2}	2.6×10^{-2}	1.5×10^{-4}
	8.9	318.2	232.5	4.764×10^2	5.8×10^{-2}	1.1×10^{-1}	1.1×10^{-4}
	8.5	337.4	235.6	4.986×10^2	1.1×10^{-1}	1.6×10^{-1}	9.8×10^{-5}

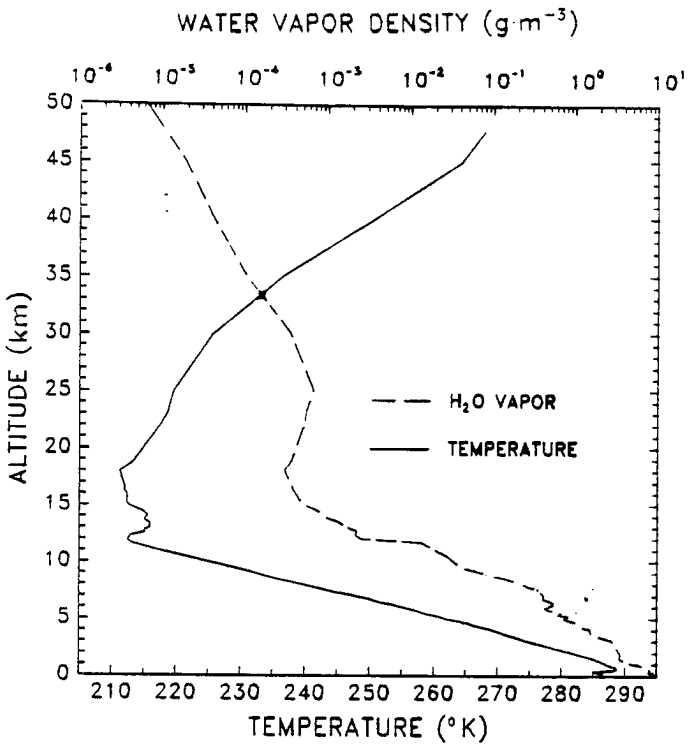

Figure 5.9: The composite 1600Z atmospheric temperature and water vapor profile for the observed and saturated with respect to ice conditions for clouds 1 and 2 on Oct. 28, 1986 near Green Bay, Wisc.

initialization and details of the specific cases simulated are described in detail in section 5.5.2.

5.2.1 Derived flux quantities

The observed and computed quantities describing the radiative properties of cirrus clouds to be compared are the radiative fluxes, radiative heating rates, longwave emittances (upward and downward) and shortwave absorptances and albedos. Radiative fluxes are compared directly from simulation results and observations, while radiative heating rates are computed.

It is useful to analyze the longwave flux measurements in terms of the longwave upward and downward emittances which are defined as follows (see Cox, 1976)

$$\epsilon^{+} = \frac{F^{+}(\tau_0) - F^{+}(0)}{F^{+}(\tau_0) - \pi B(\overline{T})} \tag{5.1}$$

and

$$\epsilon^{-} = \frac{F^{-}(0) - F^{-}(\tau_0)}{\pi B(\overline{T}) - F^{-}(0)} \tag{5.2}$$

where B $(\overline{T})$ is the Planck function for the mean cloud temperature $(\overline{T})$ integrated over the spectral response of the detector and τ_0 is the optical depth of the cloud from top to cloud base.

The shortwave absorption and albedo of the cirrus are defined after Paltridge and Platt (1981) as:

$$a = \frac{[F^{-}(0) - F^{+}(0)] - [F^{-}(\tau_0) - F^{+}(\tau_0)]}{F^{-}(0) + F^{+}(\tau_0)} \tag{5.3}$$

and

$$\alpha = \frac{\{F^{-}(0)[1-a] - F^{-}(\tau_0)\}}{F^{-}(0) - F^{+}(\tau_0)} \tag{5.4}$$

The quantities are derived both from observations and from computations and comparisons of these quantities are used to assess the ability of the model in simulating the radiative transfer through cirrus.

5.2.2 Simulations

The simulations performed for comparison with the observed cirrus were initialized in much the same way as discussed in section 4.3. The spectral bands of the model were adjusted to correspond with the spectral range of the detectors (SW 0.3 μm - 2.8 μm, LW 4.0 μm - 50 μm). The atmospheric sounding described above is used and the water vapor densities within the cloud layers are those specified in Table 5.2. The surface temperature is assumed to be equivalent to the lowest height in the sounding. The solar zenith angle is 61.3° as given by the local time (1600Z) and location of the aircraft. A surface albedo of 0.072 is used corresponding to the albedo over Lake Michigan given the solar zenith angle above. The amount of CO_2 is defined as 330 ppm while 0_2 is defined as 2.095×10^5 ppm (McClatchey *et al.*, 1972). The assigned ozone amount was discussed above.

Table 5.3 lists the simulation cases performed using the above conditions. Three different profiles of the ratio a were used for each cloud. Profile one corresponds to simulations assuming the measured size distributions ($a = 1$) in the three layers taken to represent the cloud. Profile two corresponds to the situation in which high concentrations of small ice crystals exist in the upper layer with decreasing concentration toward cloud base. Profile three corresponds to the case with large concentrations of small ice crystals throughout the cloud. Three simulations for each of these profiles were performed assuming IWCs which were taken to represent the range of IWC variability of the two flight legs and the mean of this variability as shown in table 5.1.

Table 5.3: The vertical profile of the large particle IWC to total IWC ratio a representing three separate effective size distribution profiles used to simulate the observations. Each profile is used for three cases corresponding to the mean, minimum and maximum IWC's shown in table 5.1. The effective radii have units μm.

Layer	Cloud 1						Cloud 2					
	Profile 1		Profile 2		Profile 3		Profile 1		Profile 2		Profile 3	
no.	a	r_e	a	r_e	a	r_e	a	r_e	a	r_e	a	r_e
1	1.0	48.06	0.8	35.92	0.8	35.92	1.0	76.81	0.8	51.86	0.8	51.86
2	1.0	116.25	0.9	83.53	0.8	64.35	1.0	181.81	0.9	109.81	0.8	77.41
3	1.0	220.22	1.0	202.22	0.8	82.66	1.0	159.58	1.0	159.58	0.8	73.74

5.2.3 Water Vapor Effects on Cirrus Clouds

Figures 5.10 and 5.11 show the effect of the moisture amount in cloud 1 on the solar and infrared radiative heating rates. The observed clear sky heating rate refers to the moisture profile produced from aircraft data while saturation with respect to ice is assumed for the other profile. The heating rates of both profiles without the presence of cloud particles are presented in both figures. Comparison in the infrared indicates that the profile with enhanced moisture amount produces greater cooling. In the presence of small particles, a smaller infrared heating rate is produced in the cloud with the enhanced moisture of the saturation water vapor profile as opposed to the drier observed water vapor profile. In the solar wavelengths, the ice saturation water vapor profiles produce greater heating rates than the drier observed profile. Thus larger water vapor amounts are shown to enhance cooling in the infrared and heating in the solar wavelengths. This is caused by the enhancement of gaseous optical paths. Note that the net effect of the radiative cooling and heating changes caused by increased water vapor amount is approximately zero because enhanced cooling in the infrared is offset by enhanced heating in the solar bands.

5.2.4 Comparison of Observed and Computed Radiative Heating Rates

The computation of radiative heating rates from observations is subject to considerable uncertainty due to cloud inhomogeneities and sampling errors. Computed standard deviations of the observed flux measurements give maximum variations in the cloud layer divergences of $\pm$ 20 $W \cdot m^{-2}$ and $\pm$ 60 $W \cdot m^{-2}$ for the infrared and solar wavelengths respectively. Considering the thickness of clouds one and two, these maximum uncertainties in the divergences correspond to variations in the radiative heating rates of $\pm 2° K/day$ and $\pm 5° K/day$ in the infrared and solar wavelengths respectively. These uncertainties are too large to obtain precise observation simulation comparisons.

However, Smith *et al.* (1989) present infrared radiative heating rates for both clouds 1 and 2 of the present case by correcting the upwelling flux using a broadband emissivity model. The corrected upwelling fluxes were observed to be within the range of variability

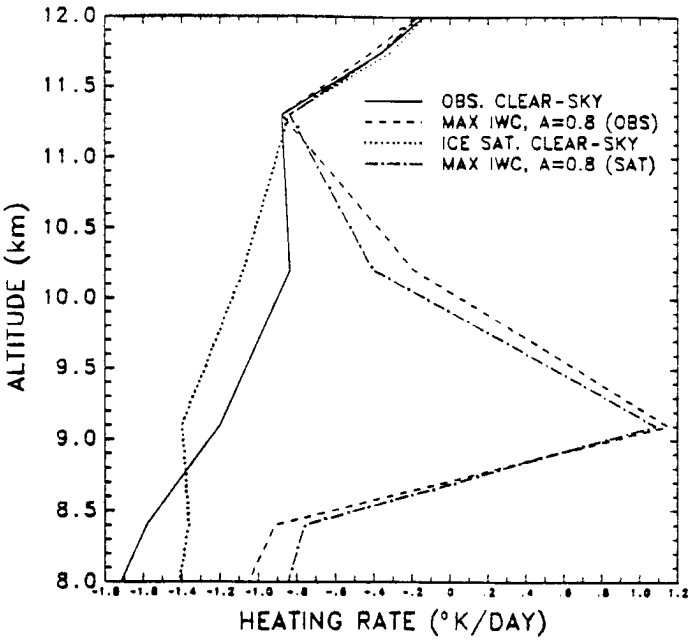

Figure 5.10: Comparison of the effect on the clear-sky and thick cloudy sky infrared radiative heating rate profiles with the observed and saturated with respect to ice water vapor profiles in cloud 1.

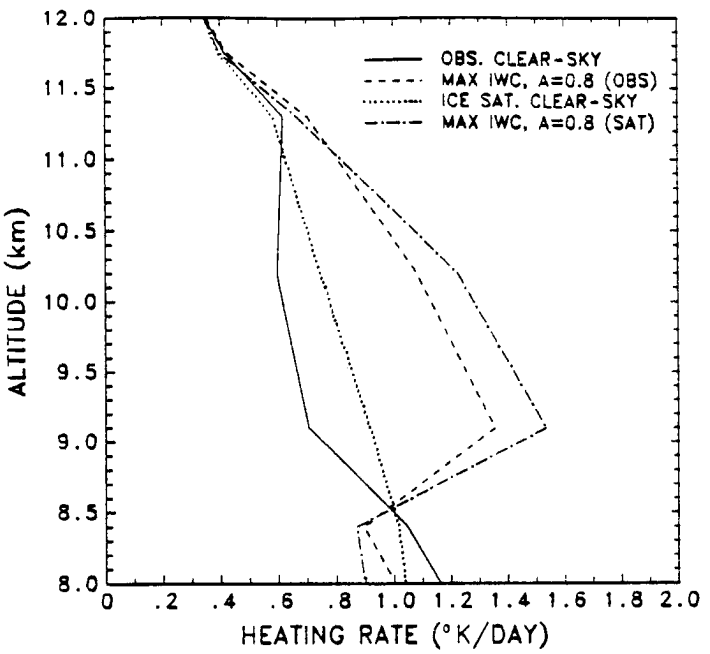

Figure 5.11: Comparison of the effect on the clear-sky and thick cloudy sky solar radiative heating rate profiles with the observed and saturated with respect to ice water vapor profiles in cloud 1.

of the measured fluxes. These radiative heating rates are presented with their associated uncertainties along with the simulated infrared radiative heating profiles in Figs. 5.12 and 5.13 for clouds 1 and 2 respectively. The three simulated curves present the limits of the variability of the IWP profiles and the small particle concentrations shown in tables 5.1 and 5.3.

In both clouds 1 and 2 all the simulated results even the clear-sky results lie within the uncertainties of the measurements themselves. This makes a quantative evaluation of the simulated results impossible. Qualitatively, figures 5.12 and 5.13 show similar results in that heating rates at cloud base are greater than heating rates at cloud top and may become negative. The simulated radiative heating profile which corresponds best to observed heating rates is the profile that corresponds to the cloud having the most small particles. Thus, these results indicate that simulated clouds with larger concentrations of small particles produce heating rates that are more consistent with the observed cirrus radiative heating rates. However, this result is not conclusive and must be further tested by comparing observations of emittance to the emittances produced from the simulation cases.

Figures 5.14 and 5.15 show the simulated solar radiative heating profiles. The solar measurements are affected by spatial inhomogeneities predominantly through scattering as described in section 5.1.2. This leads to more poorly defined flux profiles shown by the extreme variability cited above. Comparison of observed to simulated solar radiative heating rates gives meaningless results.

5.2.5 Emittances and Albedos

The infrared downward and upward emittances, solar absorptances and albedos were computed from both the observations and simulation results using equations 5.1-5.4. The results for the infrared downward and upward emittances and solar albedos are plotted in Figures 5.16 - 5.18 respectively.

The model results indicate that the emittances and albedos of clouds 1 and 2 increase monotonically with IWP up to 20 $g \cdot m^{-2}$. Also, despite small differences in the observed

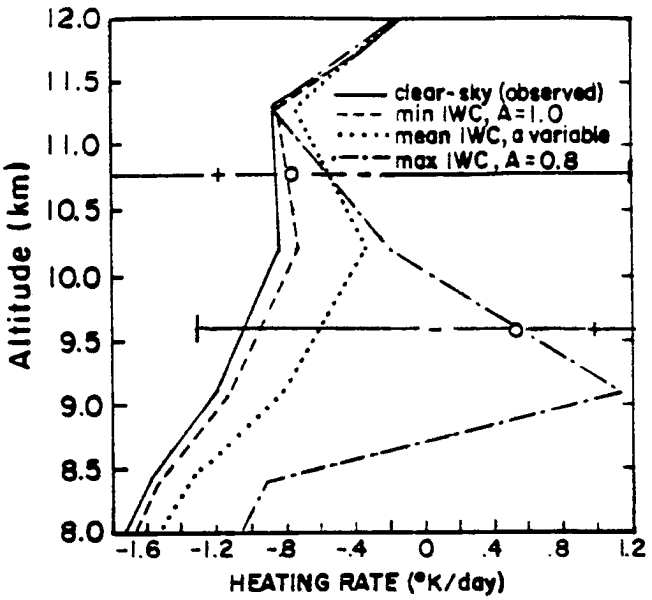

Figure 5.12: The infrared radiative heating rates from the stratified observations (denoted by (+) for thick cloud, (o) for mean and (-) thin cloud) and the simulations.

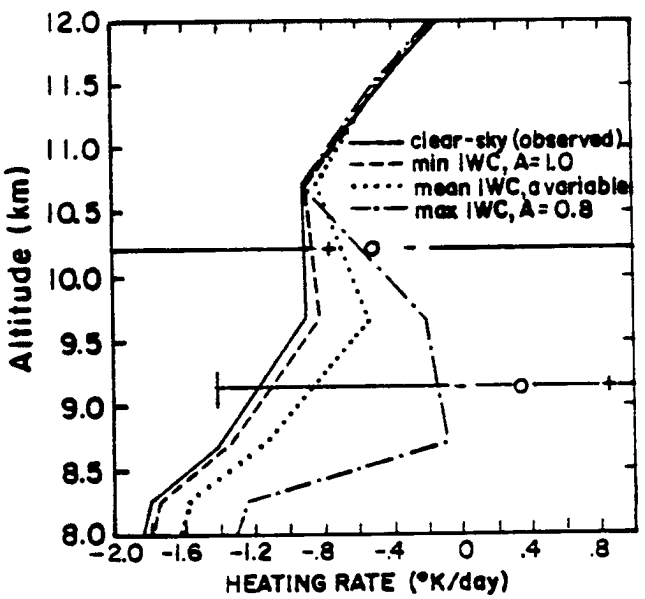

Figure 5.13: Same as 5.12 except for cloud 2

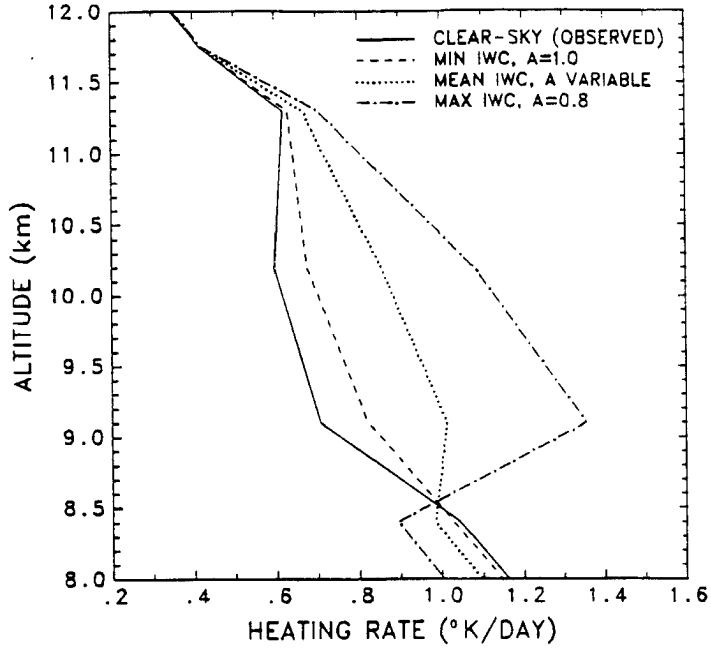

Figure 5.14: Simulated solar radiative heating rates for cloud 1.

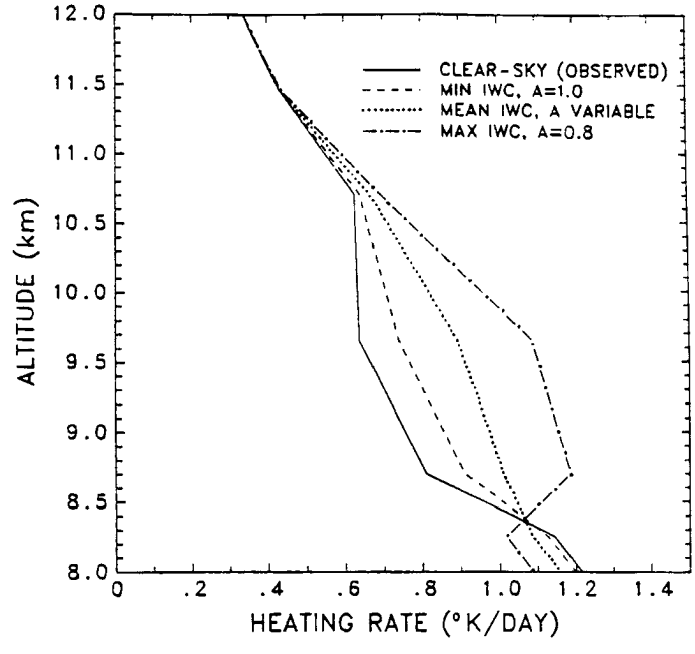

Figure 5.15: Simulated solar radiative heating rates for cloud 2.

crystal size distributions between clouds 1 and 2, the values of emittances and albedos mainly align according to the specified profile of small particle concentration shown in table 5.3. Thus the emittances and albedos the magnitudes of which are determined by the effective crystal radius of the size distributions, are smooth functions of IWP.

Figure 5.16 shows the calculated and observed infrared downward emittance as a function of IWP. The observations, computed using flux measurements and the IWP data, are plotted as cross points. The downward emittances are significantly greater than those predicted by the model (open symbols) even for the case where crystals with less than 50 μm contribute to 20% of the IWC throughout the cloud. The results suggest that size of the crystals must be significantly smaller than those assumed in the calculations in order to more properly simulate the cirrus observed here. Figure 5.17 also shows a similar type of discrepancy for the upward emittance.

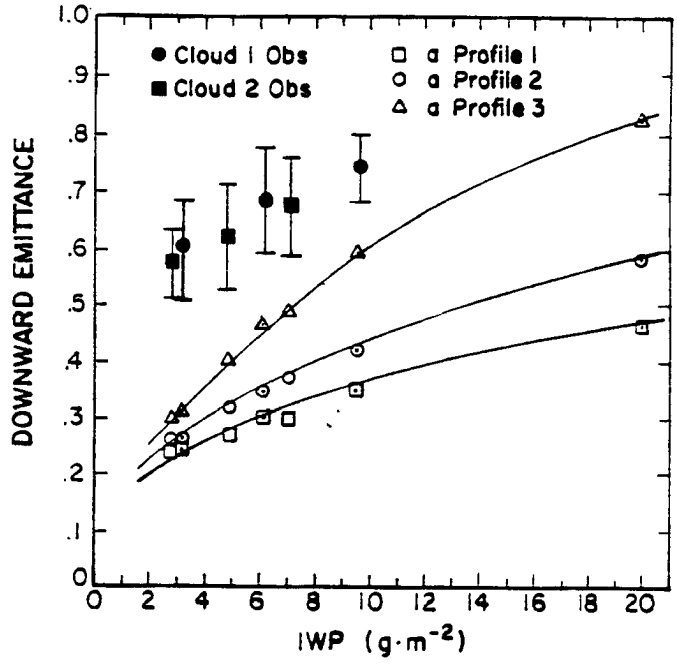

Figure 5.16: The variation of the downward emittance with IWP ($g \cdot m^{-2}$) computed from observed measurements for cloud 1 and cloud 2 and the simulated emittances for the three profiles of the ratio a and the two clouds (cloud 1 denoted by center dots) as shown in table 5.3.

Figures 5.18 presents the comparisons of the albedo-IWP relationships. Similar to the emittances, these comparisons demonstrate a consistent bias between the calculated and

observed relations although the integrity of the cloud 1 data especially for the albedos must be questioned. This comparison demonstrates that the effective crystal size assumed for the size distributions which were used to generate the cloud albedos must be significantly reduced. These comparisons are perhaps expected since the small ice crystals were not sampled.

5.2.6 The Role of the Asymmetry Parameter

Figure 5.19 presents a scatter diagram of the relationship between albedos and emittance in the observed cirrus clouds. The observations are plotted using four different symbols to represents the upward and downward emittances of each cloud. Interestingly all case simulations regardless of effective crystal size or IWP fall on the dashed lines shown on Fig. 5.19 for upward and downward effective emittances. This is a surprising result in that the observations lie well above these curves and have much steeper slopes than the relationships computed by the model. This result suggests that the size of the ice particles that are required to match the observations of emissivity are different from the size of the ice particles required to explain the albedo discrepancies.

Referring to Figure 5.19 two other curves are drawn corresponding to the simulation cases where the asymmetry parameter g is held constant at 0.7 (eg. Stephens *et al.*, 1989). Note that these curves show much better agreement to the observed emittance albedo relationships. Figure 5.20 shows the variation of the asymmetry parameter throughout the solar wavelengths as derived from the observed measured size distribution and the distribution where $a = 0.8$. Note that the g is decreased with addition of small particles and reduction of effective crystal size. However, the asymmetry parameter is also determined by the shape of the particle. For the case considered, the decrease of g is approximately 1.3% which is evidently not enough to cause considerable deviation from the curve plotted in Figure 5.19.

The asymmetry parameter is unaffected by the increase of concentration of the small particles even though the effective size of the size distribution is decreased. Thus although the addition of small particles to particle size distribution will improve the ability of the

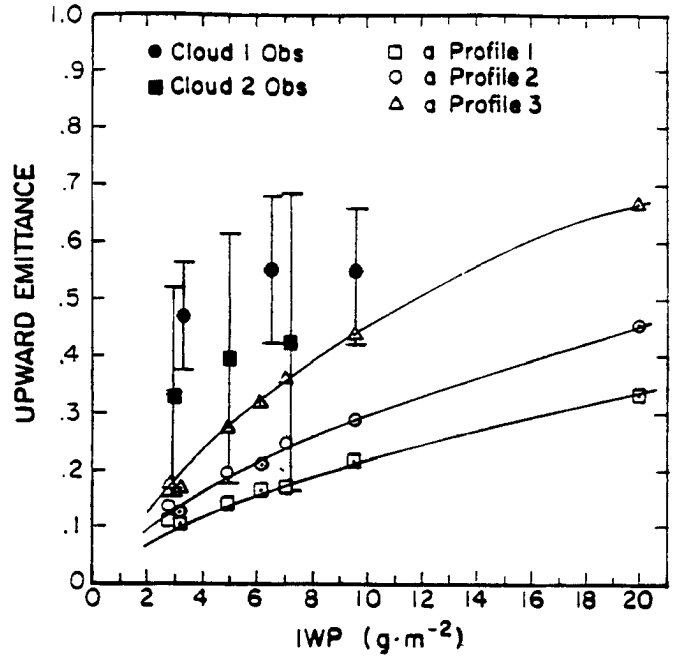

Figure 5.17: The variation of the upward emittance with IWP ($g \cdot m^{-2}$) computed from observed measurements for cloud 1 and cloud 2 and the simulated emittances for the three profiles of the ratio a and the two clouds (cloud 1 denoted by center dots) as shown in table 5.3.

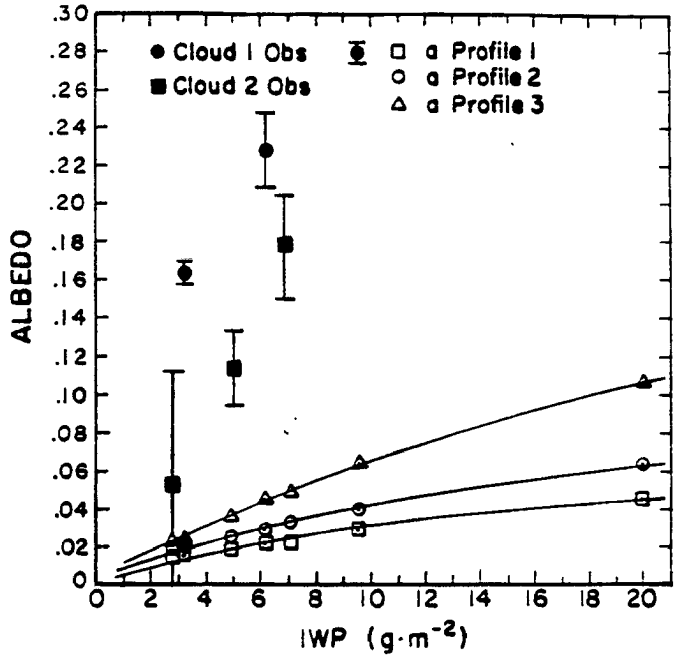

Figure 5.18: The variation of the albedo with IWP ($g \cdot m^{-2}$) computed from observed measurements for cloud 1 and cloud 2 and the simulated emittances for the three profiles of the ratio a and the two clouds (cloud 1 denoted by center dots) as shown in table 5.3.

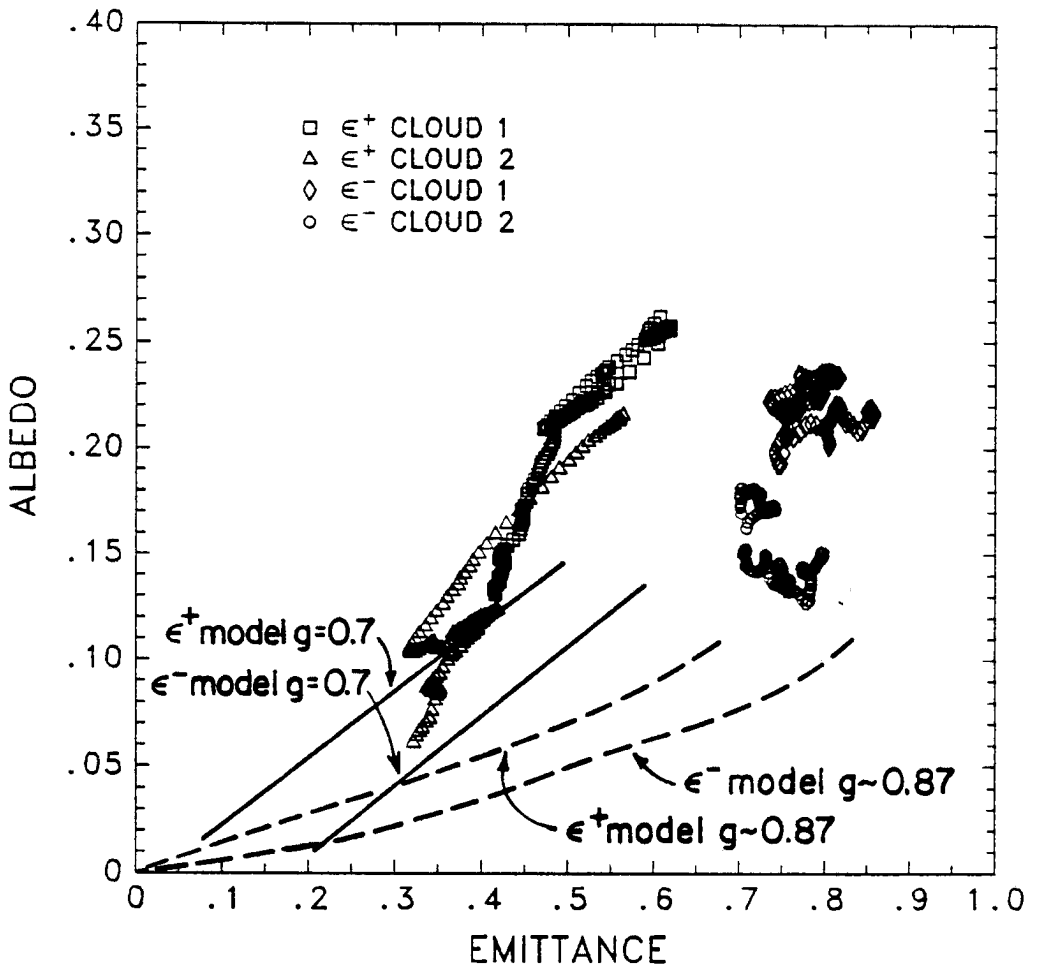

Figure 5.19: The relationship between the albedo and the downward and upward emittances from the observed measurements and the simulations for the two clouds. Solid lines denote simulations listed in table 5.3, dashed lines denote simulations with shortwave $g = 0.7$.

model to simulate cirrus cloud heating rates, emittances and albedos the overestimation of the asymmetry parameter may lead to greater differences between the observed and simulated radiative characteristics of cirrus clouds.

5.3 Summary

This chapter compared the observed properties of cirrus clouds to simulations employing the two-stream radiative transfer model developed in Chapters 2 and 3. Comparisons revealed that the addition of the amount of small particles in size distributions produces heating rates, emittances and albedos which agree more closely with cirrus cloud radiative observations. This is found despite the large uncertainties associated with the data. However, the comparison between the observed and simulated albedo-emittance relationship suggest that the size of the ice particles required to match the observations of emittance are different from the size of ice particles required to explain the albedo discrepancies. It was concluded that proper derivation of the albedo-emittance relationship requires both the inclusion of effects of small particles and some account of particle shape on the solar asymmetry parameter which is overestimated by the equivalent sphere approximation.

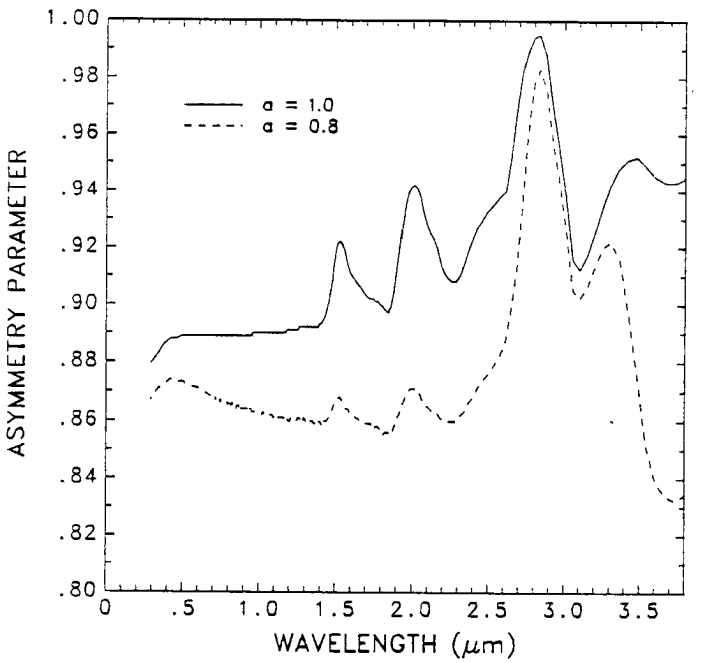

Figure 5.20: The spectral variation of the asymmetry parameter for an observed size distribution with no small particles (a=1.0) and with small particles included (a=0.8).

Chapter 6

SUMMARY AND CONCLUSIONS

An understanding of the way radiation interacts with clouds is vital for understanding the sensitivity of the earth's climate to both natural and anthropogenic changes in the atmosphere. Cirrus clouds are thought to be an important modulator of climate sensitivity. Stephens *et al.* (1989) show the that the feedback effect of cirrus on climate can be positive or negative depending upon the microphysics and scattering properties of the cloud. These properties of cirrus clouds are not well understood partly because of their thin tenuous nature and partly because of their microphysical properties. The high altitude and cold temperatures within these clouds along with their transparency greatly increase the difficulty in which accurate measurements can be obtained and interpreted both by aircraft and remote sensing. Thus the understanding of the interaction of radiation in cirrus clouds is crucial to determining the ways in which these clouds interact with climate forcings.

The purpose of the present work is to develop a two stream radiative transfer model which may be used to examine the properties of cirrus and to compare these simulations with the observations obtained during the FIRE experiment. Thus three tasks have been performed in this present research:

1. the development and testing of a two stream radiative transfer model,
2. a theoretical examination of the characteristics of cirrus clouds in various atmospheres and size distributions, and
3. the comparison of observations to model simulations.

The following sections summarize and draw conclusions from the tasks performed in this research. The final section presents recommendations for future research and speculations as to possible cirrus parameterizations schemes.

6.1 Summary of the Radiative Transfer Model

The development of an appropriate radiative transfer model is the cornerstone of the present research. The simulation of cirrus clouds requires the consistent treatment of the physical processes involved during the interaction of the cloud and radiation. Processes such as molecular and particulate absorption and scattering are required to be solved simultaneously. In addition a model of relative simplicity was desired so that future parameterizations may be based on the formulation.

The two stream model was chosen and formulated to satisfy the above criteria. The simplifying assumptions of a plane-parallel atmosphere, horizontal homogeneity and azimuthal symmetry were made. The diffuse solutions were represented in terms of reflectance and transmittance coefficients and source terms which treat the single scattering of the direct collimated beam of radiation in the solar wavelengths (0.28 μm - 3.8 μm) and thermal emission in the infrared (3.8 μm - 200.0 μm).

The two stream model was also adapted to account for molecular absorption in the form of the narrow band K-distributions and exponential sum fitting gaseous absorption data as input. The absorbing gases included were H_2O, CO_2 and O_3 in both the solar and infrared wavelengths as well as O_2 absorption which was included for the solar bands wavelengths. Solar absorption by O_3 for wavelengths less than 0.68 μm was computed using sum of exponential fit data. As a first approach, the narrow band data from the K-distribution tables having resolutions of 20 cm^{-1} and 50 cm^{-1} in the infrared and solar wavelengths respectively were employed. Optical paths were computed using the simple pressure temperature scaling parameterization with constants given for each gas by Chou and Arking (1980), Chou and Arking (1981), Chou and Peng (1983) and Chou (1984). Processes such as Rayleigh scattering and e-type absorption were also included in the model so that all relevant physics were represented.

Besides the molecular absorption and molecular scattering data, the two stream model also provided a way of treating cloud particle scattering and absorption. Particle extinction, single scatter albedo and asymmetry parameter are provided by Mie solutions given particle size distributions and indices of refraction. While the phase functions of the particles are also given by Mie solutions, the Henyey-Greenstein is used to approximate the phase function in all simulations presented here. Optical depths are calculated from the particle extinctions and are then used along with molecular optical depths to scale the single scatter albedos and asymmetry factors after Slingo and Schrecker (1982). Additionally, in the solar wavelengths the phase function is scaled using the Rayleigh and particle optical depths.

Test runs of an earlier version of the model produced instabilities that arose for three different reasons. Numerical instabilities occurred due to the way the reflectance and transmittance coefficients were formulated as functions of optical depth. The reflectance and transmittance coefficients were reformulated to remedy the problem. A second numerical instability was discovered in the formulation of the infrared source terms for very small optical depths. This condition occurs mainly in the upper clear sky atmosphere where molecular optical depths were computed to be less than 10^{-8}. An alternate expression of the infrared source term was also developed for this case to remove the problems. The recognition and correction of this instability represents a new contribution to the development of the two stream radiative transfer model and is necessary for the application of the model to the entire atmosphere instead and all infrared wavelengths. The final instability noted in the formulation of this radiative transfer model was caused by the singularity apparent in the shortwave source term. An alternate solution to the radiative transfer equation for this case was also developed to avoid this problem.

6.2 Model Results

The model was tested by comparing clear-sky and cloudy-sky simulations to published literature and to an established more complicated model. Clear- sky comparisons to line-by-line models were performed in both the infrared and solar wavelengths and a shortwave cloudy-sky simulation was compared to an established n-stream radiative transfer model.

6.2.1 Clear-Sky Simulations

The infrared clear-sky simulations were compared to line-by-line model results presented by Luther (1984). The most serious discrepancies occurred with the absorption of CO_2. Upon examination it was concluded that the emission by CO_2 in the stratosphere exceeded that of the line-by-line results while the opposite occurs in the troposphere. This problem was traced back to the scaling parameters used in calculating the optical paths and it was concluded that the optical paths in the stratosphere were too long while being too short in the troposphere. Although this problem leads to significant errors in upper stratospheric heating rates ($\approx 2°K/day$ at 50 km), the tropospheric heating rates especially at altitudes typical of cirrus are observed are less than 0.3 $°K/day$ when considering all three major infrared absorbers H_2O, CO_2 and O_3 combined. Absolute flux errors were observed to be within the $\pm 15\ W \cdot m^{-2}$ of other approximate schemes compared in the study of Luther (1985).

Solar wavelength comparisons were made between the line-by-line calculations of Chou and Arking (1981) and the present model were made for H_20 absorption. Differences between heating rates presented in the tropical atmosphere were less than 0.1 $°K day$ and decreased with altitude.

The Processes of e-type absorption in the infrared and Rayleigh scattering were also shown to compare well with other studies. Based on these comparisons it was concluded that the narrow band two stream radiative transfer model is capable of determining the infrared and the solar wavelengths radiative transfer properties of clear sky well enough to be used in the simulation of cirrus cloudiness. For applications involving climate, especially those involving scenarios of a change in CO_2, the problems in the infrared must be revisited and solved.

6.2.2 Cloudy-Sky Simulation

A shortwave simulation of a cloud case was performed in order to demonstrate the applicability of the present model to a cloudy atmosphere. The results of the present model were compared to those of a more complicated n-stream model (n=4 for this comparison). In addition, the sensitivity of the present two-stream model to various backscatter

approximations developed in literature and summarized by King and Harshvardan (1986) was examined. The two-stream flux results were shown to be consistent with the fluxes produced by the four stream leading to the conclusion that the present two stream is viable for cloudy-sky radiative transfer.

6.3 Theoretical Cirrus Investigations

In order to examine the performance of the model and to investigate some of the phenomenological properties of cirrus clouds, simulations were performed for various atmospheres and size distributions. Investigations of cirrus imbedded in various atmospheres were conducted mainly to further validate the model and its applicability to cirrus clouds. Simulations assuming size distributions chosen from the FIRE observations and adjusted to include varying concentrations of small ice particles, were performed to evaluate the effect of these small particles on the radiative characteristics of cirrus clouds.

6.3.1 Effects of the Atmosphere Environment

Based on these model simulations in the infrared it is concluded that:

1. cloud top infrared cooling and cloud base heating are enhanced by increasing IWC,
2. the thinnest clouds at low altitudes (ie. $T_{surface} - T_{cloudbase}$ small) cooled throughout the cloud layer but heated at high altitudes (ie. $T_{surface} - T_{cloudbase}$ large),
3. the net radiative effect of cirrus is largely determined by surface-cloud base temperature difference (and thus altitude) and that heating (cooling) increases with increasing (decreasing) altitude,
4. spectral analysis revealed that radiative heating dominates in the window region (8-12 μm) while cooling is dominated more in the far infrared ($\approx$ 15-200 μm), and
5. the heating (cooling) of the window region (far infrared) increases in both magnitude and spectral width with increasing (decreasing) altitude.

The shortwave simulations revealed the following:

1. radiative heating rate profiles showed maximum heating at cloud top which decreased monotonically toward cloud base,

2. the radiative heating at cloud top decreased with decreasing cloud top altitude, and

3. the changes in the spectral distribution of absorption as a function of altitude were mainly confined to the 2.6 - 2.9 μm region where CO_2 is an active absorber.

The behavior of the radiative characteristics of cirrus in various atmospheres as deduced by the two-stream model agrees qualitatively to studies presented by Ackerman *et al.* (1988). Additionally, these results have profound climatological implications. It is not enough to know the amount or distribution of cirrus about the globe to understand their influence on the earth radiation budget. In order to understand the climatological effects of cirrus clouds, information regarding temperature and height as well as their distribution and microphysical characteristics must also be understood.

6.3.2 The Effects of Small Particles

Particles less than 25.0 μm in size were not measured during the cirrus IFO but their presence was speculated. Concentrations of particles less than 100 μm in size were noted to be a source of uncertainty in understanding the radiative characteristics of cirrus clouds. To assess the importance of this uncertainty small particles were added to the observed crystal size distributions. The following sensitivities of the model were noted.

1. The addition of relatively small concentrations of small particles results in a substantial enhancement of cloud radiative heating and cooling rates, cloud emittances and albedos.

2. Although the addition of small particles enhanced the IWC of the clouds, the effect of this increase on the cloud radiative characteristics was small relative to the enhanced extinction by small particles.

3. For spectral wavelengths less than 0.28 μm, changes in the radiative characteristics of the cirrus caused by the enhancement of IWC, approach those due to the presence of small particles.

It was concluded from the simulations that appreciable differences between observations of cirrus radiative characteristics and theoretical calculations for wavelengths greater than 0.28 μm may be partly attributable to uncertainties of the amount of small particles in the observed size distributions.

6.3.3 Variable IWC clouds with Small Particles

An investigation of vertically variable IWC clouds (IWC decreased with increasing altitude) was performed and radiative characteristics of these clouds were contrasted to those of uniform clouds. The sharp discontinuities of the radiative heating and cooling rates at cloud top and cloud base exhibited by uniform clouds were not observed. Instead, for profiles of IWC typical of those observed in cirrus clouds during the FIRE IFO,

1. solar heating rates increased from cloud top to the thickest cloud layer near the base of the cloud, and

2. infrared heating rates increased from cloud base to the thickest cloud layer.

Simulations of variable IWC profile clouds with small particles were also performed. Radiative solar (infrared) heating (cooling) rates were increased (decreased) with increased of concentrations of small particles. Upon examination of the net radiative effect of the cloud it was observed that for this case the increase in the concentration of small particles changed the cloud from net radiative cooling to net warming.

The following conclusions were drawn from these simulations:

1. The vertical structure of IWC affects the magnitude and shape of radiative heating rate profiles throughout the clouds.

2. The net radiative effect of the cirrus cloud is highly sensitive to changes in the size distributions representative of these clouds.

These results contain important implications to the evolution and dissipation processes within cirrus and its interactions with the environment.

6.4 Comparison to Observations

Comparisons between the thin cirrus case observed during the FIRE cirrus IFO on October 28, 1986 over the vicinity of Green Bay, Wisc. and model simulations of this case were presented.

The conclusions drawn from the comparison between the observations and simulations are listed as follows:

1. Underestimations of radiative heating rates in the infrared wavelengths and in the variation of emittance with IWP are perhaps largely due to the overestimation of the effective crystal size of the size distributions. This is caused by both the equivalent diameter sphere approximations and the underestimation of particles smaller than 100 μm.

2. Model underestimation of solar albedos is perhaps due in part to the overestimation of the asymmetry parameter as a result of the assumption of spherical particles.

It is clear from these results that the uncertainties involved in the estimation of the scattering properties of ice clouds remain one of the major hurdles that separates the agreement between the observations and simulations. Until the scattering properties of cirrus clouds are better understood, the interactions of radiation with microphysical parameters in the life cycle of these clouds will remain somewhat of a mystery. In addition, the climatic feedbacks of this radiation microphysical interaction will remain uncertain.

6.5 Limitiations and Recommendations

The aim of this study was to examine possible differences between the model and observations and to make inferences concerning the reduction of these differences. The uncertainties in the observations and the microphysical approximations used in the simulations were discussed. Improvements in the environmental, microphysical and radiation measurements and the theory which predicts the scattering properties of cirrus clouds would greatly improve the theoretical and observations agreement. The specific uncertainties in the environmental, microphysical and radiative measurements that contributed to disagreement between observations and simulations are:

1. Observations

(a) A reliable vertical moisture profile throughout the cloud could not be inferred from the radiosonde or aircraft measurements. This is most important when calculating radiative heating rates throughout the cloud. Solar (infrared) heating rates were enhanced (reduced) with increased water vapor amount. A better understanding of the moisture within these clouds is crucial to dynamical and microphysical cirrus modeling (Ramaswamy and Detwiler, 1976).

(b) The concentration of particles less than 100 μm in physical size was not measured. The presence of these particles despite their concentration greatly affect the scattering properties of the cirrus clouds. Simulations show the enhancement of radiative heating rates, emittances and albedos with the addition of small particles to the observed size distributions.

(c) The radiative measurements themselves contained uncertainties mainly caused be cloud inhomogeneity. The inhomogeneities within the cloud were unexpectedly large with standard deviations of fluxes at cloud top and bottom as large as 20 $W \cdot m^{-2}$ in the infrared and 60 $W \cdot m^{-2}$ in the solar wavelengths. This variability corresponded to uncertainties in the radiative heating rates in the infrared and solar wavelengths of approximately $\pm 2° K \cdot day^{-1}$ and $\pm 5° K \cdot day^{-1}$ respectively. An additional problem, which had been left unstated, was the low zenith angles associated with the observations which caused biases in the data to some of the upward looking shortwave instruments in a matter that depended on the heading of the aircraft. This may account for the problems encountered in reducing the shortwave data.

(d) The impossibility of flying simultaneous vertical profiles throughout the clouds caused general sampling problems. Due to the tenuous and changing nature of these clouds, horizontal race tracks at different altitude levels were not necessarily measuring the same cloud, especially because the race tracks did not follow the mean wind downstream.

The uncertainties listed in points (a) and (b) represent the areas in which improvements would be the most fruitful. The uncertainties of points (c) and (d) are for the most part unavoidable. Additionally, the analysis technique developed to reduce the uncertainty associated with points (c) and (d) do provide reliable estimates of the actual radiative properties of cirrus clouds.

The specific uncertainties associated with the simulations mostly relate to the model input scattering parameters and may prove to be more significant than the uncertainties associated with the observations. The uncertainties of the simulations are:

2. Model Simulations

   (a) The scattering and absorbing properties of irregularly shaped ice crystals are assumed to be similar to the scattering and absorbing properties of equivalent diameter spherical crystals. It is known that the actual ice crystals are for the most part nonspherical, therefore this assumption will tend to overestimate the areas and volumes of the actual particles within the cloud. In addition, the assumption of spherical particles leads to the overestimation of the asymmetry parameter or forward scattering of cirrus and therefore leads to an underestimation of cloud albedos.

   (b) Horizontal homogeneity is assumed in order to derive the two stream model. These assumptions were obviously violated by the actual cloud observed during the October 28 Fire case.

   (c) The Henyey-Greenstein function which was scaled to provide a more forward scale after Joseph *et al.* (1976) was used to approximate the phase function. Uncertainties caused by this approximation are not known.

   (d) The reliability of the two stream model in the solar wavelengths decreases with increasing solar zenith angle (King and Harshvardan, 1986). To the extent this adds uncertainty to these simulations is not known.

The uncertainties (a) and (b) above are partially the cause of the disagreement between the observations and simulations. A better representation of the scattering properties of the cirrus cloud would improve the initialization of the model.

6.6 Recommendations for Future Research

Since so much of the disagreement observed in this research occurs due to the misrepresentations of the scattering properties of cirrus clouds, future research should be aimed in the following areas.

1. Development of new theoretical methods of estimating the scattering properties of irregular ice crystals. The anomalous diffraction theory and the discrete dipole method are two such methods which may be potential candidates.

2. Development of instruments capable of measuring small irregular ice particles.

3. In view of the apparent large variability of the clouds, development of radiative transfer methods capable of handling cloud inhomogeneities is required. The model proposed by Stephens (1988) might be a candidate method.

4. Investigation of the k-distribution scaling parameters particularly as they relate to CO_2 to improve gaseous absorption and clear sky radiative heating rates in the stratosphere.

Finally, once the scattering properties of cirrus clouds are better understood, the relationship between albedo and emittance formulated by the model developed in this thesis provides a suitable framework for the parameterization of these processes for use in dynamical models of cirrus.

REFERENCES

Ackerman, S. A., S. K. Cox, 1981: Aircraft observations of the shortwave fractional absorptance of non-homogeneous clouds. *J. Appl. Meteor.*, **20**, 128–133.

Ackerman, T. P., K.-N. Liou, F. P. J. Valero and L. Pfister, 1988: Heating rates in tropical anvils. *J. Atmos. Sci.*, **45**, 1606–1623.

Albrecht, B., and S. K. Cox, 1976: Radiation data reduction procedures for Sabreliner, C-10 and DC-6 aircraft during GARP Atlantic Tropical Experiment. *Atmos. Sci. Pap. No. 244,* Colorado State University, Ft. Collins, 100 pp.

Albrecht, B., and S. K. Cox, 1977: Procedures for improving pyrogeometer performance. *J. Appl. Meteor.*, **16**, 188–197.

Arking, A., and K. Grossman, 1972: The influence and band structure on temperatures in planetary atmospheres. *J. Atmos. Sci.*, 937-949.

Blanchet, J. P., 1985: On radiative heating due to polar stratospheric clouds. *Tellus,* **37B**, 197–209.

Chou, M. -D., 1984: Broadband water vapor transmission functions for atmospheric IR flux computations. *J. Atmos. Sci.*, **41**, 1775–1778.

——, and A. Arking, 1980: Computation of infrared cooling rates in the water vapor bands. *J. Atmos. Sci.*, **37**, 855–867.

——, and A. Arking, 1981: An efficient method for computing the absorption of solar radiation by water vapor. *J. Atmos. Sci.*, **38**, 798–807.

——, and L. Peng, 1983: A parameterization of the absorption in the 15 μm spectral region with application to climate sensitivity studies. *J. Atmos. Sci.*, **40**, 2183–2192.

Cox, S. K., 1973: Cirrus Clouds and the Climate. it J. Atmos. Sci. **28**, 1513–1515.

Cox, S. K., 1976: Observations of cloud infrared effective emissivity. it J. Atmos. Sci. **33**, 287–289.

Davis, J. M., S. K. Cox, 1982: Reflected solar radiances from regional scale scenes, it J. Appl. Meteor., **21**, 1698–1712.

Foot, J. S., 1988: Some observations of the optical properties of clouds. II: Cirrus. *Quart. J. Roy. Meteor. Soc.*, **114**, 145–164.

Grant, I. P. and G. E. Hunt, 1969: Discrete space theory of radiative transfer II. Stability and non-negativity. *Proc. Roy. Soc. Lond.*, **313**, 199–216.

Griffith, K., S. K. Cox, and R. G. Knollenburg, 1980: Infrared radiative properties of tropical cirrus clouds inferred from aircraft measurements. *J. Atmos. Sci.,* **37**, 1077-1087.

Hansen, J. E., G. Russel, D. Rind, P. Stone, A. Lacis, S. Lebedeff, R. Ruedy and L. Travis, 1983: Efficient three-dimensional global models for climate studies: Models I and II. *Mon. Wea. Rev.,* **111**, 609–662.

Hein, P. F., S. K. Cox, C. M. Johnson-Pasqua, 1987: The Sabreliner data set of the FIRE Cirrus IFO: FIRE Series No. 1. *Atmos. Sci. Pap. No. 418,* Colorado State University, Ft Collins, 52 pp.

Heymsfield, A. J., 1977: Precipitation development in stratiform ice clouds: a microphysical and dynamical study. *J. Atmos. Sci.,* **34**, 367–381.

——, and D. Baumgardner, 1985: Summary of a workshop on processing 2-D probe data. *Bull. Amer. Meteor. Soc.,* **66**, 437–440.

——, and K. M. Miller, 1989: The October 27-28, 1986, FIRE cirrus case study: cloud microstructure. *submitted to Mon. Wea. Rev.*

Iqbal, M., 1983: *An Introduction to Solar Radiation,* Academic Press, 390 pp.

Joseph, J. H., W. J. Wiscombe and J. A. Weinman, 1986: The delta-eddingtopn approximation for radiative flux transfer. *J. Atmos. Sci.,* **33**, 2452–2459.

King, M. D., and Harshvardhan, 1986: Comparative accuracy of selected multiple scattering approximations. *J. Atmos. Sci.,* **43**, 784–801.

Kneizys, F. X., E. P. Shettle, W. O. Gallery, J. H. Chetwynd, Jr., L. W. Abreu, J. E. A. Selby, R. W. Fenn, and R. A. McClatchey, 1980: Atmospheric Transmittance/Radiance: computer code LOWTRAN 5. Report No. AFGL-TR-80-0067, Air Force Geophysics Lab, Hanscom AFB, MA., 200 pp.

Liou, K.-N., 1986: Influence of cirrus clouds on weather and climate processes: a global perspective. *Mon. Wea. Rev.,* **114**, 1167–1199.

Luther, F. M., 1985: The intercomparison of radiation codes in climate models (ICR-CCM) – longwave clear-sky calculations. (Frascati, Italy, 15-18 August 1984), World Climate Programme Series report **93**, 44 pp.

Manabe, S. and R. F. Strickler, 1974: Thermal equilibrium of the atmosphere with a convective adjustment. *J. Atmos. Sci.* **21**, 361–385.

McClatchey, R. A., R. W. Fenn, J. E. A. Selby, F. E. Voltz, and J. S. Garing, 1972: Optical properties of the atmosphere, 3rd ed. AFCRL-72-0497, 108 pp.

McKee, T. B. and S. K. Cox, 1974: Scattering of visible radiation by finite clouds. *J. Atmos. Sci.* **31**, 1885–1892.

Meador, W. E., and W. R. Weaver, 1980: Two stream approximations to radiative transfer in planetery atmospheres: A unified description of existing methods and a new improvement. *J. Atmos. Sci.,* **37**, 630–643.

Paltridge, G. W., and C. M. R. Platt, 1976: *Radiative Processes in Meteorology and Climatology,* Elsevier, 318 pp.

——, and ——, 1981: Aircraft observations of solar and infrared radiation and microphysics of cirrus cloud *Quart. J. Roy. Meteor. Soc.*, **107**, 367–380.

Platt, C. M. R. and Harshvardhan, 1988: Temperature dependence of cirrus extinction: implications for climate feedback. *J. Geophys. Res.*, **93**, 11051–11058.

Pollack, J. B. and J. D. McKay, 1985: The impact of polar stratospheric clouds on the heating rates of the winter polar stratosphere. *J. Atmos. Sci.*, **42**, 245–262.

Prabhakara, C., R. S. Fraser, G. Dalu, M.-L. C. Wu and R. J. Curran, 1988: Thin cirrus clouds: seasonal distribution over oceans deduced from Nimbus-4 IRIS. *J. Appl. Meteor.*, **27**, 379–399.

Preisendorfer, R. W., 1976: *Hydrological Optics V. Properties,* NOAA, PMEL.

Ramanathan, V., 1987: The role of the earth radiation budget studies in climate and general circulation research. *J. Geophy. Res.*, **92**, 4075–4095.

Ramanathan, V., 1989: Atmospheric general circulation and its low frequency variance. *submitted to J. Meteor. Soc. Japan.*

Ramaswamy, V. and A. Detwiler, 1986: Interdependence of radiation and microphysics in cirrus clouds. *J. Atmos. Sci.*, **43**, 2289–2301.

Ramaswamy, V. and V. Ramanathan, 1989: Solar absorption by cirrus clouds and the maintenance of upper troposphere thermal structure. *submitted to J. Atmos. Sci.*

Roberts, R. E., J. E. A. Selby and L. M. Biberman, 1976: Infrared continuum absorption by atmospheric water vapour in the 8–12 μm window. *Appl. Opt.*, **15**, 2085–2090.

Rockwood, A. A. and S. K. Cox, 1976: Satellite inferred albedo over northwestern Africa. *Atmos. Sci. Pap. No. 262,* Colorado State University, Ft. Collins, 64 pp.

Roeckner, E., U. Schlese, J. Biercamp and P. Loewe, 1987: Cloud optical depth feedbacks and climate modeling. *Nature,* **329**, 138–140.

Sagan, C., and J. B. Pollack, 1967: Anisotropic nonconservative scattering and the clouds of Venus. *J. Geophys. Res.*, **72**, 469–477.

Slingo, and H. M. Schrecker, 1982: On the shortwave properties of stratiform water clouds. *Quart. J. Roy. Meteor. Soc.*, **108**, 407–426.

Smith, Jr., W. L., S. K. Cox and V. Glover, 1988: Temperature sensitivity of Eppley broadband radiometers. *Atmos. Sci. Pap. No. 423,* Colorado State University, Ft. Collins, 12 pp.

——, P. F. Hein and S. K. Cox, 1989: The October 27-28, 1986, FIRE cirrus case study: *in situ* observations of radiation and dynamic properties of a cirrus cloud layer. *submitted to Mon. Wea. Rev.*

Stamnes, K., S-C. Tsay, W. Wiscombe and K. Jayaweera, 1988: Numerically stable algorithm for discrete-ordinate-method radiative transfer in multiple scattering and emitting layer media. *Appl. Opt.*, **27**, 2502–2509

Starr, D. O'C. and D. Wylie, 1989: The October 27-28, 1986, FIRE cirrus case study. *submitted to Mon. Wea. Rev.*

Stephens, G. L., 1980: Radiative properties of cirrus clouds in the infrared region. *J. Atmos. Sci.*, **37**, 435–446.

——, 1984: The parameterization of radiation for numerical weather prediction and climate models. *Mon. Wea. Rev.*, **112**, 826–867.

——, 1988: Radiative transfer through arbitrarily shaped optical media. Part I: a general method of solution. *J. Atmos. Sci.*, **45**, 1818– 1836.

——, and P. J. Webster, 1979: Sensitivity of radiative forcing to variable cloud and moisture. *J. Atmos. Sci.*, **36**, 1542–1556.

——, and ——, 1981: Clouds and climate: Sensitivity of simple systems. *J. Atmos. Sci.*, **38**, 235–247.

——, P. W. Stackhouse, Jr., and P. J. Flatau, 1989: The relevance of the microphysical and radiative properties of cirrus clouds to climate and climatic feedback. *submitted to J. Atmos. Sci.*

Toon, O. B., C. P. McKay and T. P. Ackerman, 1989: Rapid calculation of radiative heating rates and photodissociation rates in inhomogeneous multiple scattering atmospheres. *submitted to J. Geophys. Res.*

Tsay, S-C., 1986: *Numerical study of the atmosphere radiative transfer process with applications to the arctic energy balance.* Ph.D. dissertation, University of Alaska, Fairbanks, 251 pp.

Wiscombe, W. J. and G. W. Grams, 1976: The backscattered fraction in two- stream approximations. *J. Atmos. Sci.*, **33**, 2440–2451.

Zdunkowski, W. G., R. M. Welch and G. Korb, 1980: An investigation of the structure of typical two-stream-methods for the calculation of solar fluxes and heating rates in clouds. *Contrib. Atmos. Phys.*, **53**, 147–166.